

# Secondary Flow Mitigation in Turbine Vanes Through Endwall Fence Shape Optimization

Giacomo Mingardo

Technische Universiteit Delft



# SECONDARY FLOW MITIGATION IN TURBINE VANES THROUGH ENDWALL FENCE SHAPE OPTIMIZATION

by

**Giacomo Mingardo**

to obtain the degree of

**Master of Science in Aerospace Engineering**

at the

**Delft University of Technology,**

to be defended publicly on  
**Monday January 15th, 2018 at 14:00.**

Student number:	4519035	
Project duration:	June, 2016 - December, 2017	
Supervisors:	Prof. dr. ir. M. Pini,	TU Delft
	Prof. dr. ir. C. Lettieri	TU Delft
Thesis committee:	Prof. dr. ir. M. Pini,	TU Delft
	Prof. dr. ir. P. Colonna,	TU Delft
	Dr. ir. R. Pecnik	TU Delft

An electronic version of this thesis is available at <http://repository.tudelft.nl/>.



# PREFACE

The completion of this work entails the very end of my studies and the end of my time at the TU Delft. These years of master were extraordinarily fruitful for both my personal and professional growth. On the personal side, I had the chance of getting in touch with many different cultures and way of thinking. On the professional side, the master in *Flight Performance and Propulsion* provided me with the competences and the knowledge that I was looking for, allowing me to start my career in the industry of aerospace propulsion, as in my objective. For these reasons, I am extremely satisfied with my choice of coming to the TU Delft. In particular, this thesis project was the most engaging part of the experience, because I found pleasantly gratifying to carry out a research in autonomy. Also, this project gave me the unique opportunity to travel the world, working at the Osaka Institute of Technology for three months, and presenting the research at the ASME TurboExpo in Charlotte.

For this amazing opportunity, I am deeply grateful to my supervisors Matteo and Claudio, who chose me for this project and helped me whenever I was stuck.

I own an *arigato gozaimasu* to professor Kawata for his supervision, to my colleagues Kakeru and Shouhei, for the collaboration and the friendship, and in general to all the team from the OIT, for their hospitality.

Francesco, it was great working and living all these experiences with you, I still wonder how you stood me for so much time.

I want to thank all the friends who made special my years in Delft, especially Marco, Marco and Cristiano for your support, and Giorgio and Giulia for bearing me during the stressful period of the thesis writing.

I thank my parents and my sister, for motivating me during all my life and particularly in the most difficult moments of my studies. I own this and all of my achievements to you.

A special mention goes to my dear Sara, who was on my side throughout all the challenges I faced, giving me her support anytime.

Last but not least, I thank all my friends from Padua, in particular Giuseppe, Alberto, Alberto Maria, Andrea, Virgilio, Marco, Stefano, Benedetta and Chiara, who always make me feel at home when I go back to my beloved hometown Padova.

*Giacomo Mingardo  
Delft, January 2018*



# ABSTRACT

The threat of global warming made the increase of efficiency a crucial objective for future power plants and aero engines. As secondary flow is a major source of aerodynamic losses in turbines [1], its mitigation is critical to enable efficient designs. However, the suppression of secondary flow formation is challenging due to the complexity of the flow field and to the variability of its features according to each cascade characteristics. One solution is the use of three-dimensional endwall fence, to reduce secondary flow losses. Three-dimensional fences can reduce the secondary flow penetration, increase the pitch-wise uniformity of vorticity, reduce the kinetic energy of the crossflow and decrease the mixing out of the vortices downstream the blade passage. At the same time, the endwall fence entails an increment of wetted area and viscous losses, making the design of its shape a trade-off problem. The design of such devices must be tailored to the specific turbine and is usually obtained via lengthy and time-consuming experimental campaigns. Shape optimization can greatly enhance the design process of these components as it provides a way to investigate the fluid dynamic performance of a multitude of fence geometries at affordable computational cost. This paper presents a numerical methodology to automate the endwall fence design; a surrogate-based optimization is applied to minimize the total pressure losses of a steam turbine cascade [2]. The results of the numerical analysis indicate a reduction of 48% of the secondary kinetic energy leading to a decrease of 1.96% in total pressure loss of the optimized design with respect to the baseline geometry without endwall fence. The partition of the passage vorticity led to a weakening of the secondary flow strength and consequently to reduced downstream mixing losses. A wind tunnel validation of the improvement has been finally carried out, confirming the success of the methodology.



# CONTENTS

<b>Abstract</b>	<b>v</b>
<b>List of Figures</b>	<b>ix</b>
<b>List of Tables</b>	<b>xiii</b>
<b>List of Symbols and Abbreviations</b>	<b>xv</b>
<b>1 Introduction</b>	<b>1</b>
1.1 Background	1
1.2 Research Questions and Objectives	2
1.3 Original Contribution of this Work	3
1.4 Outline of the Thesis	4
<b>2 Theoretical Background</b>	<b>5</b>
2.1 Basic Concepts of Flow Vorticity and Secondary Flows Generation	5
2.2 Secondary Flows in Turbomachinery	7
2.2.1 The Secondary Flow Picture	7
2.2.2 Limiting Streamlines Topology	10
2.2.3 Secondary Loss Generation and Evolution	12
2.2.4 Additional Side Effects of Secondary Flows	14
2.2.5 Parameters Influencing the Evolution of Secondary Flow	15
2.3 Secondary Flow Mitigation Techniques	19
2.3.1 Splitter Vanes	20
2.3.2 Blade Leaning	20
2.3.3 Endwall Contouring	22
2.3.4 Blade Fence	24
2.3.5 The Endwall Fence	25
2.4 CFD Modeling of Secondary Flow	27
2.5 Surrogate Model Optimization for CFD-Based Automated Design	28
2.5.1 Design of Experiments	29
2.5.2 Response Surface Types	30
2.5.3 Optimization	31
<b>3 Technical Approach</b>	<b>33</b>
3.1 Automated Design Chain	33
3.2 Fence Parameterization	34
3.3 Meshing Process	36
3.3.1 Mesh Adaption Through Geometrical Elements Association	36
3.4 CFD Model	37
3.5 Optimization through Response Surface	37
<b>4 Case Study</b>	<b>39</b>
4.1 Test Case Presentation	39
4.1.1 Mesh Independence Analysis	42
4.2 Resulting Response Surface	42
4.3 Optimal Fence Shape	44
4.4 Physical Mechanism of Loss Reduction	45
4.4.1 Analysis of $C_{loss}$	47
4.4.2 Analysis of $C_{SKE}$	49
4.4.3 Discussion on the Improvement Mechanism	53

<b>5</b>	<b>Experimental Validation</b>	<b>57</b>
5.1	Wind Tunnel Experiments . . . . .	58
5.1.1	Experimental Setup . . . . .	58
5.1.2	Data Acquisition Procedure . . . . .	59
5.2	Experimental Error Assessment . . . . .	61
5.3	Validation Results . . . . .	62
5.3.1	Independent Validations of Both Configurations . . . . .	62
5.3.2	Validation of the Optimization . . . . .	64
<b>6</b>	<b>Conclusions and Recommendations</b>	<b>69</b>
6.1	Conclusions . . . . .	69
6.2	Recommendations for Future Works . . . . .	69
	<b>Bibliography</b>	<b>71</b>

# LIST OF FIGURES

1.1	Representation of the secondary flow development and interaction, Coull [3], 2016. . . . .	2
1.2	Schematic representation of fence blocking the horse-shoe vortex migration, Chung and Simon [58], 1993. . . . .	3
2.1	Example of boundary layer velocity profile and rotation of the fluid element due to the vorticity (Greitzer [7], 2004). . . . .	6
2.2	Distortion of the vortical filament due to the non-uniform velocity distribution in the bend and generation of streamwise vorticity (Greitzer [7], 2004). . . . .	7
2.3	Generation of secondary flow in a turbine cascade due to the flow deflection (Dixon et al. [10], 2014). . . . .	8
2.4	Classical representation of secondary flow in turbine cascade. (Hawthorn [11], 1955). . . . .	8
2.5	Representations of the horseshoe vortex formation: (a) schematic of boundary layer vortical lines wrapping around an object (Greitzer [7], 2004), (b) velocity vectors showing boundary layer separation upstream an object that leads to the horseshoe vortex (Eckerle and Langston [15], 1986). . . . .	9
2.6	Comparison between secondary flow representations according to Klein [14] (a) and Langston [18] (b). . . . .	9
2.7	Streamwise evolution of the secondary flow according to smoke visualization experiments carried out by Sieverding and Van den Bosch, [20], 1983. . . . .	10
2.8	Sketch of secondary flow as observed by Sharma and Butler[6], 1987. . . . .	10
2.9	Secondary flow representation of Wang, Olson, Goldstein and Eckert [24], 1997. . . . .	11
2.10	Separation lines in a turbine cascade from the endwall flow visualization experiment of Langston et al. [22], 1977. . . . .	11
2.11	Drawing of separation lines in a cascade, Sieverding [21], 1985. . . . .	12
2.12	Examples of spanwise distributions of losses downstream a cascade for increasing blade loadings, Sieverding [21], 1985. . . . .	13
2.13	$b/\delta_{inlet}$ trends as a function of $\delta_{inlet}/g$ ( $g$ is the blade pitch) for different blade loadings, Sieverding [21], 1985. . . . .	14
2.14	Distributions of static pressure coefficient around a blade at different span locations, Langston et al. [18], 1977. . . . .	14
2.15	Comparison of outlet flow angle between design distribution and actual distribution, affected by the under and over-turning due to the secondary flow. Dixon [10], adapted from Horlock, 1963. . . . .	15
2.16	Comparison of measurements obtained with incidence angles $-30^\circ$ , $0^\circ$ and $+30^\circ$ ; distributions of: (a) kinetic energy losses, (b) secondary velocity. Perdichizzi et al. [32], 1996. . . . .	17
2.17	Comparison of loss distributions and secondary velocity fields for outlet flow Mach numbers 0.5, 0.72, 1.15, 1.38, 1.55, at a distance of 1.9 blade axial chords ( $C_{ax}$ ) away from the blade trailing edge. Passage vortex in red, shed vortex in green, corner vortex in yellow. Perdichizzi et al. [34], 1989. . . . .	17
2.18	Spanwise distributions scaled with midspan conditions of: (a) kinetic energy losses, (b) outflow angle. Measurements taken at a distance of 2.1 blade axial chords ( $C_{ax}$ ) away from the blade trailing edge. Perdichizzi et al. [34], 1989. . . . .	18
2.19	Trend of net secondary losses against the outlet Mach number. Perdichizzi et al. [34], 1989. . . . .	18
2.20	Results from inviscid calculations of exit $C_{SKE}$ against the inverse of cascade aspect ratio. Clark et al. [4], 2016. . . . .	19
2.21	Comparison of secondary flow streamlines development on a normal low aspect ratio turbine cascade with the same cascade with the addition of splitter blades (and increased blade pitch). Clark et al. [4], 2016. . . . .	20
2.22	Schematic representing the effect of blade leaning on the secondary flow, as superimposition of common passage vorticity and vorticity introduced by leaning. D'Ippolito et al. [39], 2011. . . . .	21
2.23	Sketch of front view of prismatic, lean and bow (i.e. compound) blades. Harrison [40], 1992. . . . .	21

2.24	Comparison of planar loss distributions between planes located at 83% and at 123% of the $C_{ax}$ from the leading edge. . . . .	22
2.25	Drawing of an S-shaped endwall contouring. Dossena, Perdichizzi and Savini [44], 1998. . . . .	22
2.26	Schematic illustrating an example of leading edge fillet, Zess and Thole [45]. . . . .	23
2.27	(a) Cross-sectional view of leading edge bulbs, (b) bulb surface mesh. Sauer et al. [46], 1999. . . . .	23
2.28	Color plot of the perturbation field used to obtain the contoured endwall profile in [48], Luo, Liu and McBean, 2011. . . . .	24
2.29	Schematics representing a cascade with blade boundary layer fences. Kawai and Adachi, [53], 1987. . . . .	24
2.30	Cascade with endwall fences. Kawai et al., [54], 1989. . . . .	25
2.31	Endwall fence designed by Chung and Simon, [58], 1993. . . . .	26
2.32	Vorticity iso-surface showing the formation of a counter vortex above an endwall fence of height equal to one-third of the boundary layer thickness, Moon and Koh [60], 2000. . . . .	26
2.33	Topology of skin-friction lines in a cascade with endwall fence: (a) on the endwall and (b) on the blade suction side. Kumar and Govardhan [63], 2014. . . . .	27
2.34	Comparison between total pressure loss coefficient from CFD results and experimental results. Moon and Koh, [60], 2001. . . . .	28
2.35	CCD disposition of points [67]. . . . .	29
2.36	Disposition of points in a Box-Behnken Design [67]. . . . .	30
2.37	Comparison of the disposition of points with an LHS and with an OSF [67]. . . . .	30
2.38	Scheme of Neural Network algorithm [67]. . . . .	31
3.1	Block diagram representing the automated design loop. . . . .	34
3.2	Sketches showing the parameterizations of: (a) position (b) camber line and length (c) thickness distribution (d) height distribution. . . . .	35
3.3	CAD models of: (a) the flow passage domain and (b) an example of endwall fence. . . . .	35
3.4	Mesh blocks adapted to the shape of the flow domain. . . . .	36
3.5	Example of automatic mesh adaptation to the fence geometry modification. . . . .	37
3.6	Example of response surface for total pressure loss coefficient as a function of the position of the camber line control point. . . . .	38
4.1	Representations of the turbine cascade geometry: (a) 2D sketch, (b) CAD view of the blade passage with the baseline shape of the endwall fence. . . . .	40
4.2	Schematic of the baseline fence shape with values of geometrical parameters. . . . .	41
4.3	Mesh convergence analysis results. . . . .	42
4.4	$C_{loss}$ response surface for the fence leading edge position in pitchwise $x_1$ and streamwise $x_2$ direction against the . . . . .	43
4.5	Identification in the cascade endwall of the optimal region for the fence position in the response surface. . . . .	43
4.6	Schematic of the optimal fence with all the relevant dimensions. . . . .	44
4.7	Optimal fence position and shape compared to the blade camber line passing for the middle of the passage. . . . .	45
4.8	Comparison between optimal and baseline fence. . . . .	45
4.9	Planes used to study the evolution of $C_{loss}$ and $C_{SKE}$ spanwise distributions. . . . .	47
4.10	Comparison between evolution of $C_{loss}$ spanwise distributions for baseline case and optimal case. . . . .	48
4.11	Comparison between $C_{loss}$ spanwise distributions for baseline case and optimal fence case at the TE plane, Plane 4 and Plane 7. . . . .	49
4.12	Distributions on the TE Plane of: (a) $C_{loss}$ for the baseline geometry, (b) $C_{loss}$ for the optimal geometry, (c) $\Delta C_{loss}$ between baseline and optimal case. . . . .	50
4.13	Distributions on Plane 4 of: (a) $C_{loss}$ for the baseline geometry, (b) $C_{loss}$ for the optimal geometry, (c) $\Delta C_{loss}$ between baseline and optimal case. . . . .	50
4.14	Distributions on Plane 7 of: (a) $C_{loss}$ for the baseline geometry, (b) $C_{loss}$ for the optimal geometry, (c) $\Delta C_{loss}$ between baseline and optimal case. . . . .	51
4.15	Streamwise evolution of the $C_{loss}$ for baseline and optimal case. . . . .	51
4.16	Comparison between evolution of $C_{SKE}$ spanwise distributions for baseline case and optimal fence case. . . . .	52

4.17 Comparison between $C_{SKE}$ spanwise distributions for baseline case and optimal fence case on the TE plane, plane 4 and plane 7. . . . .	52
4.18 Distributions on the TE Plane of: (a) $C_{ske}$ for the baseline geometry, (b) $C_{ske}$ for the optimal geometry, (c) $\Delta C_{ske}$ between baseline and optimal case. . . . .	53
4.19 Distributions on Plane 4 of: (a) $C_{ske}$ for the baseline geometry, (b) $C_{ske}$ for the optimal geometry, (c) $\Delta C_{ske}$ between baseline and optimal case. . . . .	53
4.20 Distributions on Plane 7 of: (a) $C_{ske}$ for the baseline geometry, (b) $C_{ske}$ for the optimal geometry, (c) $\Delta C_{ske}$ between baseline and optimal case. . . . .	54
4.21 Streamwise Evolution of the Secondary Kinetic Energy Coefficient for Baseline and Optimal Case. . . . .	54
4.22 Comparison between vortex development in baseline and optimal cases. . . . .	55
4.23 Comparison of wall shear distribution on the blade suction side for baseline and optimal configurations. . . . .	55
5.1 Position of the measurement plane in the CFD domain. . . . .	57
5.2 Drawing of the wind tunnel with zooms on the inlet Pitot tube and the rotatable cascade. . . . .	58
5.3 5-holes Pitot tube positioned downstream of the cascade (a) and the automatic positioning system (b). . . . .	59
5.4 5-holes Pitot tube orientation angles and holes positioning. . . . .	59
5.5 Schematic of the automatic positioning system. . . . .	60
5.6 Picture of the DSA. . . . .	60
5.7 NACA 63 <sub>4</sub> – 021 shape of the 5-holes Pitot tube fairing (a) and fairing picture (b). . . . .	60
5.8 Comparison of $C_{loss}$ spanwise trends between CFD results and wind tunnel experiments for the baseline configuration. . . . .	62
5.9 Comparison of $C_{loss}$ spanwise trends between CFD results and wind tunnel experiments for the baseline configuration. . . . .	63
5.10 Planar $C_{loss}$ distributions from wind tunnel experiments for the baseline and the optimal configurations. . . . .	63
5.11 Comparison of planar $C_{loss}$ distributions for the baseline configuration of: (a) experimental data after interpolation, (b) CFD results. . . . .	65
5.12 Comparison of planar $C_{loss}$ distributions for the optimal configuration of: (a) experimental data after interpolation, (b) CFD results. . . . .	66
5.13 Planar distribution of the loss validation error $\epsilon$ for the optimal configuration. . . . .	67
5.14 Comparisons of spanwise distributions at the measurement plane of: (a) $C_{loss}$ of baseline and optimal configurations extracted from the CFD, (b) $C_{loss}$ of baseline and optimal configurations obtained through experiments, (c) $\Delta C_{loss}$ between the two configurations in according to CFD and experiments. . . . .	68



# LIST OF TABLES

2.1	Comparison of total pressure loss coefficient ( $C_L$ ) in CFD and experiments. Values of the overall losses, of the losses at the mid-span, and of the secondary losses. Hartland, Gregory-Smith and Rose [64], 2000. . . . .	28
4.1	Main geometrical characteristics of the cascade employed for the methodology verification. . .	39
4.2	Geometrical features of the baseline fence. Parameter names ( $x_i$ ) are referred to the parameterization illustrated in Sec. 3.2. . . . .	41
4.3	Geometrical features of the optimal fence. Parameter names ( $x_i$ ) are referred to the parameterization illustrated in Sec. 3.2. . . . .	44
4.4	Axial distance from the blade trailing edge of the section planes indicated in Fig. 4.9. Distance normalized to $s$ . . . . .	46



# LIST OF SYMBOLS AND ABBREVIATIONS

## Symbols

$\alpha_1$	inlet flow angle
$\alpha'_1$	inlet blade angle
$\alpha'_2$	outlet blade angle
$\Gamma$	circulation
$\delta_{ij}$	Kronecker delta
$\delta_{inlet}$	inlet boundary layer thickness
$\omega$	vorticity
$\theta$	flow deflection
$\mu$	dynamic viscosity
$\nu$	kinematic viscosity
$\nu_t$	turbulent viscosity
$\rho$	density
$\tau_{ij}$	Shear Stress Tensor
$C_{ax}$	blade axial length
$C$	blade chord
$C_{bf}$	baseline fence chord
$C_{of}$	optimal fence chord
$C_{LOSS}$	total pressure loss coefficient
$C_{SKE}$	secondary kinetic energy coefficient
$F$	surface forces
$H$	blade span length
$k$	turbulent kinetic energy
$KE$	kinetic energy
$p$ or $P$	pressure
$Re$	Reynolds number
$s$	blade pitch
$S_{ij}$	Mean rate shear stress tensor
$u$ or $V$	velocity
$u'_i$	turbulent velocity fluctuation
$X$	volume forces
$\overline{\quad}$	Averaged quantity
$-\overline{u'_i u'_j}$	Reynolds stress tensor

## Abbreviations

<i>AR</i>	aspect ratio
CFD	Computational Fluid Dynamics
DP	design point
$H_p$	pressure side leg of the horseshoe vortex
$H_s$	suction side leg of the horseshoe vortex
OIT	Osaka Institute of Technology
<i>R</i>	reattachment line
RANS	Reynolds averaged Navier-Stokes
RMS	root mean square
<i>S</i>	separation line
SKE	secondary kinetic energy
SST	Shear Stress Transport turbulence model
TKE	turbulent kinetic energy

## Subscripts

<i>baseline</i>	obtained with the baseline cascade geometry
<i>bulk</i>	property of the bulk flow
<i>CFD</i>	data provided by CFD
<i>exp</i>	data provided by the experiments
<i>in</i>	Inlet conditions
<i>optimal</i>	obtained with the optimal cascade geometry
<i>out</i>	outlet conditions
<i>S</i>	static property
<i>sec</i>	property of the secondary flow
<i>T</i>	total (or stagnation) property
<i>visc</i>	of viscous nature
<i>vortex</i>	property of a vortex

# 1

## INTRODUCTION

### 1.1. BACKGROUND

The current concern for global warming is pushing the research in turbines toward highly efficient solutions and designs. Indeed, around 30% [5] of the global greenhouse gas emissions are due to electricity production, and marine and aeronautical propulsion, all involving turbines as the main component in the process of power generation. In the field of aero engines, the efficiency is an even more stringent requirement than in the industry, as it determines the amount of fuel that must be carried and, in turn, the weight of the aircraft and the cost of the travel. In fact, for civil aviation, one of the major expenses in the overall cost is attributable to the fuel consumption. As a consequence, each aerodynamic component in an aero engine is studied and optimized in every detail, so to achieve the highest possible efficiencies reachable with a thermodynamic cycle. In recent years, thanks to the availability of high computational capabilities, the Computational Fluid Dynamics became an increasingly widespread tool for the aero/thermodynamic design of the aerodynamic components, also opening to the possibility of performing automatic CFD-based shape optimizations. Nowadays, the numerical optimization is a common mean used in the research environment to further push the growth in efficiency. In the frame of a global exertion addressed to keep raising the efficiency, a particular attention is dedicated to the reduction of *secondary losses* in turbine blade rows (Langston, [22]). In turbomachinery, secondary flow is defined as a vortical flow motion laying in the plane orthogonal to the main direction of the flow [7] (in the so-called *secondary plane*) at a section downstream of the blade trailing edge. The associated losses can amount to 30-50% of the total pressure losses (according to [6]) in highly loaded turbine cascades featuring particularly low aspect ratios and thickness-chord ratios, as those commonly used for the first stages (high pressure turbines or HPT). The detrimental effect of the secondary flow consists, other than in the waste of useful kinetic energy (becoming *secondary kinetic energy*), in significant energy dissipations caused by the formation of a large region of low-energy flow at the trailing edge of the blade. Here, different vortical structures are rounded up and interact with the blade wake, enhancing the production of mixing losses.

One of the methodologies proposed to mitigate this phenomenon is the addition of an endwall fence (Langston, [22]). An endwall fence is a small and thin surface applied to the endwall and positioned in the blade row passage. Its purpose is to obstruct the secondary flow development as shown in Fig. 1.2, so to mitigate the formation of the large area of low-energy flow at the blade trailing edge. Also, the fence obstructs the endwall crossflow and splits the endwall vorticity, reducing the overall secondary kinetic energy. However, the addition of the fence, leads to an increment in profile losses and creates another wake that, together, originate further losses. For this reason, a fence should be designed in such a way that the reduction of fluid-dynamic losses due to the mitigation of secondary flows exceeds the extra profile losses. Different authors in the past studied the sensitivity of the turbine cascade efficiency to the fence geometrical parameters. Also, many experiment-based optimizations have been performed to find optimal configuration and demonstrate the effectiveness of this methodology. However, no work has ever been done with the aim of providing a universal mean for the efficient design of endwall fences, as those results were applicable only to the cascades investigated, with the flow conditions used. In fact, the appropriate fence shape for a certain blade row, strictly depends on the secondary flow characteristics and the secondary flow relevance with respect to the overall energy losses. These aspects, and in turn the optimal fence geometry, are sensitive to:

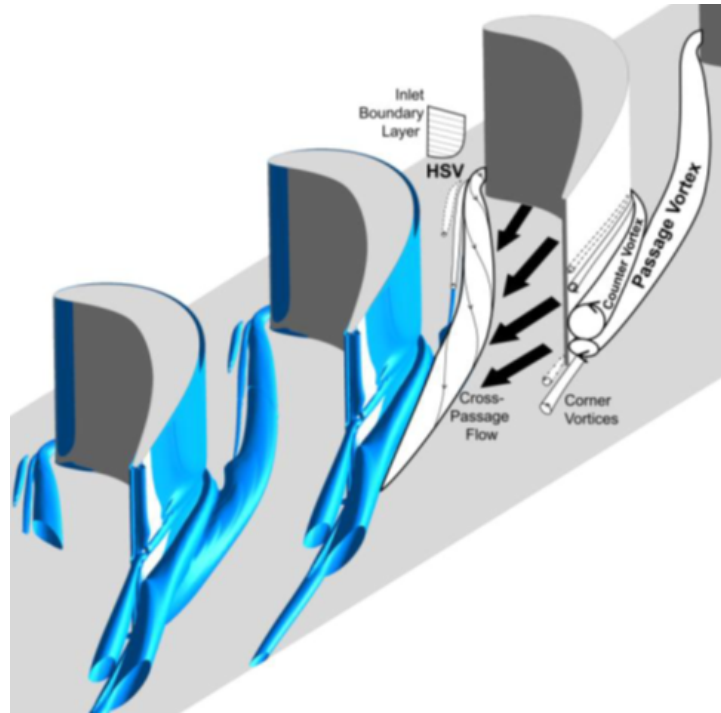


**Figure 1.1:** Representation of the secondary flow development and interaction, Coull [3], 2016.

- Blade loading: it acts on the crossflow strength, determining dimensions, strength and migration pattern of the passage vorticity.
- The inlet boundary layer thickness and velocity profile: these affect the size and the strength of the inlet endwall vorticity.
- Reynolds number: it changes the entity of secondary losses, which is a property related to the fluid momentum, w.r.t. the wall shear.
- The blade aspect ratio: it impacts the relevance of the endwall effects ([4]) w.r.t. the overall losses of the cascade.

According to these conditions, the fence geometry must be adapted in order to intercept and split the inlet boundary layer vorticity, adjusting its dimensions depending on the importance of secondary losses in the cascade. For these reasons, every study on the fence shape produces results that cannot be of any help for the design of other cascades. The design of such devices is therefore usually obtained via lengthy and time-consuming experimental campaigns. However, shape optimization can greatly enhance the design procedure in terms of both efficiency and efficacy, allowing the investigation of a large number of configurations at affordable computational power. For this reason, a CFD-based automated design is a powerful and quick way to determine the best fence shape for a certain application.

## 1.2. RESEARCH QUESTIONS AND OBJECTIVES

*The main goal of this work is the development of an efficient design tool for endwall fences and to assess the impact of fence design on secondary losses mitigation.* By developing and testing this framework, the following research questions can be answered:

- **What is the performance gain attainable with an optimal fence shape in terms of reduction of total pressure losses?**
- **What is a suitable optimization methodology for fence design?**
- **What is the accuracy of CFD models in predicting secondary flow-induced losses?**

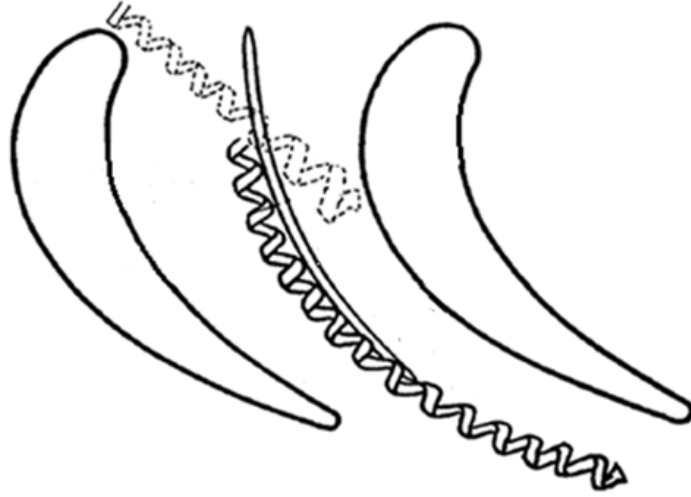


**Figure 1.2:** Schematic representation of fence blocking the horse-shoe vortex migration, Chung and Simon [58], 1993.

The fulfillment of the main research objective enables to accomplish the following other objectives:

1. **Demonstrate the feasibility of computational methodologies for the automatic generation of fence geometries and mesh.**
2. **Verify that the methodology can be successfully utilize to attain an optimal fence design for the turbine cascade used as test case.**
3. **Gain insight of the physical flow mechanisms triggered by the fence that allow to mitigating the secondary flow in turbine cascades.**
4. **Prove the accuracy of the design procedure by validating the optimal shape improvement against wind tunnel experiments.**

### 1.3. ORIGINAL CONTRIBUTION OF THIS WORK

In this work, a framework for the automatic generation of fence geometries and the launch of CFD simulations is devised to efficiently create and test many configurations; the simulation results are then fitted to create a mathematical model correlating the values of the geometry parameters to the resulting cascade performance. The efficiency of the methodology, allows to increase the number of optimization variables with respect to those previously investigated in the past. The parameters optimized in the past have been:

- Pitchwise position
- Height (and height distribution successively)
- Length
- Thickness

The additional parameters hereby introduced are:

- Streamwise position
- Thickness distribution
- Camberline shape

Given that the generation and simulation of geometries is automatic, the combined effects of all the mentioned parameters assuming many different values can be assessed. The creation of a surrogate model provides the capability of predicting the performance of a whichever fence configuration without running any additional simulation. Therefore, the full parameterization, the large number of tests, and the surrogate model, widened the “choice” of the optimal fence to all the possible shapes.

## 1.4. OUTLINE OF THE THESIS

This thesis collects the most important aspects of the research process that led to the development and test of the design framework, and reports them in the same order as they were performed.

- Ch. 2: brings together all the main investigations on the secondary flow phenomenon, its mitigation techniques and previous knowledge about endwall fence. A section is dedicated to the issues related to the CFD modeling of secondary flows, and another regards the different algorithms that can be employed in response surface optimizations.
- Ch. 3: regards the numerical methodology and the aspects of its development.
- Ch. 4: the outcomes of the methodology applied to the test case are analyzed to investigate the loss reduction mechanisms and assess the performance improvements.
- Ch. 5: the fluid dynamic performance improvements are experimentally validated.
- Ch. 6: the conclusions and the recommendations for future studies are presented.

# 2

## THEORETICAL BACKGROUND

This chapter gathers the background knowledge acquired for carrying out this research. Sec. 2.1 provides the mathematical background on vorticity dynamics and general secondary flow generation in bent ducts. Sec. 2.2 deepens the topic of secondary flow in turbine cascades: the models developed are outlined, separation and loss mechanisms are explained, minor detrimental effects are discussed and the sensitivity of the phenomenon to the cascade parameters is addressed. In Sec. 2.3 all the existing mitigation techniques for the secondary flow are described, while a separate section is dedicated to the researches about the endwall fence in Sec. 2.3.5. Sec. 2.4 is dedicated to the difficulties encountered in past researches by the authors in correctly predicting the secondary flows with CFD simulations. Conclusively, Sec. 2.5 regards the technique of the response surface optimization and its sub-elements, focusing on the algorithms available in the framework used, namely Ansys Workbench.

### 2.1. BASIC CONCEPTS OF FLOW VORTICITY AND SECONDARY FLOWS GENERATION

Secondary flows originate from the boundary layer vorticity of a flow that passes through a curved duct. The definition of vorticity is:

$$\boldsymbol{\omega} = \nabla \times \mathbf{u} \quad (2.1)$$

Therefore, considering a mono-directional flow, the velocity profile of the boundary layer has one only vorticity component (Fig. 2.1), i.e. the component orthogonal to the flow direction and parallel to the wall. If the  $x$  axis is aligned with the flow direction and the  $y$  axis is perpendicular to the wall, the vorticity component of such a basic flow is aligned with the  $z$  axis, and is:

$$\omega_z = -\frac{\partial u}{\partial y} \quad (2.2)$$

where  $u$  is the local velocity along the  $x$  direction. Substituting Eq. 2.2 within the definition of the shear stress yields:

$$\tau_{x,y} = \mu \frac{\partial u}{\partial y} = -\mu \omega_z \quad (2.3)$$

assuming the fluid to be Newtonian. More specifically, substituting Eq. 2.2 into the momentum equation for the boundary layer, leads to:

$$\frac{1}{\rho} \frac{dp}{dx} = \nu \frac{\partial^2 u}{\partial y^2} \Big|_{y=0} = -\nu \frac{\partial \omega_z}{\partial y} \Big|_{y=0} \quad (2.4)$$

Eq. 2.4 describes the generation of vorticity at the solid surface as a diffusion along the wall-normal direction produced by the streamwise pressure gradient. More in general, the creation of vorticity can be ascribed to the free-stream conditions [7], as it can be expressed by rewriting the momentum equation in  $x$  direction and substituting Eq. 2.4 with the pressure gradient:

$$\frac{\partial u_E}{\partial t} + u_E \frac{\partial u_E}{\partial x} = \nu \frac{\partial \omega_z}{\partial y} \Big|_{y=0} \quad (2.5)$$

A complete equation for the vorticity can be obtained from the general form of the momentum equation:

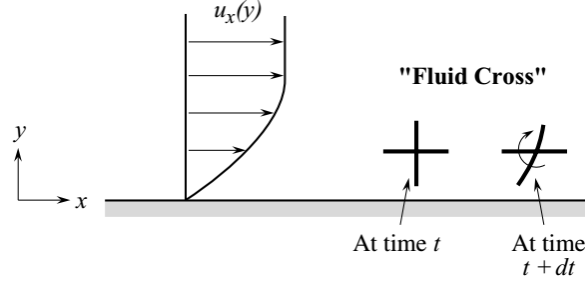


**Figure 2.1:** Example of boundary layer velocity profile and rotation of the fluid element due to the vorticity (Greitzer [7], 2004).

$$\frac{\partial \mathbf{u}}{\partial t} + \mathbf{u} \cdot \nabla \mathbf{u} = -\frac{1}{\rho} \nabla p + \mathbf{X} + \mathbf{F}_{visc} \quad (2.6)$$

where  $\mathbf{X}$  are the volume forces and  $\mathbf{F}_{visc}$  are the surface forces acting on the fluid element. Applying the curl to the Eq. 2.6 and making use of some vector identities the vorticity equation is (derivation can be found in [7]):

$$\frac{D\omega}{Dt} = \frac{\partial \omega}{\partial t} + (\mathbf{u} \cdot \nabla) \omega = (\omega \cdot \nabla) \mathbf{u} - \omega (\nabla \cdot \mathbf{u}) - \nabla \times \left( \frac{1}{\rho} \nabla p \right) + \nabla \times \mathbf{X} + \nabla \times \mathbf{F}_{visc} \quad (2.7)$$

where:

- $\frac{\partial \omega}{\partial t}$  describes the vorticity variation generated for flow unsteadiness
- $(\mathbf{u} \cdot \nabla) \omega$  is the convection term
- $(\omega \cdot \nabla) \mathbf{u}$  accounts for the tilting and stretching of vorticity due to velocity gradients
- $\omega (\nabla \cdot \mathbf{u})$  is related to the diffusion of the vorticity for compressibility effects
- $\nabla \times \left( \frac{1}{\rho} \nabla p \right)$  can be developed as:

$$\nabla \times \left( \frac{1}{\rho} \nabla p \right) = \frac{1}{\rho} (\nabla \times \nabla p) - \frac{1}{\rho^2} \nabla \rho \times \nabla p = -\frac{1}{\rho^2} \nabla \rho \times \nabla p$$

with  $\nabla \times \nabla p = 0$  as a curl of a gradient is always null. It describes the generation of vorticity occurring when a pressure gradient impresses a moment on a fluid particle with non-uniform density distribution.

- $\nabla \times \mathbf{X}$  moment impressed by a body force
- $\nabla \times \mathbf{F}_{visc}$  moment impressed by a surface force

The vorticity, being a solenoidal field, is usually visualized as infinite vortical lines. Considering a turning duct like that in Fig. 2.2 and a flow entering with its endwall vorticity, there will be a component of that vorticity aligned with the streamwise direction at the duct outlet, namely the creation of a secondary flow. Assuming the flow to be inviscid, incompressible, steady and with no body forces, Eq. 2.7 becomes:

$$(\mathbf{u} \cdot \nabla) \omega = (\omega \cdot \nabla) \mathbf{u} \quad (2.8)$$

From Eq. 2.8, can be seen that the term  $(\omega \cdot \nabla) \mathbf{u}$  changes the direction and intensity of  $\omega$  because of the velocity gradient across the duct section. In fact, as accurately explained in [7], when the flow turns, the particles flowing in the outside of the curve will proceed with lower velocity, and for a longer distance, than those in the inside. As a consequence, the associated vortex filament is distorted being convected by the inner and faster fluid, as shown in in Fig. 2.2. However, the term  $(\omega \cdot \nabla) \mathbf{u}$  is only a worsening factor for the generation of secondary flow. Indeed, even without taking into account its effects, the vorticity would keep the same direction as at the turning entrance, ending up with a component parallel to the main flow.

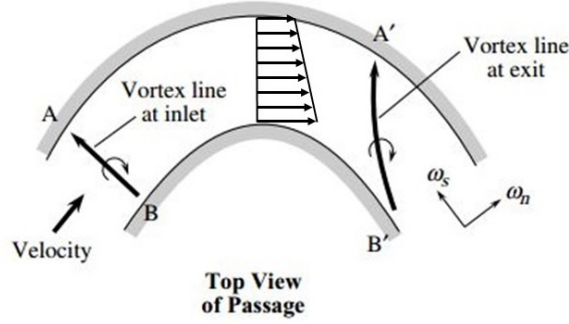


**Figure 2.2:** Distortion of the vortical filament due to the non-uniform velocity distribution in the bend and generation of streamwise vorticity (Greitzer [7], 2004).

Consequently, the secondary flow creation is due to a combination of these two effects on the boundary layer vorticity that approaches a bent orthogonally: a conservation of the rotational momentum and a deflection of the vortex toward the streamwise direction caused by the velocity gradient in the duct.

A simplified model of the secondary flow downstream a turning has been obtained by Squire and Winter [8]:

$$\omega_s = -2\omega_i \Delta\theta \quad (2.9)$$

with  $\omega_s$  the outlet streamwise vorticity,  $\omega_i$  the inlet vorticity normal to the main flow and  $\Delta\theta$  the flow deflection. The previous model, however, assumes a fairly constant radius of curvature. A more general model has been developed by Lakshminarayana and Horlock [9] obtaining the outlet streamwise vorticity  $\omega_s$  as a function of the gradient of the total pressure  $p_t$ , starting from the equation of vorticity and transforming them with an intrinsic coordinate system. The resulting model consists of the following equation:

$$\frac{\partial}{\partial l} \left( \frac{\omega_s}{u} \right) = - \frac{2}{\rho u^2 r_c} \frac{\partial p_t}{\partial b} \quad (2.10)$$

where  $r_c$  is the local curve radius,  $l$  is the local coordinate along the streamline,  $b$  is the coordinate orthogonal to  $l$  and to the curve radial direction  $n$ .

From the previous derivations, it is clear that the generation of secondary flow, despite having a viscous origin, i.e. the viscosity in the boundary layer, is actually an inviscid mechanism.

Secondary flows are typically encountered in turbomachinery cascades, because of the presence of endwall vorticity being convected when passing through a bladed channel. as shown in Fig. 2.3. In turbomachinery, blade shapes and gradients of pressure (or sometimes even temperature), contribute to creating additional vortical structures, leading to a highly three-dimensional flow that is characterized in detail in the following sections.

## 2.2. SECONDARY FLOWS IN TURBOMACHINERY

### 2.2.1. THE SECONDARY FLOW PICTURE

The first representation of the vortex system downstream to a turbine was developed by Hawthorne in 1955 [11]. As can be seen in Fig. 2.4, it consists in the classic secondary flow theory with the addition of a vortex sheet at the blade trailing edge, due to the non-uniform spanwise distribution of circulation around the blade. He called *passage vortex* the vortex in the center of the passage, caused by the above explained process related to the flow deflection, and *trailing shed vorticity* the wake of vortices released by the blade trailing edge.

The presence of the passage vortex in the center of the cascade was confirmed by the smoke visualization experiments of Herzig et al. [12]; however, measurements provided by Armstrong [13] showed that the distribution of secondary velocity downstream a stator cascade hardly resembles the simple representation of Hawthorne.

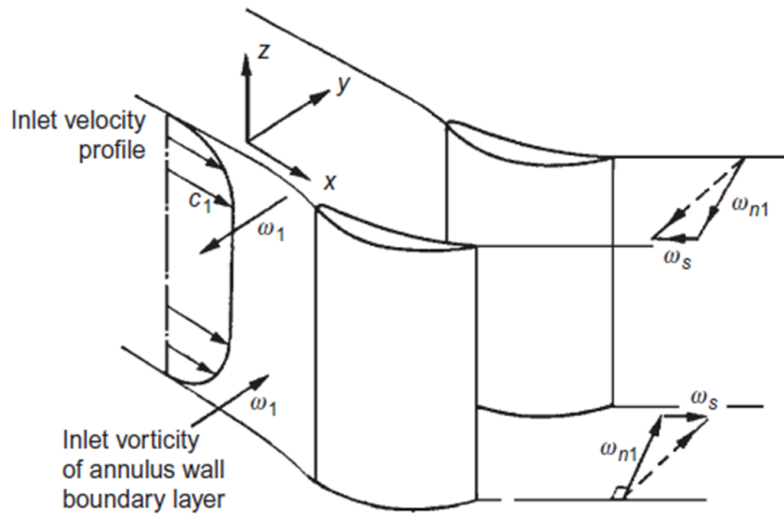


Figure 2.3: Generation of secondary flow in a turbine cascade due to the flow deflection (Dixon et al. [10], 2014).

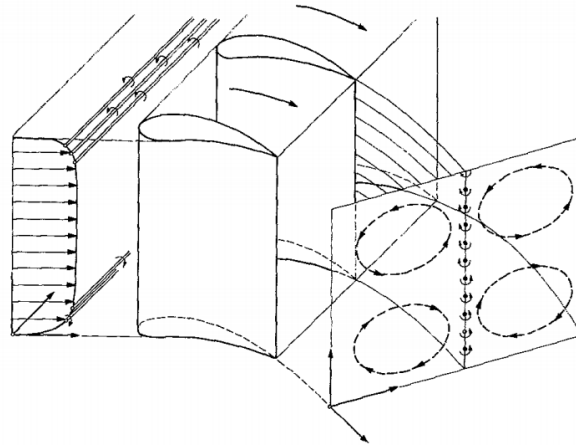
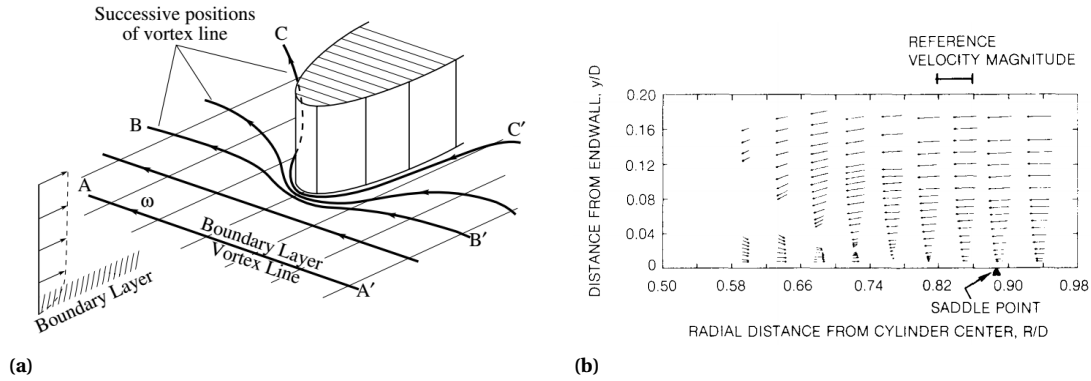


Figure 2.4: Classical representation of secondary flow in turbine cascade. (Hawthorn [11], 1955).

In [14] Klein mentions the formation of a *stagnation point vortex* at the blade leading edge of a cascade. This vortical phenomenon, usually referred as *horseshoe vortex*, is well-known and studied in the literature; it consists in the endwall boundary layer separation in front of an obstacle. An intuitive explanation is provided in [7] with the representation of the vorticity as vortical lines, Fig. 2.5 (a). If we imagine a plane parallel to the flow and passing for the stagnation point, when the flow approaches the obstacle, the particles moving along this plane will gradually slow down because of the adverse pressure gradient; on the opposite, those passing away from this plane will accelerate. For this reason, the associated vortical lines will be stretched and turned, wrapping, at the end, around the obstacle. From the study of Eckerle and Langston [15], we can see in Fig. 2.5 (b) the vortex creation by boundary layer separation that takes place in the above-mentioned plane: after a separation at the so-called *saddle point*, the boundary layer turns toward the endwall in front of the stagnation point, creating what seems like a corner vortex. According to Osnaghi [16], the downward turning is due to a pressure gradient developing in the following way: the boundary layer, having non-uniform velocity but same pressure, recovers all the total pressure at the stagnation point. As a consequence, being the velocity higher in the free-stream flow, also the recovered pressure will be higher than inside the boundary layer, creating the pressure gradient that drives the flow turning in Fig. 2.5 (b). Such a vorticity diffuses to the adjacent flow particles that keep rotating while proceeding downstream, with a component of this rotation turned toward the streamwise direction. Therefore, the horseshoe vortex is an additional source of secondary flow and its gen-

eration takes place also at the blade leading edge. Indeed, as successively demonstrated by Bölcs in [17], he



**Figure 2.5:** Representations of the horseshoe vortex formation: (a) schematic of boundary layer vortical lines wrapping around an object (Greitzer [7], 2004), (b) velocity vectors showing boundary layer separation upstream of an object that leads to the horseshoe vortex (Eckerle and Langston [15], 1986).

assumed that the near-wall flow around a blade leading edge and around a cylinder had the same characteristics, thus he added to the representation of Hawthorn the horseshoe vortex as shown in Fig. 2.6 (a). In the case of a blade cascade, however, given the asymmetric shape of the blade section, the two legs of the vortex have different patterns: the pressure side leg  $H_p$  crosses the passage as it is pulled toward the blade suction side, while the suction side leg  $H_s$  remains attached to the blade surface. According to this representation, however, the  $H_p$  remains a different entity with respect to the passage vortex and the  $H_s$  is dissipated interacting with the passage vortex. Conversely, Langston et al. showed in [18], supported by experimental results, that the pressure side leg of the horseshoe vortex and the passage vortex were actually merging, as they rotate in the same direction. Furthermore, they showed that the suction side leg, rotating in the opposite way and therefore called *counter vortex*, is not quickly dissipated but is still present downstream the cascade. The representation of Langston et al. is in Fig. 2.6 (b). Here, as well as in the figure, they also mention the role of an additional actor: the *endwall crossflow*, which is an extra secondary flow source due to the pressure gradient between the blade pressure surface and the suction surface. This pressure gradient is relevant only at the endwall because of the low momentum of the boundary layer flow. According to Langston et al., specifically, the interaction of

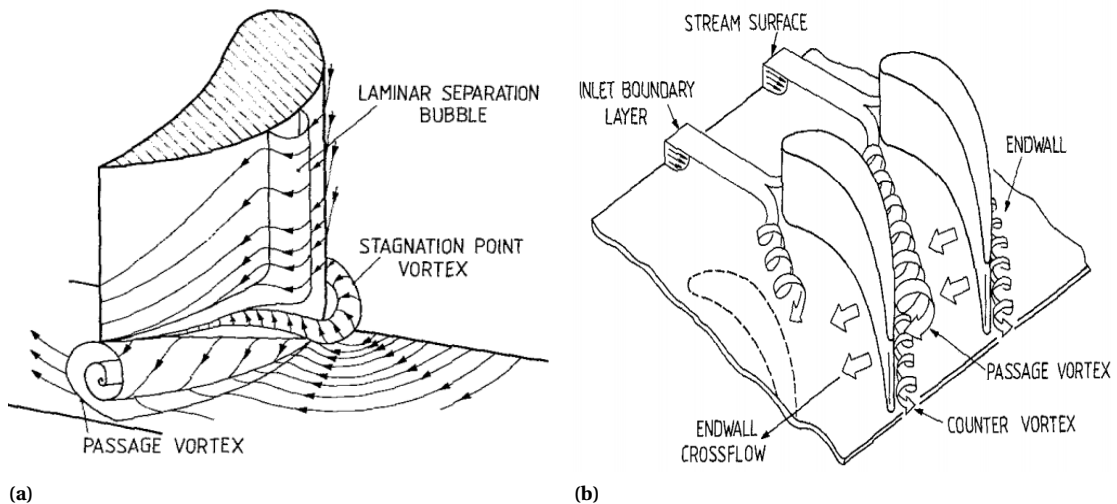


**Figure 2.6:** Comparison between secondary flow representations according to Klein [14] (a) and Langston [18] (b).

the passage/ $H_p$  vortex and the counter/ $H_s$  vortex resembles the planetary orbit, as the counter vortex wraps and rotates around the passage vortex exactly as a planet around a star. The mechanism of their evolution and interaction has been also observed by Sieverding and Van den Bosch in [20]: they marked the upstream flow

with smoke at two different blade span (Fig. 2.7), one inside and one outside the boundary layer, and they observed the planetary motion of the counter vortex around the passage vortex, concluding that the outlet position of the former depends on the rotational speed of the latter.

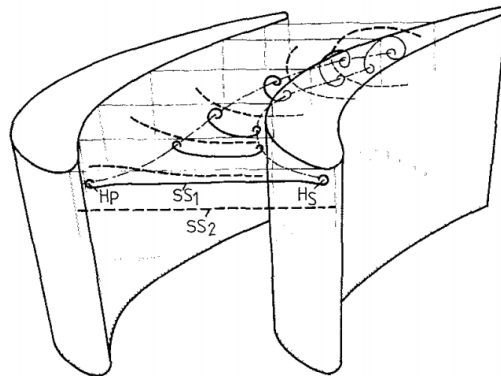


**Figure 2.7:** Streamwise evolution of the secondary flow according to smoke visualization experiments carried out by Sieverding and Van den Bosch, [20], 1983.

In [21] Sieverding points out the existence of two vortices at the junction between endwall and blade walls, called *corner vortices*. At these corners, in fact, the boundary layers of the two surfaces merge, so the flow has very low energy and the passage vortex puts such flow into rotation.

Sharma and Butler [6] discovered by experimental observations that the counter vortex wraps around the passage vortex as sketched in Fig. 2.8. In [23], Goldstein and Spores report the presence of another minor vortex

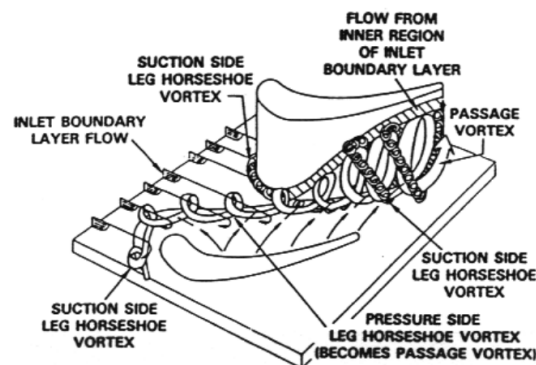


**Figure 2.8:** Sketch of secondary flow as observed by Sharma and Butler[6], 1987.

identified at the junction between endwall and blade leading edge, which they called *leading edge corner vortex*. They found an unexpectedly high mass transfer rate in the junction at the Reynolds number of the engine at operating conditions, too high and localized to be ascribed to horseshoe vortex, so they postulated its existence. However, only in [24] the vortex has been observed, leading to the vortex pattern displayed in Fig. 2.9. Similarly to the other corner vortices, this is due to the low energy flow at the junction that is put into rotation by the horseshoe vortex.

### 2.2.2. LIMITING STREAMLINES TOPOLOGY

The *limiting streamlines*, or limiting lines, are those streamlines attached to a body surface. Their visualization provides an insight in the flow field at the wall, showing, in particular, the presence pressure gradients or boundary layer separation. As the formation of the horseshoe vortex is caused by boundary layer separation (Sec. 2.2.1), the vortex pattern can be traced by investigating the topology of the limiting lines on the endwall and on the blade suction surface. In [18] Langston et al. presented a scheme of ink traces of the limiting streamlines that they obtained, reported in Fig. 2.10.  $R$  is the *reattachment line*, the streamline ending in the stagnation point and  $S$  is the *separation line*, divided in the pressure side part  $S_p$  and the suction side  $S_s$ .  $R$

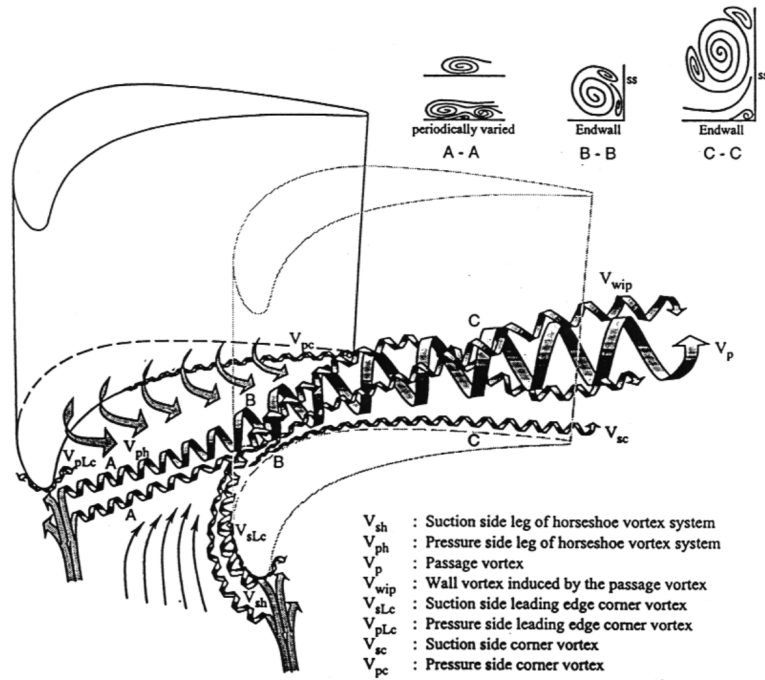


Figure 2.9: Secondary flow representation of Wang, Olson, Goldstein and Eckert [24], 1997.

divides the flow that is about to deviate its pattern toward the suction side from that going for the pressure side. At the intersection between  $R$  and  $S$  there is the *saddle point*  $A$ , where the separation starts and from where it propagates along the  $S$  line; here the boundary layer starts to roll up becoming the passage vortex or the counter vortex, accordingly. The  $S_p$  line continues on the blade suction side, with the passage vortex causing three-dimensional separation. The authors reported that the topology of these streamlines depends on the flow incidence angle.

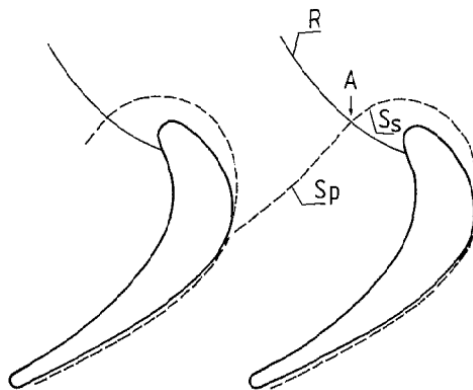


Figure 2.10: Separation lines in a turbine cascade from the endwall flow visualization experiment of Langston et al. [22], 1977.

In [21], Sieverding improved the description of the endwall limiting lines referring to flow visualizations of different authors (Belik [25], Sjolander [26], Marchal and Sieverding [27], Moore [28], and Gotthardt [29]). As displayed in his drawing in Fig. 2.11, there are a primary and a secondary separation line, respectively  $S_1$  and  $S_2$ , as well as two saddle points,  $A_1$  and  $A_2$ . As you can see in Fig. 2.11 (c) along the primary separation line takes place the actual flow separation while the secondary line is the trace of the “lift-off” of the passage vortex. Depending on the strength of the crossflow between  $S_{1,p}$  and  $S_{2,p}$ , there can be strong or weak interaction with the blade suction side, both shown in Fig. 2.11 (d): in the case of strong interaction, the generation of a corner vortex occurs (visible from the reattachment line  $R_{2,p}$ ) and the related separation line  $S_3$  will be visible, while if weak interaction takes place there will be just the  $S_{2,p}$  flowing along the blade wall. On the blade suction side,  $S_{1,s}$  joins  $S_{2,s}$  immediately downstream and climbs the suction surface until the counter vortex is entrained

and detached by the passage vortex rotation, shown in Fig. 2.11 (b). A corner vortex at the junction between blade pressure surface and endwall is also shown by the reattachment line named  $R_5$ .

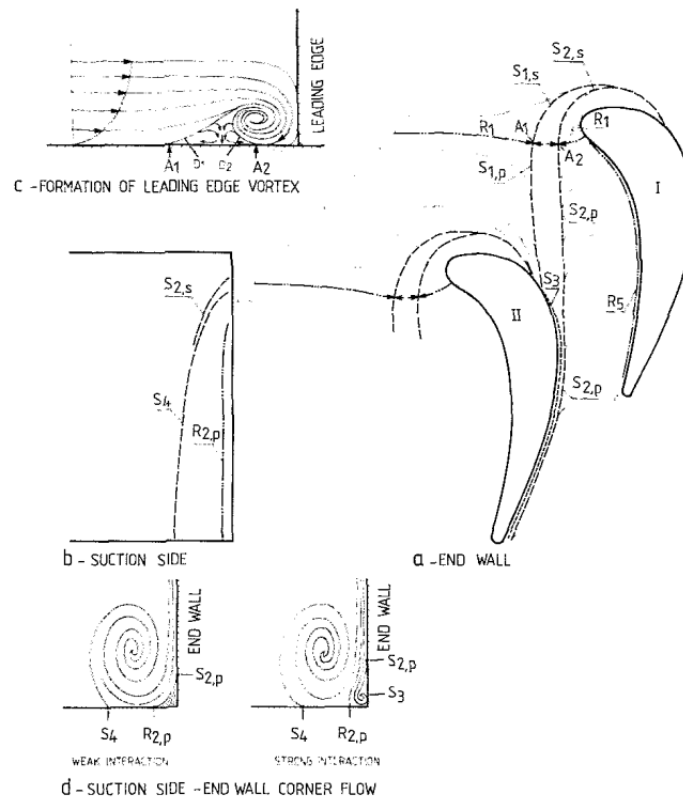


Figure 2.11: Drawing of separation lines in a cascade, Sieverding [21], 1985.

### 2.2.3. SECONDARY LOSS GENERATION AND EVOLUTION

In [21] Sieverding provided a full characterization of the secondary loss mechanisms in a turbine cascade. He accounted the following secondary-induced phenomena as responsible for the fluid-dynamic losses:

1. Boundary layer, before the separation in  $S_1$  (inlet boundary layer, which is lifted and becomes the passage vortex) and after the  $S_2$  (where a new boundary layer is created).
2. Separation bubble located between  $S_1$  and  $S_2$ .
3. Viscous dissipation at the corner vortices of both suction and pressure side.
4. The shear action of the passage vortex on the separated area of the blade suction surface.
5. Mixing of vortices and wake with the main flow downstream the cascade.

1) When the inlet boundary layer separates becoming the passage vortex, it carries its low energy flow downstream. After  $S_2$ , energy is drained from the main flow for the formation of the new boundary layer; this is subject to the sweeping action of the crossflow and entrained in the passage vortex, enlarging the loss region. 2) The separation, propagating to the blade suction surface along the line  $S_4$  (Fig. 2.11), creates a separation bubble that is released at the blade trailing edge as an additional loss peak region. The spanwise penetration of  $S_4$  depends on the magnitude of the vortex and the strength of the crossflow. 3) The crossflow feeds the corner vortex at the junction, where further total pressure is dissipated and another loss area is created. 4) The skin friction of the crossflow on the separated area of the suction surface enlarges the loss core carried by

the passage vortex. 5) Downstream to the cascade, the remaining secondary kinetic energy expands these loss regions by mixing out the main flow with the low energy flow.

In Fig. 2.12 examples are provided of plots showing loss spanwise distributions downstream a blade row. Due to the loss sources mentioned above, three regions of loss concentration can be identified according to the position of:

- corner vortex
- passage vortex (the core of the losses is not always coinciding with the vortex core [31])
- separation line  $S_4$  (Fig. 2.11)

The examples in Fig. 2.12 are shown for increasing blade loading. Sieverding [21] studied the variation in the trend of the spanwise loss plots with respect to the position of these listed loss regions. Fig. 2.12 (a) shows the distribution downstream a cascade where the passage vortex is very small and the corner vortex is weak; both things indicate that the blade loading is rather low, otherwise both passage and corner vortex would have been enlarged by the passage crossflow. Also, there is no evidence of the peak related to the separated flow. The inlet boundary layer thickness  $\delta_{inlet}$  must be small as well, otherwise the passage vortex would have been visible. The effects of a larger loading, with a larger passage vortex are shown in Fig. 2.12 (b) from the presence of a bump; in Fig. 2.12 (c) a detached peak indicates a well lifted and larger vortex, with a region of high loss level between the peak and the endwall due to the merging of areas associated with corner vortex and passage vortex. A change from (b) to (c) can also be achieved with an enhancement of  $\delta_{inlet}$ . The low energy flow coming from the separation line  $S_4$ , instead, is detached from the passage vortex only for higher loadings, in Fig. 2.12 (d).

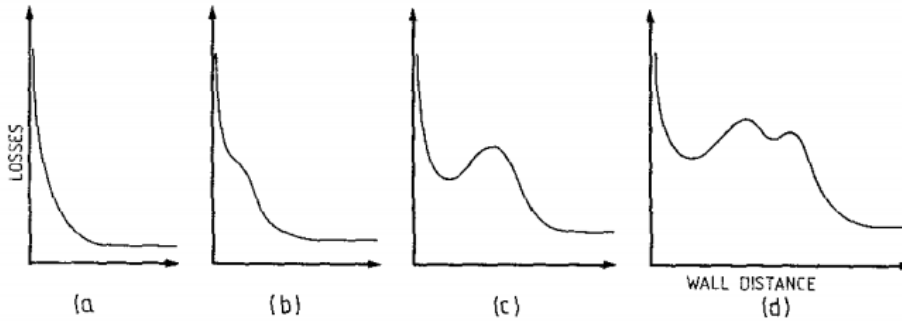


**Figure 2.12:** Examples of spanwise distributions of losses downstream a cascade for increasing blade loadings, Sieverding [21], 1985.

In an attempt to understand the correlation between the spanwise extension of the passage vortex loss region  $b$  and the  $\delta_{inlet}$ , Sieverding [21] draws three conclusions:

- $b > \delta_{inlet}$ : the passage vortex is always enlarged going across the passage, never dissipated.
- $b/\delta_{inlet}$  depends on the blade loading: this, in turn, causes the crossflow whose strength determines the increase of  $b$ , as can be seen in Fig. 2.13 from the different lines.
- $b = f(\delta_{inlet})$  is not linear: the ratio presents asymptotical behavior for increasing  $\delta_{inlet}$ .

In [32], Perdichizzi et al. analyzed the flowfield downstream the cascade and derived the planar distribution on the turbulent kinetic energy ( $TKE$ ) production, which is the main source of loss generation. Defining the production term  $P$  as:

$$P = - \sum_{i,j} \overline{u'_i u'_j} \cdot S_{i,j} \quad \text{where} \quad S_{i,j} = \frac{1}{2} \left( \frac{\partial U_i}{\partial x_j} + \frac{\partial U_j}{\partial x_i} \right) \quad (2.11)$$

The  $S_{i,j}$  is the mean strain rate tensor,  $\overline{u'_i u'_j}$  is the Reynolds stress, and  $U_i$  is the main velocity component, all calculated from five holes probe measurements. The results of their analysis was that, as expected, the peaks of TKE production are on both sides of the wake and on the vortex region, particularly in correspondence of the strong spanwise crossflow on the blade suction surface.

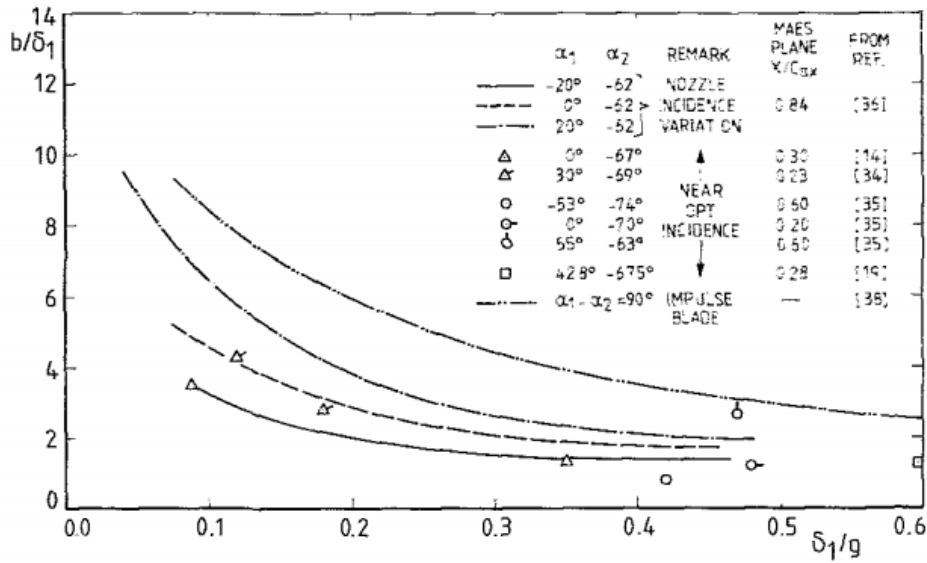


Figure 2.13:  $b/\delta_{inlet}$  trends as a function of  $\delta_{inlet}/g$  ( $g$  is the blade pitch) for different blade loadings, Sieverding [21], 1985.

#### 2.2.4. ADDITIONAL SIDE EFFECTS OF SECONDARY FLOWS

On top of a remarkable impact on fluid-dynamic losses, secondary flows induce additional effects on the aerothermodynamic characteristics of the flow:

1. lift reduction on the blade, implying a decrease in outlet flow momentum
2. underturning of the outflow, resulting in reduced overall flow turning
3. increased heat transfer, problematic for blades requiring cooling

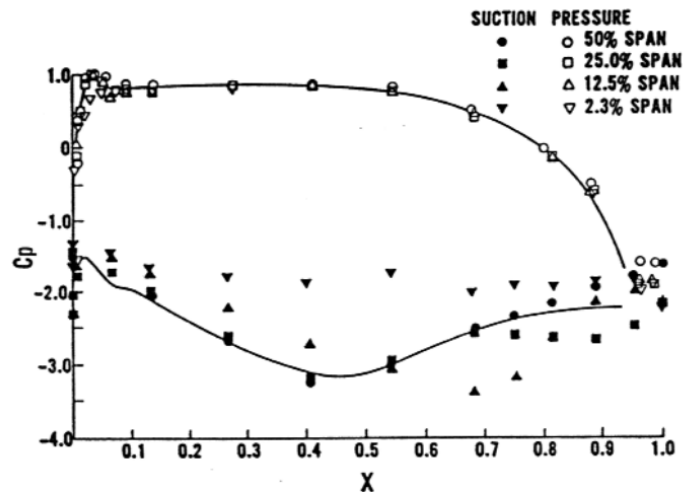
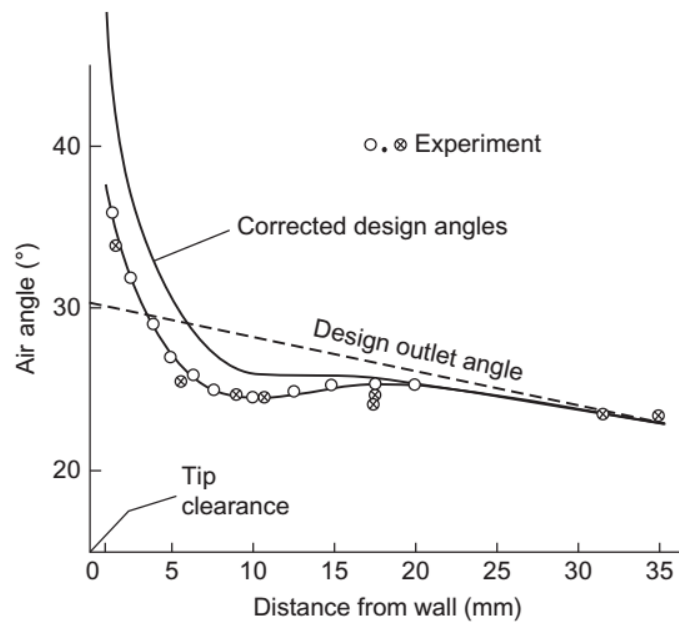


Figure 2.14: Distributions of static pressure coefficient around a blade at different span locations, Langston et al. [18], 1977.

The lift reduction occurs because of the three-dimensional separation caused by the passage vortex at the blade suction side. The presence of a low energy fluid around the separated area decreases the blade circulation in the endwall region. A prove of this effect has been provided by Langston et al. in [18]: they measured the pressure coefficient distribution at different blade spans with the results displayed in Fig. 2.14. It can be observed that, at 50% of the span the distribution perfectly matches the two-dimensional behavior (solid

line), except for the trailing edge separation; then, at lower span locations, while the pressure side distributions keep following the line, at the suction side the pressures are higher. As the lift at each section is the integral of the pressure difference between suction side and pressure side, this upward shift of the suction side curves indicates a reduction in blade lift and, as a result, a reduction in outflow momentum.



**Figure 2.15:** Comparison of outlet flow angle between design distribution and actual distribution, affected by the under and over-turning due to the secondary flow. Dixon [10], adapted from Horlock, 1963.

The flow underturning, instead, is an effect due to the influence of the secondary flow component on the design outflow velocity. In practice, the vorticity of the passage vortex reduces the effective outflow angle of the cascade, therefore decreasing the work extracted at the rotor. As can also be observed in Fig. 2.15, a phenomenon of *overtuning* takes place as well, but it is always of minor importance as it is confined on the endwall side of the passage vortex.

A last detrimental effect of the secondary flow is the increase of heat transfer between fluid and surfaces. This is an issue for high pressure turbines, where film cooling is adopted to allow the flow temperatures to be higher than tolerated by the blade material. In fact, the passage vortex carries the high temperature fluid from the middle of the passage to the endwall and the blade surface, sweeping away the film cooling. A comprehensive explanation and investigation of the phenomenon is reported in [19].

### 2.2.5. PARAMETERS INFLUENCING THE EVOLUTION OF SECONDARY FLOW

Sieverding [21] reported the following observations on the influence of flow conditions on the downstream planar loss distribution, provided by general trends noted in different previous investigations:

- For increasing inlet flow angle the passage vortex is pushed toward the blade suction surface.
- For smaller inlet boundary layer the passage vortex is shifted toward the blade suction surface and the endwall.
- For aspect ratios smaller than the critical aspect ratio (i.e. value for which the secondary flows of upper and lower endwalls interact with each other) passage vortex cores are pushed toward the endwall.
- The increase in outlet Mach number does not affect the passage vortex position, for  $M$  ranging between 0.1 and 0.8.

Successively, other authors investigated more extensively the influence of these and other parameters on the secondary flow development. The most influential parameters and conditions are:

- Blade loading
- Mach number
- Reynolds number and boundary layer thickness
- Aspect ratio

#### BLADE LOADING

The blade loading is the force that the turbine blade undergoes as a consequence of the flow deflection and acceleration. This is affected by the following parameters:

- inlet flow velocity
- incidence angle
- pitch-chord ratio
- the blade camber and thickness distribution

The influence of blade loading has been studied by varying the flow incidence angle ( $\alpha_1$ ) and the pitch-chord ratio.

In [33] Yamamoto and Nouse investigated the effect of largely varied incidence angle, concluding that:

- the passage vortex is stronger and the accumulation of low energy flow on the blade suction side is more relevant for high values of  $\alpha_1$ .
- for largely negative incidence angles the flow on the blade pressure side separates and the weak passage vortex entrains it, resulting in a wide region of losses downstream the cascade.
- for largely negative  $\alpha_1$  the counter vortex becomes particularly relevant.

Perdichizzi et al. studied the effects of the incidence angle and the pitch-chord ratio in [35]. Their main results are:

- a mathematical interpretation of the blade loading relation with the passage vortex intensity obtained by rewriting Eq. 2.7 in intrinsic coordinates as:

$$\frac{D\omega_s}{Dt} = \omega_s \frac{\partial u}{\partial s} + \omega_n \frac{\partial u}{\partial n} + \omega_z \frac{\partial u}{\partial z} + \nu \nabla^2 \omega_s \quad (2.12)$$

where, neglecting the viscous term and considering  $\omega_z$  and  $\omega_s$  null at the passage entrance, the growth of the inlet vorticity  $\omega_s$  only depends on the term  $\frac{\partial u}{\partial n}$ . For increasing loading, larger velocity gradients are generated between suction and pressure side, and so larger crossflow at the endwall is formed.

- the assessment of influence of pitch-chord ratio, achieved by changing the blade pitch  $s$ . For reduced solidity the secondary flow increases; such an effect takes place regardless the value of incidence angle, but the growth is much greater at large  $\alpha_1$ .
- the observation of the passage vortex reaching the critical point, i.e. where the secondary flow of both endwalls interact (Fig. 2.16), increasing the losses dramatically.

In Fig. 2.16, losses are defined using the kinetic energy loss coefficient  $\zeta$  distributions, defined:

$$\zeta = \frac{V_{2,IS}^2 - V_2^2}{V_{2,IS,MS}^2} = \frac{\left(\frac{P_{s,2}}{P_{t,2}}\right)^{\left(\frac{\gamma-1}{\gamma}\right)} - \left(\frac{P_{s,2}}{P_{t,1}}\right)^{\left(\frac{\gamma-1}{\gamma}\right)}}{1 - \left(\frac{P_{s,2}}{P_{t,1}}\right)_{MS}^{\left(\frac{\gamma-1}{\gamma}\right)}} \quad (2.13)$$

Here, the  $MS$  is the condition at the midspan, taken as a reference of two-dimensional flow. The  $\zeta$  coefficient is also used in Fig. 2.16, Fig. 2.17, Fig. 2.17, Fig. 2.18 and Fig. 2.19.

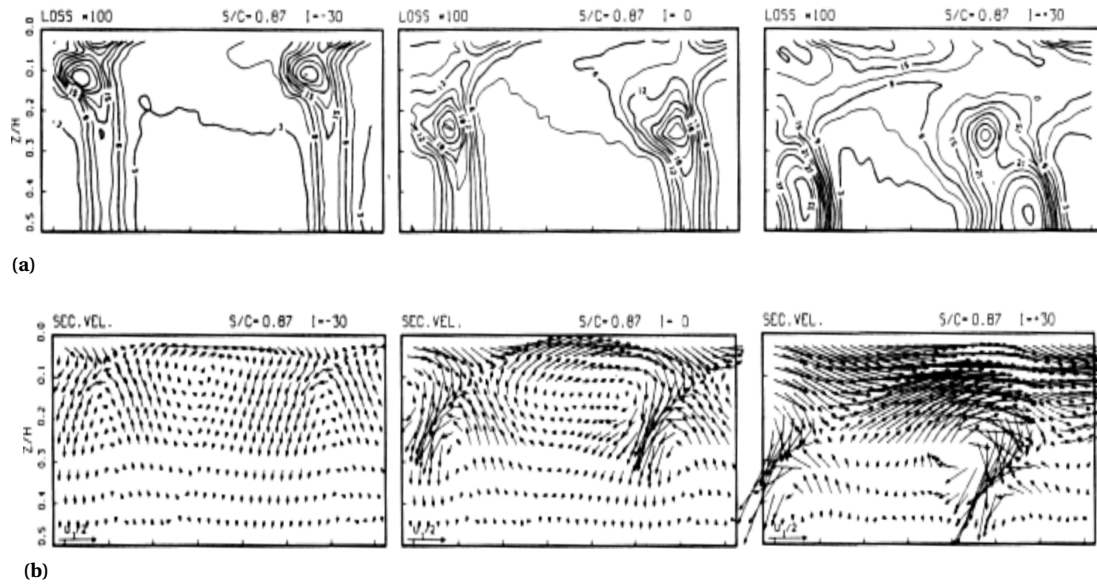


**Figure 2.16:** Comparison of measurements obtained with incidence angles  $-30^\circ$ ,  $0^\circ$  and  $+30^\circ$ ; distributions of: (a) kinetic energy losses, (b) secondary velocity. Perdichizzi et al. [32], 1996.

### MACH NUMBER

Another work of Perdichizzi et al. [34] assessed the impact of the expansion ratio on the evolution of secondary flow. The outcomes are shown in Fig. 2.17, where the distributions of losses and secondary velocity are reported for half-span of a passage (the  $y$  axis is the spanwise direction, the  $x$  axis is the pitchwise direction). For increasing outlet Mach number, from left to right, the passage vortex (circled in red) is progressively confined at the endwall; in particular, the passage vortex loss region loses relevance with respect to those of the corner (yellow) and the shed vortices (green), which conversely become more significant. The increasing relevance of the corner vortex is specifically due to the shockwave-boundary layer interaction, that enhances the loss peak in the area of the blade-endwall junction. More in general, the secondary flow has a reduced

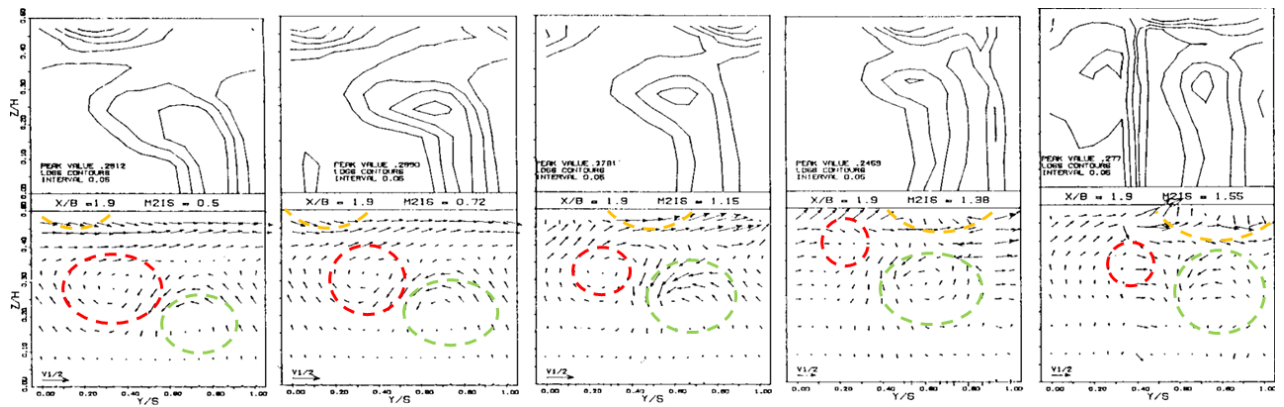


**Figure 2.17:** Comparison of loss distributions and secondary velocity fields for outlet flow Mach numbers 0.5, 0.72, 1.15, 1.38, 1.55, at a distance of 1.9 blade axial chords ( $C_{ax}$ ) away from the blade trailing edge. Passage vortex in red, shed vortex in green, corner vortex in yellow. Perdichizzi et al. [34], 1989.

effect at higher Mach numbers, as the experimental results in Fig. 2.18 can prove. In (a), spanwise ( $Z/H$ ) total pressure loss coefficient (Eq. 2.13) distributions for increasing Mach number are shown at a distance of 2.1 blade axial chords ( $X/B$ ); the smaller is the Mach number, the wider is the peak due to secondary losses close to the endwall. In (b) the outlet flow underturning ( $\Delta\beta$ ) shows decreasing values with growing outlet  $M$ . Indeed, at high Mach number, the swirling motion becomes negligible with respect to the main flow velocity, so the over/under-turning becomes of minor relevance. The loss coefficient in Eq. 2.13 accounts for the importance of the losses with respect to the kinetic energy after an isentropic expansion in the cascade; therefore

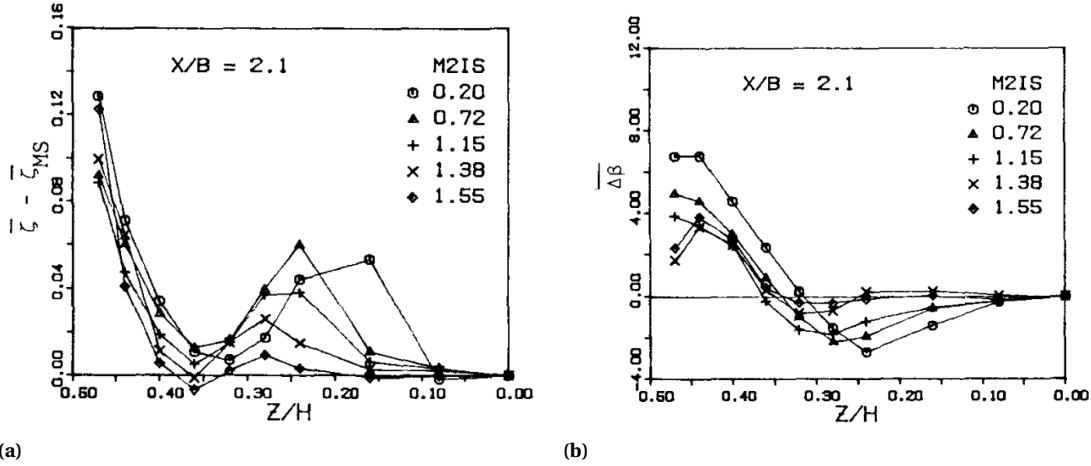


**Figure 2.18:** Spanwise distributions scaled with midspan conditions of: (a) kinetic energy losses, (b) outflow angle. Measurements taken at a distance of 2.1 blade axial chords ( $C_{ax}$ ) away from the blade trailing edge. Perdichizzi et al. [34], 1989.

Fig. 2.18 (a) only shows that the secondary flow is a major source of losses at low  $M$ . The net secondary losses, instead, follow the behavior in Fig. 2.19; they are rather constant in the incompressible regime (up to  $M = 0.5$ ), experience a step increase in the transonic range (to  $M = 0.9$ ), drop in high transonic/low supersonic, until  $M = 1.2$  is reached, and starts growing again later. To sum up, the increase of outlet Mach number do increases net the secondary losses but their relevance relatively to the total losses in the blade row is diminished.

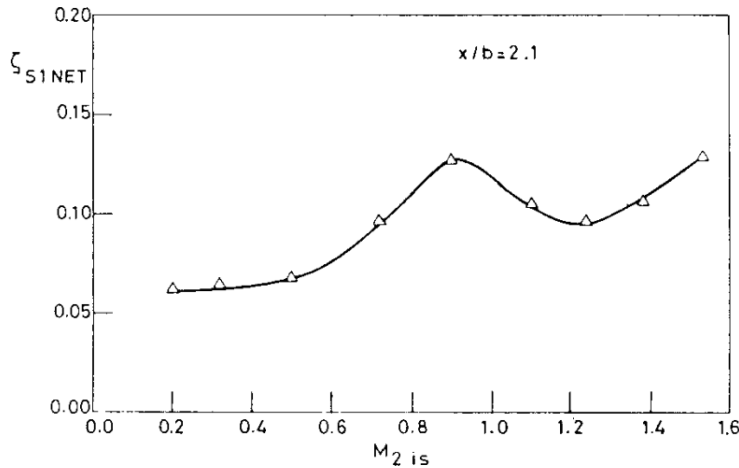


**Figure 2.19:** Trend of net secondary losses against the outlet Mach number. Perdichizzi et al. [34], 1989.

### REYNOLDS NUMBER AND BOUNDARY LAYER THICKNESS

Reynolds number ( $Re$ ) and boundary layer thickness ( $\delta_{inlet}$ ) effects have been studied by Hodson and Dominy in [36], using a low pressure rotor cascade as a test case. The investigation on Reynolds number effects (carried out in a cascade where the Reynolds number can be varied independently from the Mach number) has been carried out comparing experimental results obtained with  $Re = 1.5 \cdot 10^5$ ,  $2.9 \cdot 10^5$  and  $6 \cdot 10^5$ . The study revealed that the production of new secondary losses increases with higher Reynolds numbers. For lower Reynolds numbers the passage vortex interacts with a large boundary layer on the suction side; despite this causes a rather large area of losses, the general loss levels are low. Greater mixing losses are instead produced when a more powerful passage vortex is formed with a higher Reynolds number. Hodson and Dominy also compared the secondary flow characteristics with two different inlet boundary layer thickness,  $\delta_{inlet}^*/C = 0.11$  and  $0.22$ , where  $\delta_{inlet}^*$  is the displacement thickness and  $C$  is the blade chord. The authors conclude that this variation does not affect the amount of secondary losses produced throughout the turbine cascade, but that the outlet

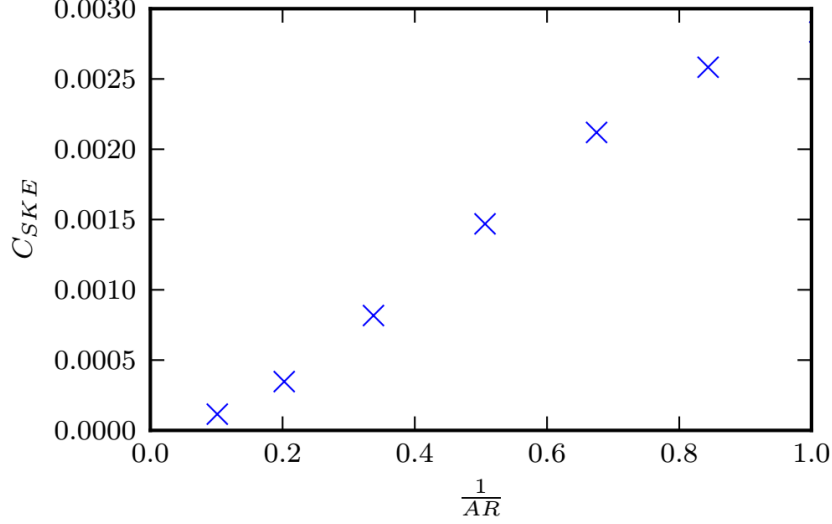


**Figure 2.20:** Results from inviscid calculations of exit  $C_{SKE}$  against the inverse of cascade aspect ratio. Clark et al. [4], 2016.

losses are higher for  $\delta_{inlet}^*/C = 0.22$  because of the larger boundary layer losses of the inlet flow.

#### ASPECT RATIO

Clark et al. reported in [4] the results of secondary kinetic energy coefficient  $C_{SKE}$  at the cascade exit for varying aspect ratios  $AR$ . The coefficient is defined as:

$$C_{SKE} = \frac{SKE}{KE_{bulk}} = \frac{\frac{1}{2}\rho\overline{V}_{sec}^2}{\frac{1}{2}\rho\overline{V}_{bulk}^2} \quad (2.14)$$

where the  $KE_{bulk}$  is the kinetic energy of the bulk flow. The authors carried out a parametric study by varying the aspect ratio of the cascade. The resulting trend is reported in Fig. 2.20, and shows that the relative importance of the  $C_{SKE}$  in Eq. 2.14 scales almost linearly with the inverse of the aspect ratio. It can be seen in Eq. 2.17, that the kinetic energy associated with the vortices is proportional to the square of the circulation, which is in turn proportional to the vorticity.

$$KE_{vortex} = \int_0^R \frac{1}{2}\rho V_{sec}^2 2\pi r dr = \frac{\Gamma^2 \rho}{4\pi} \left( \ln(R) + \frac{1}{4} \right) \quad (2.15)$$

Given a certain inlet vorticity and a certain flow deflection, according to the Squire and Winter model [8] (Eq. 2.9), the outlet streamwise vorticity is fixed, so the sum of the circulation is:

$$\sum_i^n \Gamma_i = const. \quad (2.16)$$

Where  $n$  is the number of vortices at the outlet. The total secondary kinetic energy downstream a blade cascade is, referring to Eq. 2.17:

$$SKE = \sum_i^n KE_{vortex,i} \propto \sum_i^n \Gamma_i^2 \quad (2.17)$$

For this reason, provided a given inlet vorticity and flow deflection, the  $SKE$  at the outlet is minimized for the maximum possible number of partitions  $n$  and, due to the non-linear relation, for evenly partitioned  $\Gamma$ . Varying  $AR$  for a fixed pitch-chord ratio is equivalent to change the blade count, varying the parameter  $n$ .

### 2.3. SECONDARY FLOW MITIGATION TECHNIQUES

In [22], Langston provided a list of possible techniques to mitigate the detriments of the secondary flow. The techniques can be divided in three categories:

1. splitting the secondary vorticity
2. modify the airfoil load distribution by leaning the blade
3. modify the endwall shape so to reduce the strength of the vortices
4. obstructing the vortex with a fence

The endwall fence, which combines the first and the third approaches, will be extensively explained in Sec. 2.3.5.

### 2.3.1. SPLITTER VANES

*Splitter vanes* are high aspect ratio blades placed in the middle of the flow passage, with the aim of reducing the outlet SKE by splitting the inlet circulation, as explained in the previous section (Sec. 2.2.5). Despite these have been already used by Spataro et al. in [38], where splitter blades are placed in the aft part of the passage to intercept the secondary flow developed upstream, the idea of the splitter blades to partition the boundary layer inlet vorticity come from Clark et al. [4]. Clark et al. performed a CFD-based optimization of the splitter blades and the “main” blades together, managing to achieve a mixed-out stage loss reduction of 15.3%.

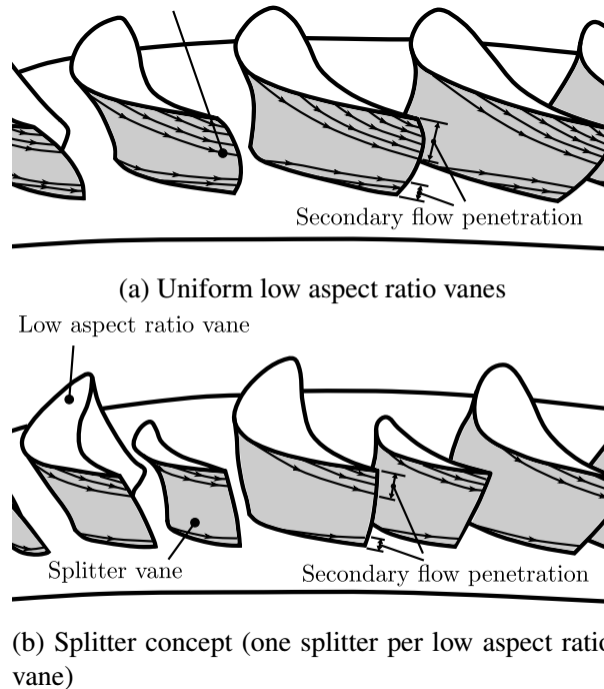


**Figure 2.21:** Comparison of secondary flow streamlines development on a normal low aspect ratio turbine cascade with the same cascade with the addition of splitter blades (and increased blade pitch). Clark et al. [4], 2016.

### 2.3.2. BLADE LEANING

The blade *leaning* consists in stacking the blade with an angle differing from  $90^\circ$  from the endwall. Besides the pressure gradient from the pressure to the suction surface, pressure gradients are also present along the blade surfaces; these are caused by the spanwise differences of static pressure, and it is directed toward the mid-span plane on the suction surface and toward the endwall on the pressure surface. These two contribute to feeding the passage vortex generating crossflow over the surfaces. Leaning the blade, however, the load over the surfaces is redistributed in such a way that a radial component of the force is created; this component is used to counteract the crossflow. An intuitive schematic of the effect of leaning is provided in Fig. 2.22: the figure represents a leaned passage with the superimposition of the normal passage vortex (in Fig. 2.22 (a)) with the vorticity introduced by the leaning. In particular, Fig. 2.22 (b) also shows the pressure contours on

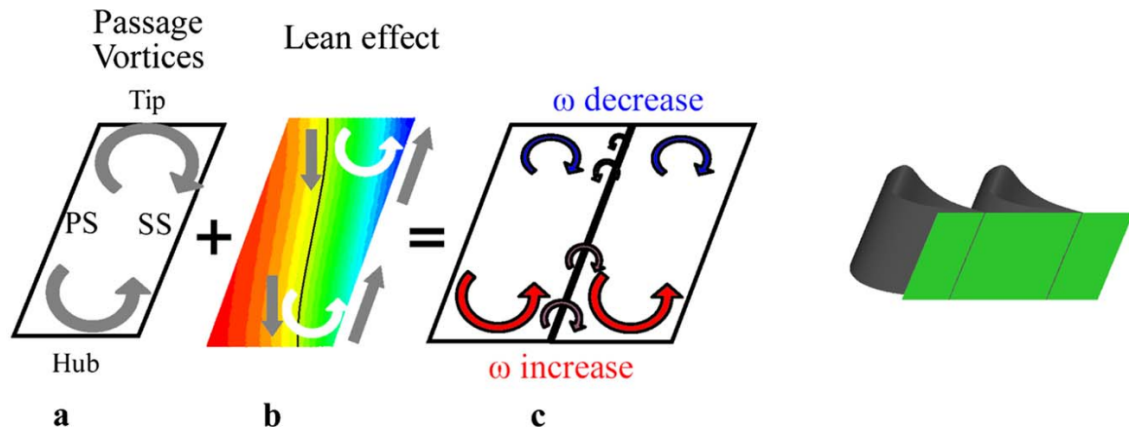


**Figure 2.22:** Schematic representing the effect of blade leaning on the secondary flow, as superimposition of common passage vorticity and vorticity introduced by leaning. D’Ippolito et al. [39], 2011.

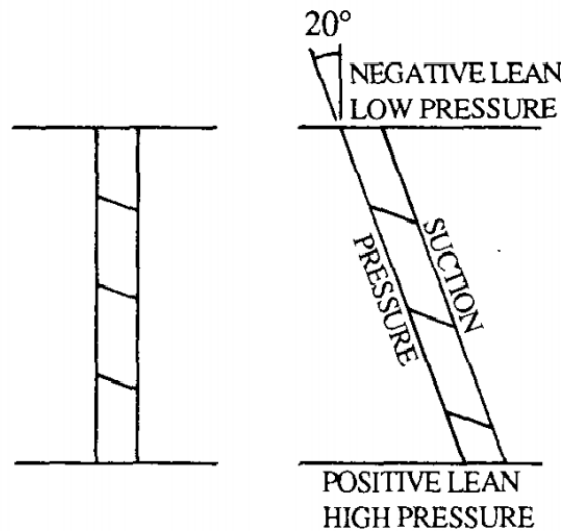


**Figure 2.23:** Sketch of front view of prismatic, lean and bow (i.e. compound) blades. Harrison [40], 1992.

the passage plane that causes the radial gradients. Fig. 2.22 (c) shows the resulting vorticity field, with the reduction obtained in the upper endwall and the increase in the lower. As employing blade leaning entails the growth of secondary flow close to one endwall, the In [40] Harrison studied this solution, comparing the results with those of a prismatic blade featuring the same airfoil; Fig. 2.23 shows the two cases, where the lean angle is 20° for the second case. Fig. 2.24 shows the results of this investigation as planar loss distributions. The passage vortex was actually weakened on the tip endwall, where the accelerated flow had a thinner boundary layer and the separated area was very small. The opposite happens at the hub endwall, where the boundary layer is thickened and the vortex is stronger. Nevertheless, the planar loss distribution displayed in Fig. 2.24 shows that 1.23 blade axial chords ( $C_{ax}$ ) downstream of the trailing edge, the upper passage vortex is carrying almost the same amount of losses as the lower, even if its peak value is reduced. The overall losses, anyway resulted to be higher in the lean case with respect to the prismatic one. D’Ippolito et al. [39], performed an optimization of the lean angle, and arrived at the conclusion that the improvements obtained, even with the optimal angle of 10°, with the lean blade are negligible.

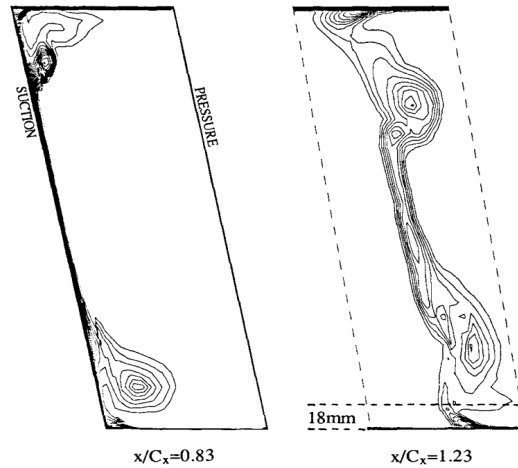


**Figure 2.24:** Comparison of planar loss distributions between planes located at 83% and at 123% of the  $C_{ax}$  from the leading edge.

### 2.3.3. ENDWALL CONTOURING

*Endwall contouring* consists in shaping the geometry of the endwalls so to modify the endwall pressure gradient that drives the crossflow from the pressure to the suction surface, and consequently mitigate the secondary flows development.

One of the first testing this concept was Deich et al. [42], who increased the efficiency of a turbine stator by profiling the endwall with an "S" shape similar to that shown in Fig. 2.25. Such a geometry accelerates the boundary layer on the contoured endwall, inhibiting the formation of a real passage vortex; the vortices are stretched because of the acceleration. Kopper et al. carried out wind tunnel experiments in [43], obtaining a reduction of 17% in massflow-averaged total pressure losses. Similar results were found also by Dossena, Perdichizzi and Savini in [44] through a campaign of combined CFD analyses and experiments.

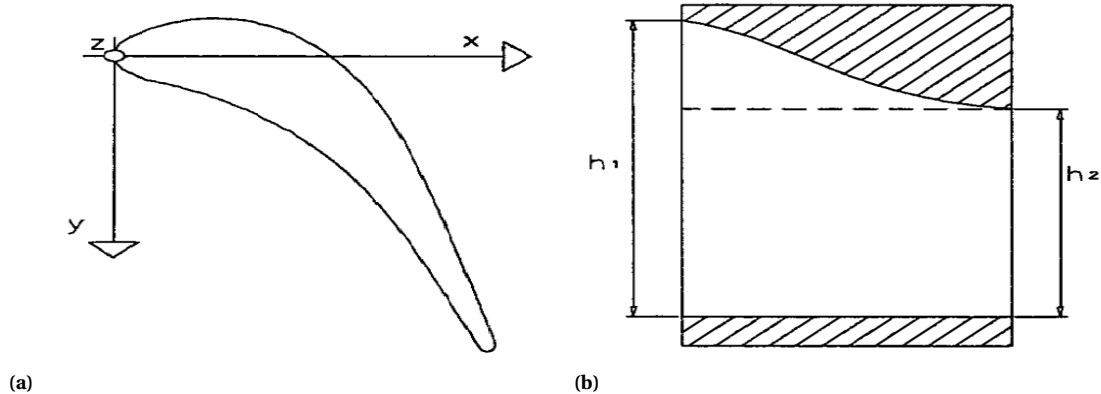


**Figure 2.25:** Drawing of an S-shaped endwall contouring. Dossena, Perdichizzi and Savini [44], 1998.

A different idea of endwall contouring is the leading edge fillet, consisting in profiling the endwall and the blade leading edge together, as in Fig. 2.26. With this technique, Zess and Thole [45] managed to eliminate the horseshoe vortex at the blade leading edge and to delay the formation of the passage vortex in a guide vane, with resulting decreased levels of streamwise vorticity and turbulent kinetic energy.

An extension of this concept has been developed by Sauer et al. in [46] and [47]. He thickened the blade leading edge at the junction with the endwall, creating a sort of bulb, as displayed in Fig. 2.27. The improvements found amounted to 47% reduction of secondary loss, obtained on a low pressure turbine cascade. The author hypothesized that the reason for this improvement is the increased strength of the counter vortex, which attenuates the development of the passage vortex.

More recently, a more complex endwall contouring shape has been created in [48] by Luo, Liu and McBean.

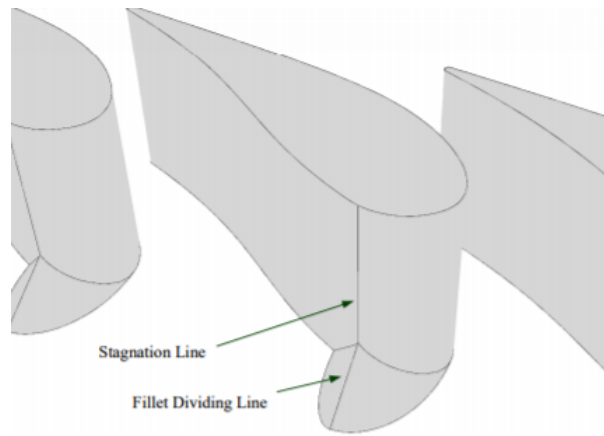


**Figure 2.26:** Schematic illustrating an example of leading edge fillet, Zess and Thole [45].

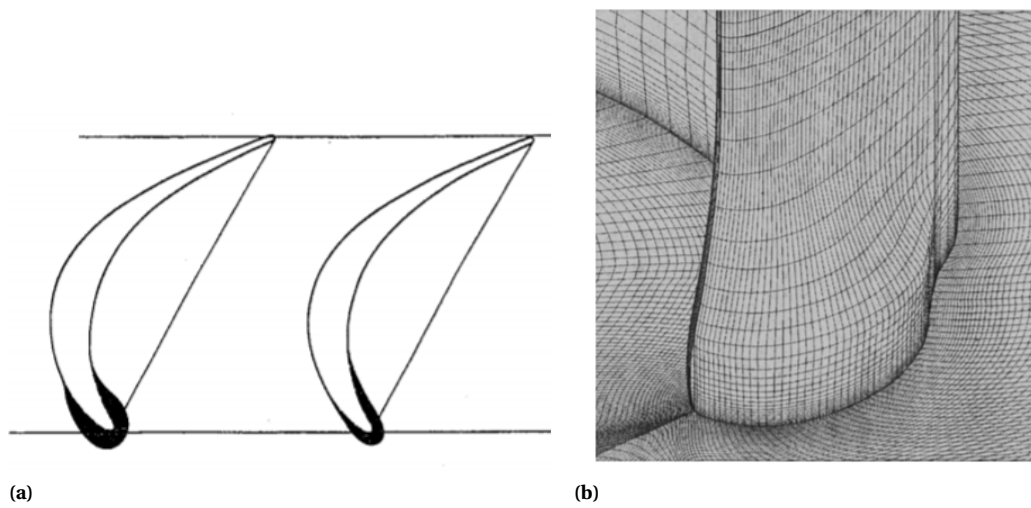


**Figure 2.27:** (a) Cross-sectional view of leading edge bulbs, (b) bulb surface mesh. Sauer et al. [46], 1999.

They added a field of height perturbation ( $dz$ ) to the endwall plane and they parameterized it with a summation of four harmonic functions, that has been optimized with the adjoint method. The perturbation field is shown in the color plot of Fig. 2.28. Increasing the endwall height close to the blade surfaces, they modified the pressure gradient in pitchwise direction and successfully reduced the crossflow, achieving a total pressure loss decrease of 4.9%. A similar approach has been also followed by [49].

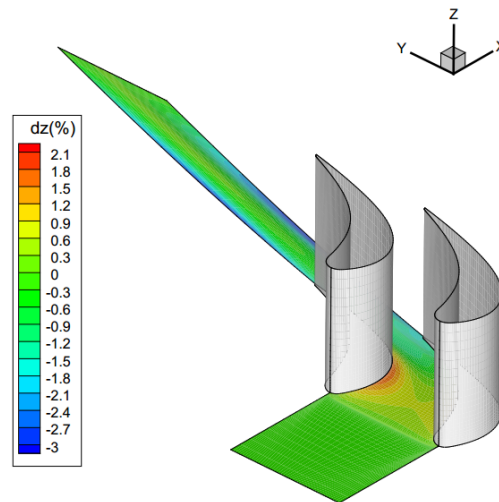


Figure 2.28: Color plot of the perturbation field used to obtain the contoured endwall profile in [48], Luo, Liu and McBean, 2011.

### 2.3.4. BLADE FENCE

A *blade fence* can be regarded as a barrier placed on the blade suction surface, close to the junction with the endwall. It prevents the passage vortex from climbing the blade surface and creating the separation region. It was originally conceived by Prümper [51] [52], and successively investigated by Kawai and Adachi in [53].

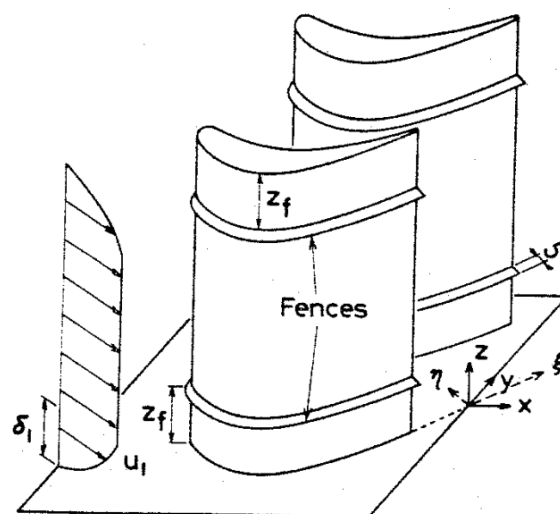


Figure 2.29: Schematics representing a cascade with blade boundary layer fences. Kawai and Adachi, [53], 1987.

### 2.3.5. THE ENDWALL FENCE

The *endwall fence* is another small barrier, similarly to the blade fence, that is placed on the endwall in the middle of the passage in order to block the crossflow and the migration of the passage vortex toward the blade suction surface. Mitigating the development of the passage vortex, endwall fences can reduce the secondary flow penetration, increase the pitchwise uniformity of vorticity, reduce the kinetic energy of the crossflow and decrease the mixing out of the vortices downstream the blade passage. Also this solution was proposed for the first time by Prümper [51] [52], whose original idea was to increase the resistance to the secondary flow by adding a fence along the passage middle line. Kawai et al. provided the first experimental results in [54], showing a loss reduction in total pressure of 25%. They performed an experimental optimization to assess the influence of fence height and pitchwise position on losses and secondary kinetic energy: the optimal configuration was found to be located in the middle of the passage channel, featured a height of  $1/3$  of  $\delta_{inlet}$  and the camber line was shaped as the blade camber. In addition, they noted that the passage vortex was actually divided in two smaller vortices by the fence, so that this device has a similar effect to the splitter blades in [4]. With this optimal fence configuration, Kawai et al. [55] also obtained a reduction of 60% on the blade loading defect that is due to the separation induced by secondary flow. In [56], he combined both endwall and blade fences, achieving an improvement of 26% in total pressure losses. A different concept of endwall fence has

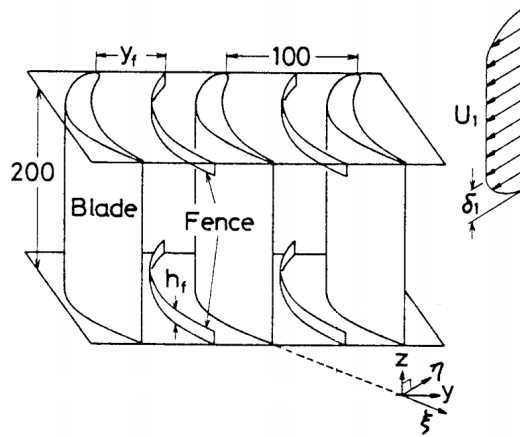


Figure 2.30: Cascade with endwall fences. Kawai et al., [54], 1989.

been tested by Chung and Simon in [57]. The fence that they designed is shown in Fig. 2.31: the difference with respect to the one used by Kawai et al. is that both leading edge and trailing edge are sharpened. Indeed, another horseshoe vortex is created in front of the fence, and a sharp leading edge diminishes its magnitude by reducing the deceleration flow region in front of the obstacle. The sharp trailing edge, instead, allows a smoother boundary layer release. Later, in [58], they used the same fence and cascade focusing on the aerodynamics performance at engine operative turbulence levels ( $\approx 10\%$ ) and observing a 17% reduction in total pressure losses. Aunapu et al. [59], shortened and changed the camber line of the same fence shape used by Chung and Simon, but, despite they successfully decreased the secondary kinetic energy of 30%, they increased the losses of 30% as well. Moon and Koh [60], studied the sensitivity of the fence height (normalized w.r.t. the boundary layer thickness) with the CFD, confirming the optimal height to be  $1/3$  of  $\delta_{inlet}$ , as found in [54], and pointing out the presence of a counter vortex (Fig. 2.32) forming on top of the fence as the reason for this result. Camci and Rizzo [61] studied the effects of an endwall fence in the simplified case of a  $90^\circ$  turning duct, in terms of both heat transfer and loss generation; they tested five concepts differing from each other for height (again normalized w.r.t.  $\delta_{inlet}$ ), length and thickness. Also here, the authors found that the configuration with optimal height ( $\delta_{inlet}/2$ ) was creating a counter vortex. However, it must be noted that, as explained in Sec. 2.2.3, the passage vortex is not only related to the  $\delta_{inlet}$  but also to the crossflow strength; this means that the normalization of the fence height with the  $\delta_{inlet}$  does not provide a universal reference dimension for the size of the vortex, but just for comparisons in the same cascade, having the blade loading. Kumar and Govardhan [62] carried out a CFD-based optimization of pitchwise position and height; besides the fact that they did not modify the camber line and that the length is the same as the whole flow passage, also in this case, the optimal solution is in the center. Nevertheless, their innovation, compared with the previ-

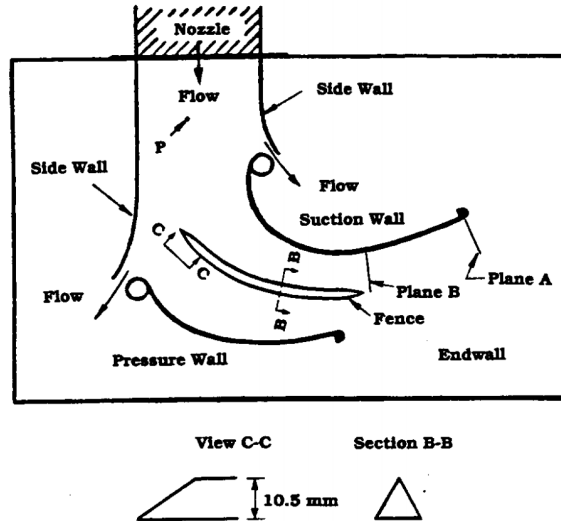


Figure 2.31: Endwall fence designed by Chung and Simon, [58], 1993.

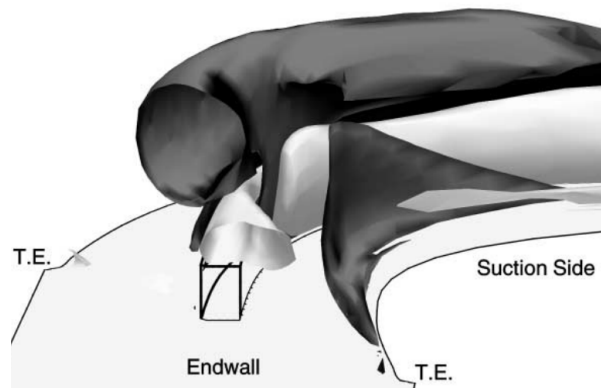
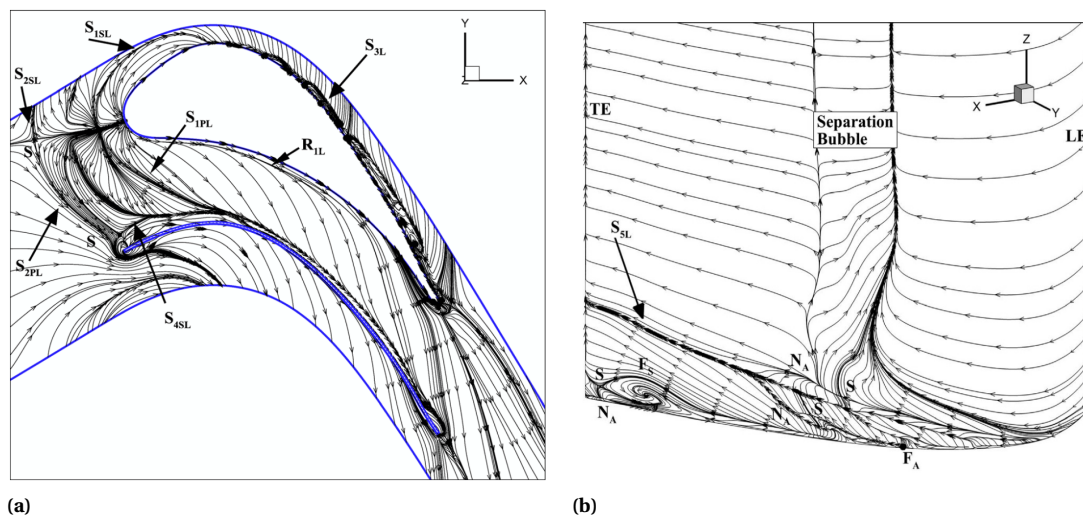


Figure 2.32: Vorticity iso-surface showing the formation of a counter vortex above an endwall fence of height equal to one-third of the boundary layer thickness, Moon and Koh [60], 2000.

ous optimizations, is their non-uniform height distribution, as they made the fence ramped from the leading edge to the trailing edge so to screen the increasingly bigger passage vortex. In [63] the same authors used the previously found optimized fence to study the topology of the limiting lines over endwall and blade suction surfaces, to understand the patterns of the separation lines in presence of a fence. As can be observed in Fig. 2.33, the separation line  $S_{2PL}$  is just diverted by the fence and climbs the suction side causing separation anyway, but the  $S_{1PL}$  is intercepted and released only at the fence trailing edge; this makes the vortex impinging on the blade wall to be much weaker.

The above mentioned studies proved the effectiveness of the endwall fence as a technique for the secondary loss mitigation. However, the authors designed the fences via experimental campaigns that allowed them to compare only a small number of configurations. Also, they could investigate the sensitivity of just a few geometrical parameters, namely pitchwise position, height, thickness and length. A larger design freedom, assessing the performance of more configurations and the influence of more geometrical features, would allow an increase in fence effectiveness. Moreover, due to the sensitivity of the secondary flow characteristics to the turbine configuration and flow conditions, the obtained optimal fences do not have general validity, and a design procedure is still not available.



**Figure 2.33:** Topology of skin-friction lines in a cascade with endwall fence: (a) on the endwall and (b) on the blade suction side. Kumar and Govardhan [63], 2014.

## 2.4. CFD MODELING OF SECONDARY FLOW

In order to accurately predict and compare the performance of each fence configuration with CFD simulations, the numerical model must be capable of capturing the flow characteristics within an acceptable error. In particular, in an optimization, a so-called *objective function* must be defined as simulation output parameter to quantify the configuration performance: for turbomachinery research, it is common and convenient the use of the total pressure loss coefficient. However, the prediction of total pressure losses is subject to uncertainty, as its value is largely affected by the choice of the turbulence closure (see the “closure problem”, Wilcox [75]). The turbulence models that require an acceptable computational power, and an optimization to be computationally affordable, are based on different simplifying assumptions; secondary flows, due to their highly three-dimensional nature, do not usually verify these assumptions.

One of these assumptions, used in the *Eddy Viscosity Models*, is the isotropy of turbulence. In fact, Eddy Viscosity Models are based on the so-called Boussinesq assumption:

$$-\overline{u'_i u'_j} = 2\nu_t S_{ij} - \frac{2}{3}k\delta_{ij} \quad (2.18)$$

meaning that the transport of momentum due to the turbulence is considered as a stress tensor  $-\overline{u'_i u'_j}$  (Reynolds stress) proportional to the mean flow velocity gradients ( $S_{ij}$ ) and to the turbulent kinetic energy  $k$ . Indeed, the eddy viscosity  $\nu_t$  is in turn proportional to  $k$ .  $k$  is a scalar property accounting for the distribution of turbulence in the flow field; however, the turbulence, consisting in small size eddies, is actually a three-dimensional property. Indeed, in [32] (1996) Perdichizzi et al. showed with experimental measurements that the hypothesis of isotropic eddy viscosity did not hold with such highly three-dimensional flow, hence that the use of an Eddy Viscosity Model would not be appropriate for secondary flows. Despite this, most of the CFD studies carried out successively on secondary flows, made use of Eddy Viscosity Models, probably because of the necessity of keeping low the computational cost.

Another assumption in the commonly used turbulence models is that the flow to be modeled is at high Reynolds number; given that the constants in the turbulence model are obtained experimentally or for asymptotical analysis (as explained by Wilcox in [75]), a simulation of a low Reynolds number flow, like the case investigated, will suffer an intrinsic error due to the model itself.

As a consequence, issues in validating the simulations are quite common in the literature. In the investigation carried out by Moon and Koh in [60] on the vorticity dynamics by means of CFD simulations, an agreement between CFD and experimental distributions of total pressure loss coefficient was just partially achieved. The validation results are shown in Fig. 2.34; neither the peak values, nor the position of the peaks was captured. A  $k-\epsilon$  turbulence model has been used with a wall function as wall treatment, which is actually not appropriate

Type/Location of losses	$C_L$ Experiments	$C_L$ CFD
Overall	0.1377	0.1926
Mid-Span	0.0598	0.1512
Secondary	0.078	0.0414

**Table 2.1:** Comparison of total pressure loss coefficient ( $C_L$ ) in CFD and experiments. Values of the overall losses, of the losses at the mid-span, and of the secondary losses. Hartland, Gregory-Smith and Rose [64], 2000.

for highly separated flows like the case in consideration (see Wilcox, [75]).

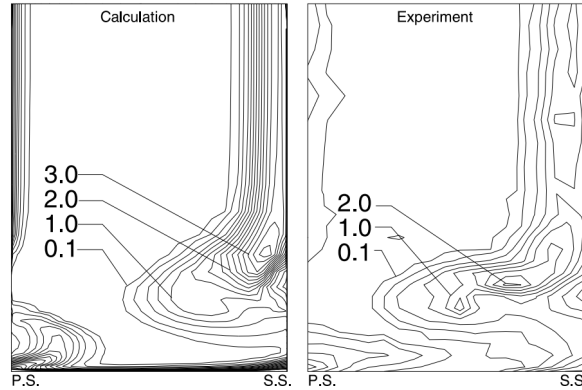


**Figure 2.34:** Comparison between total pressure loss coefficient from CFD results and experimental results. Moon and Koh, [60], 2001.

Langston [22], outlined the achievements and shortcomings of the works carried out until 2001 in CFD prediction capabilities, concluding that CFD was still not accurate enough to reliably capture the total pressure losses. Among the studies that he mentioned, the results of Hartland, Gregory-Smith and Rose [64] are exhaustive in showing the degree of disagreement between experiments and calculations; the values of total pressure loss coefficients are compared in Tab. 2.1.

More recently, Kumar and Govardhan (2011) sustained in [62] that the turbulence models available at that moment did not allow to make reliable predictions of total pressure losses so that these losses could not be employed as an objective function for an optimization. For this reason, they used a secondary kinetic energy coefficient; nevertheless, a lower secondary kinetic energy does not imply lower total pressure losses, and this method does not allow any evaluation of trade-offs with additional viscous losses when mitigation methodologies are being investigated.

In [50] Denton studied the limitations of turbomachinery CFD and concludes results must always be assessed experimentally. Still, he also states that it is useful on the comparative basis, to study the sensitivity of performance with respect to certain parameters. Indeed, in [4] Clark et al. performed a CFD-based optimization of splitter blades for secondary flow reduction with an Eddy Viscosity Model (Spalart-Allmaras model), and the same did Shahpar et al. [49]. Clark et al., in particular, used the CFD optimization to obtain the optimal design, and assessed the improvement by means of wind tunnel experiments. Therefore, the CFD limitations in correctly predicting the total pressure losses only affect the capability of the designer in making absolute evaluations on the performance; nevertheless, CFD remains a suitable tool for design processes like a shape optimization, where the sensitivity of performance to some geometrical parameters is assessed. As in [4], wind tunnel experiments are needed for a final evaluation of the improvement.

## 2.5. SURROGATE MODEL OPTIMIZATION FOR CFD-BASED AUTOMATED DESIGN

In a CFD-based shape optimization, an optimization algorithm elaborates the CFD results correlating them to the values of geometrical parameters, to find the combination of parameters providing the best results. Op-

timization algorithms can be roughly classified in gradient-free and gradient-based methods. For turbomachinery applications, gradient-free methods offer ease of implementation and flexibility to use different CFD models and solvers. Among these, *surrogate model* methods [66] are attractive as they provide an overview of the *design space* (or *parameters domain*) that can be also exploited to gain a physical understanding of the problem investigated. The surrogate model optimization, or *response surface optimization*, consists in creating a mathematical model (indeed, the response surface) correlating the parameters of the optimization to the objective function by fitting or interpolating some experimental, or numerical, data. Then, once a reliable surface is obtained, the optimization can be accomplished directly on it with a simple gradient-based algorithm. There are different ways to carry out a response surface optimization, differing from each other for the algorithms chosen for the three phases of the process:

1. Design of Experiments (DOE)
2. Response Surface Algorithm
3. Optimization

As Ansys Workbench 17.1 has been chosen as a framework for the tool development, the theoretical background acquired has been circumscribed to the algorithms implemented in it [67].

### 2.5.1. DESIGN OF EXPERIMENTS

The DOE consists in generating a set of samples of different cascade configurations whose performance are then evaluated by means of CFD. The CFD predictions can be then used to build a response surface, namely a surrogate function that mimic the behavior of the real, unknown, cost function. Each configuration is defined by a combination of the optimization parameters. A *Full Factorial Design* ([68]) should be employed to have a total description of the effect of each parameter and their combination; however, the number of simulations that must be run in this case drastically rises, going out of the feasible range, for an optimization in thirteen variables as the present case. This kind of DOE requires that all possible variable combinations are tested at every *level*. Is called level a value in which a variable is tested: so for instance if the variable  $x$  is tested for  $x = \{-1, 0, 1\}$ , there are three levels. As a consequence, for thirteen variables, in three levels (which are however quite a few), the total number of simulations would be  $3^{13} = 1594323$ . For this reason, *Fractional Factorial Designs* must be employed, which drastically reduce the number of simulations but do not allow evaluations of the combined effects. The alternatives given in Ansys are:

**Central Composite Design** It is a DOE in 5 levels (-2, -1, 0, +1, +2) in which points are disposed as in Fig. 2.35: there is one point in the center in which all parameters are at the central level (0), the “axial points” in which all parameters are at the central level while one is at  $\pm 2$ , and the “corner points” where all parameters are at  $\pm 1$ .

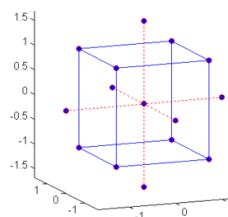


Figure 2.35: CCD disposition of points [67].

**Box-Behnken Design** It is a 3 levels DOE where the corners are not considered and the influence of parameters interaction is evaluated where one of them is kept at the central level, as in Fig. 2.36.

**Latin Hypercube Sampling** This is a quasi-random DOE in as many levels as is the number of parameters; thus, every parameter is tested at one level only once. Also, at every point the levels of the parameters will be always different: there might be a point in (0,2,-1), but never in (2,0,2), for example. The advantage of this sampling technique is exactly the large number of levels in which every parameter is tested.

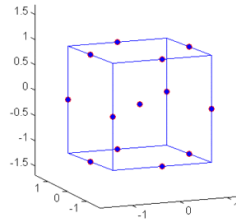


Figure 2.36: Disposition of points in a Box-Behnken Design [67].

**Optimal Space Filling** This is an improved version of the LHS (Latin Hypercube Sampling) in which the distance of the generated points in the parameter domain is optimized, as demonstrated in Fig. 2.37

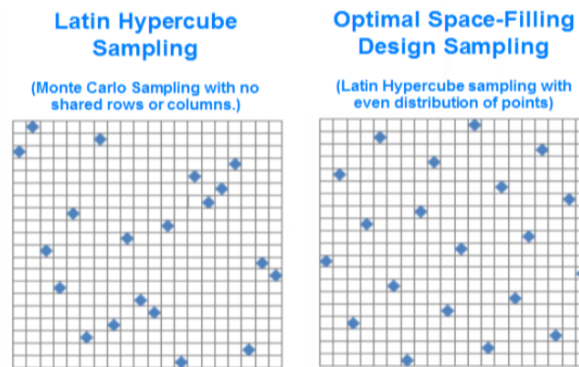


Figure 2.37: Comparison of the disposition of points with an LHS and with an OSF [67].

In general, a rule of thumb for the choice of a DOE could be that when no previous information is available on the parameters domain, LHS or OSF should be chosen because of the number of random combinations of levels tested. In the opposite case, when the best configuration has been already identified, the CCD or the Box-Behnken Design are more appropriate to investigate the local sensitivity of each variable and to optimize in the point neighborhood (neighborhood intended in its mathematical meaning).

### 2.5.2. RESPONSE SURFACE TYPES

From the same data set, different response surfaces can be created according to the requirements of the problem. The following are available in Ansys Workbench:

**Full 2nd-Order Polynomial** This method creates a surface in the form of a full second order polynomial, i.e. in the form:

$$f(x) = \sum_i^N a_i x_i^2 + \sum_j \sum_i^N b_{i,j} x_i x_j + c$$

where  $N$  is the number of variables. It is based on a regression analysis, so on a minimization of the error between data and model by minimizing the coefficients  $a_i$ ,  $b_{i,j}$  and  $c$ . It is a simple alternative, but has the intrinsic limitation due to its quadratic nature, of being unable to describe complex problems with different critical points and changes in curvature.

**Kriging** This model, on the contrary of the previous, is suitable for describing complex behaviours due to the high order of its output response surface. The output function accurately interpolates the data and is made up by: 1) a second order polynomial giving the overall trend of the surface, 2) a series of Gaussian functions creating local deviations from the trend to capture every point. Basically, it can be described as:

$$f(x) = g(x) + Z(x) \quad \text{where} \quad Z(x) = \sum_i^n \lambda_i r(x^i, x)$$

Here,  $g(x)$  is the polynomial and the  $r(x^i, x)$  are the gaussian functions centered in  $x^i$  and of magnitude  $\lambda_i$ .

**Non-Parametric Regression** Suggested for highly nonlinear behaviours of the objective function with respect to the parameters, and for problems where there is large influence of the mixed terms. This response surface is created through a regression analysis method in which no prior functional form is assumed for the response surface. The form is instead provided by the data themselves, building a model as:

$$Y = \sum_i^n (A_i - A_i^*) K(\mathbf{X}_i, \mathbf{X}) + b$$

where  $K(\mathbf{X}_i, \mathbf{X})$  is the kernel map and  $A_i^*$  and  $A_i$  are Lagrange multipliers. Further explanations can be found in [67].

**Neural Network** This last methodology is based on the learning process of a human brain to link inputs and outputs. The scheme in Fig. 2.38 represents the connections of inputs and outputs with the hidden functions, namely the response surface. Associating every connection to a weight  $w$ , for each neuron  $k$  the relation with the inputs  $x_i$  is:

$$f_k(x_i) = \sum_j^n w_{j,k} x_i + b_k$$

where  $b_k$  is the bias of the neuron. The algorithm "learns" by changing the values of the  $w_{j,k}$  and evaluating the error between the response surface and the measured data. A detailed explanation can be found in [69].

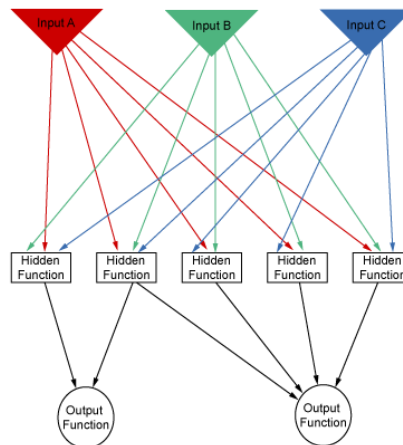


**Figure 2.38:** Scheme of Neural Network algorithm [67].

In order to evaluate the degree of accuracy of the created response surface, a parameter called Goodness of Fit (GoF) can be calculated with Ansys Workbench; this check is a valuable indicator for the choice of the most accurate fitting method, except for the Krigin with which, being interpolation, the GoF is identically 1 (maximum value). Otherwise, the choice should be made according to the occurrence of divergence or the actual prediction capabilities, tested by verification.

### 2.5.3. OPTIMIZATION

The optimization phase, at the end, is carried out by looking for the minimum (or maximum, accordingly) directly on the response surface. For this purpose, different algorithms are available:

**Screening** This makes use of an algorithm called Shifted Hammersley Sampling [70] that creates a set of sample points calculated on the response surface and the minimum is returned as an optimal value. This does not guarantee to pick up the best configuration, but provides an overview of the response surface in the case that there are different regions of local optima.

**NLPQL** Nonlinear Programming by Quadratic Lagrangian, presented in [71], is a gradient-based methodology, namely an algorithm in which the solver calculates the gradient on the function and proceeds following it until a minimum is reached. In particular, being also suitable for constrained problems, it works linearizing the constraints and constructing a quadratic approximation of the Lagrangian function. The optimization in this case is done on the Lagrangian instead of the original response surface, so to take into account the constraints. However, being a gradient-based method, the result is sensitive to the starting point of the gradient calculation, as it could find a local minimum.

**MOGA** Multi-Objective Genetic Algorithm, is appropriate for multi-objective optimizations. It works creating a population of points similarly to what is done by using the Screening.

Even if gradient-based methods are sensitive to the starting position of the iterative optimum research, the optimum can be here located with arbitrary accuracy; conversely, algorithms based on random sampling provide a complete overview of the potentially different optimal regions, while the accuracy of the research is actually dependent on the case (and on the number of sampling w.r.t. the domain dimension).

# 3

## TECHNICAL APPROACH

This chapter provides a detailed description of the proposed methodology, and of the computational framework: Sec. 3.2 describes the parameterization of the fence, Sec. 3.3 illustrates the main aspects of the mesh development and its features, Sec. 3.4 discusses the CFD model used for the case investigated and Sec. 3.5 explains the optimization.

### 3.1. AUTOMATED DESIGN CHAIN

The methodology implemented for the endwall fence design, as anticipated, is a Response Surface Optimization based on CFD simulations. The block diagram in Fig. 3.1 illustrates the optimization process and the different steps involved:

1. Design of Experiment: as explained in Sec. 2.5.1, it is a set of geometrical configurations (i.e. design points or DP) that are tested by means of CFD simulations.
  - (a) Parameters Manager: manages input and output parameters of each design point.
  - (b) Geometry Modeler: takes as input the set of parameters corresponding to each configuration and generates the fence geometry.
  - (c) Mesh Adapter: receives the geometry and adapts the mesh.
  - (d) CFD Simulator: performs the simulations and outputs the objective function value related to a certain configuration.
2. Response Surface Generator: receives the complete DOE and uses the data to create the response surface with the algorithms of Sec. 2.5.2.
3. Optimizer: finds the optimum in the response surface as in Sec. 2.5.3.

The algorithms adopted for the three phases of the response surface optimization are:

- DOE: Optimal Space Filling.
- Response Surface: Non-Parametric Regression.
- Optimization: NLPQL.

Justifications of these choices are provided in Sec. 3.5.

The optimization starts with the definition of the DOE. When the DOE is complete, the response surface is generated and the optimization is performed. Once an optimum is identified in the response surface, it must be verified with a CFD simulation: if the value of the objective function has been correctly predicted by the surrogate model, the design is complete. If the prediction is not accurate enough, for errors greater than 1%, surface refinement is required and a new optimization is carried out. This process can be repeated different times, until convergence between response surface prediction and CFD simulation results is reached.

Further insight into the main blocks taking part in the process is provided in the next sections.

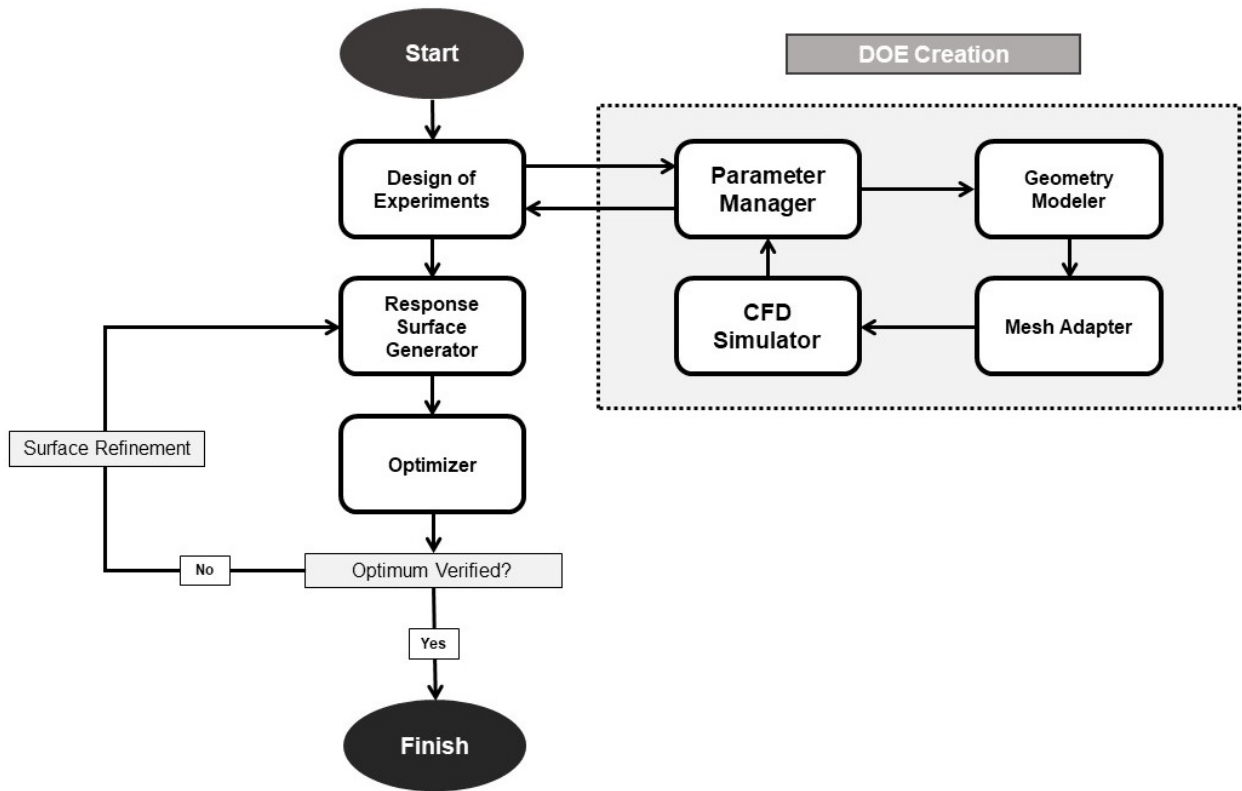


Figure 3.1: Block diagram representing the automated design loop.

### 3.2. FENCE PARAMETERIZATION

The shape optimization requires a parameterization of the fence. This means that its geometrical features have to be related to geometrical parameters so that, when the parameter value is modified, the shape changes accordingly. Solidworks has been used to obtain the flexibility required for the parameterization, as it can be coupled with Ansys Workbench to exchange information in background. The fence geometry is parameterized with the 13 parameters shown in Fig. 3.2, that are:

- Pitchwise and streamwise position of the leading edge ( $x_1$  and  $x_2$ )
- Camber line shape ( $x_3$ ,  $x_4$  and  $x_5$ )
- Axial length ( $x_6$ )
- Thickness distribution ( $x_7$ ,  $x_8$  and  $x_9$ )
- Height distribution ( $x_{10}$ ,  $x_{11}$ ,  $x_{12}$  and  $x_{13}$ )

The fence pitchwise ( $x_1$ ) and streamwise ( $x_2$ ) positions refer to the coordinates of the control point at the leading edge, as displayed in Fig. 3.2 (a). The camber line, Fig. 3.2 (b), is modelled as a quadratic Bézier curve, and the parameters are the positions of its control points with respect to the fence leading edge. As these control points are positioned relatively to the fence leading edge, instead of the blade, the camber line shape is decoupled from its position.  $x_3$  and  $x_5$  control the camber by moving the control point mid-camber line control point along the two planar directions, while  $x_4$  controls the trailing edge pitchwise position. The parameter controlling the axial length ( $x_6$ ) moves the mid-camber line and the trailing edge control points in such a way to maintain the blade metal angle distribution by changing  $x_3$ ,  $x_4$  and  $x_5$  proportionally. The thickness distribution is controlled by the thickness in three points: leading edge ( $x_7$ ), trailing edge ( $x_9$ ) and half camber line ( $x_8$ ), as in Fig. 3.2 (c). The fence height is parameterized by using a spline passing through

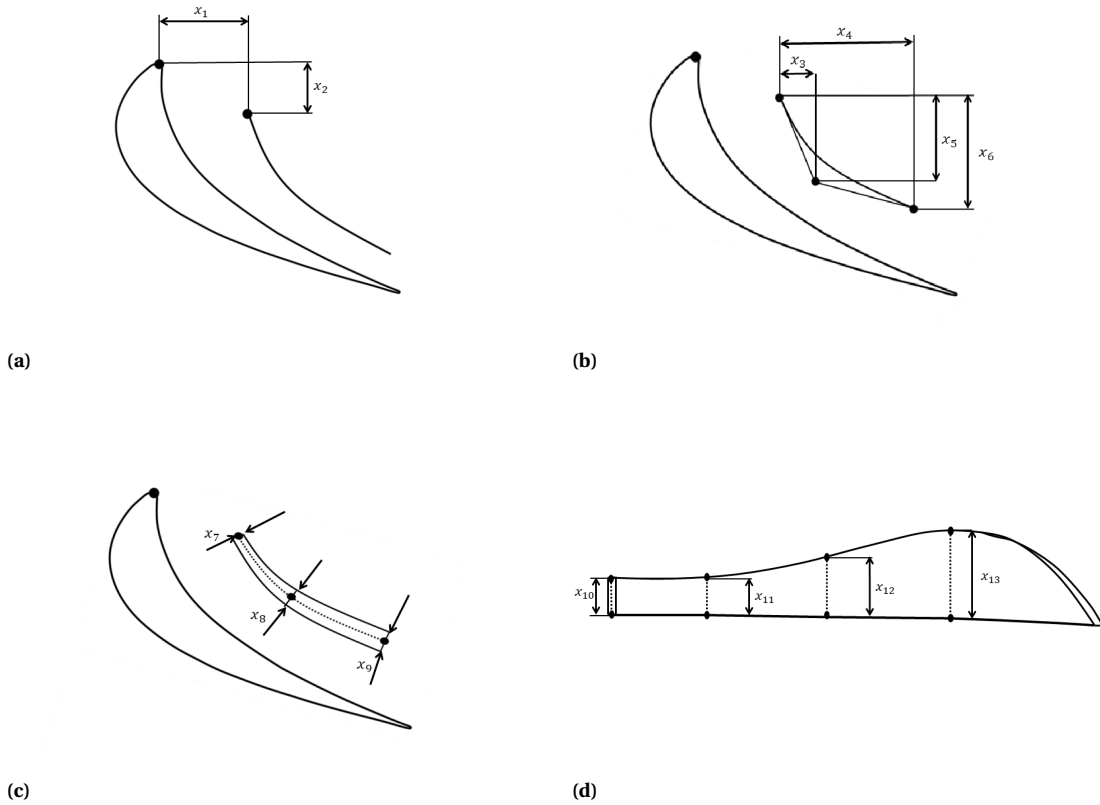


**Figure 3.2:** Sketches showing the parameterizations of: (a) position (b) camber line and length (c) thickness distribution (d) height distribution.

4 control points positioned at 25%, 50%, 75% and 100% (TE) of the Bézier curve (Fig. 3.2 (d)). The degree of freedom of these points is only along the endwall-normal direction.

The passage geometry and the endwall fence are created in two separated files, respectively in Fig. 3.3 (a) and (b). The former is just partially parameterized, as only blade pitch and span can be set; however, for future applications, the blade shape has to be made totally modifiable, in order to adapt the optimization framework for any kind of cascade. Both Solidworks files were imported in the Geometry Editor of Ansys Workbench, where the solid of the fence is subtracted from the solid of the flow passage, creating the “fenced” cascade passage.

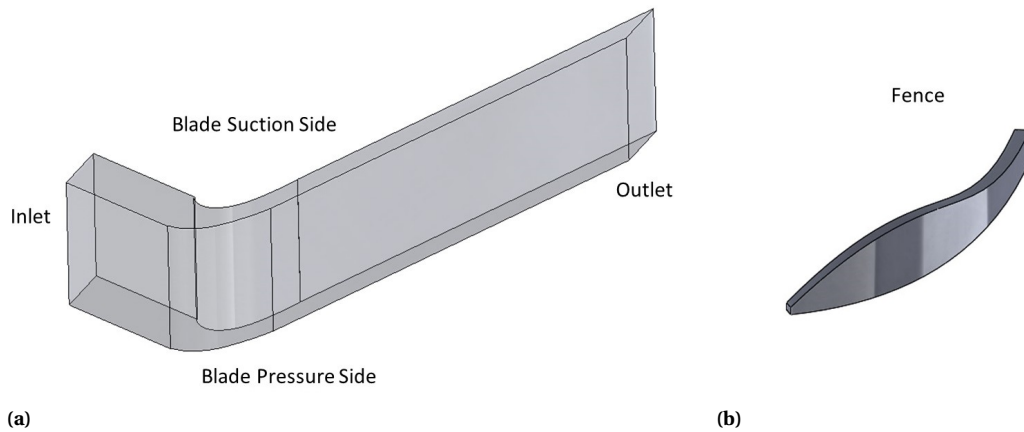


**Figure 3.3:** CAD models of: (a) the flow passage domain and (b) an example of endwall fence.

The information regarding each new design point to be simulated, as already mentioned, is provided by the DOE through the Parameters Manager; the Geometry Editor updates the fence shape by sending the data to SolidWorks, which is run in background and returns the updated fence shape. This is again subtracted from the flow passage domain and exported to the Meshing tool, ICEM.

### 3.3. MESHING PROCESS

Obtaining a robust meshing process, capable to adapt to all the different geometries that can be generated during the optimization is a very complicated task. Indeed, as also pointed out in [49], “the development of an integrated parametric mesh generator [...] represents today one of the most challenging issues for turbomachinery designers”. A structured mesh has been used for its numerical accuracy, attractive characteristic with highly three-dimensional flows like the present case, and the lower computational costs, crucial aspect for an optimization problem where many simulations need to be run. However, providing to a structured mesh the flexibility required to adapt to the geometry modifications, is particularly problematic.

#### 3.3.1. MESH ADAPTION THROUGH GEOMETRICAL ELEMENTS ASSOCIATION

The mesh is initially built in ICEM and then automatically deformed for each CFD evaluation of the optimization process according to the fence geometry under scrutiny. More precisely, in ICEM, the mesh is built with the aid of a simple GUI that initially shows it as a parallelepiped block. The user can split the block into different sub-blocks and organize them according to the meshing strategy; in this work, the mesh has been created with an H-grid structure. Then, the corner and edges of every sub-block can be associated with points and curves of the geometry; after this operation, in the present case, blocks look like shown in Fig. 3.4. By doing so, the curves of the geometry remain associated with the blocks edge, and for every shape modification of the fence, the mesh will be reconstructed accordingly. Fig. 3.5 shows an example of the morphed mesh for a large geometrical deformation of the original fence shape. This proves that the mesh adaptation algorithm is sufficiently robust for the problem at hand.

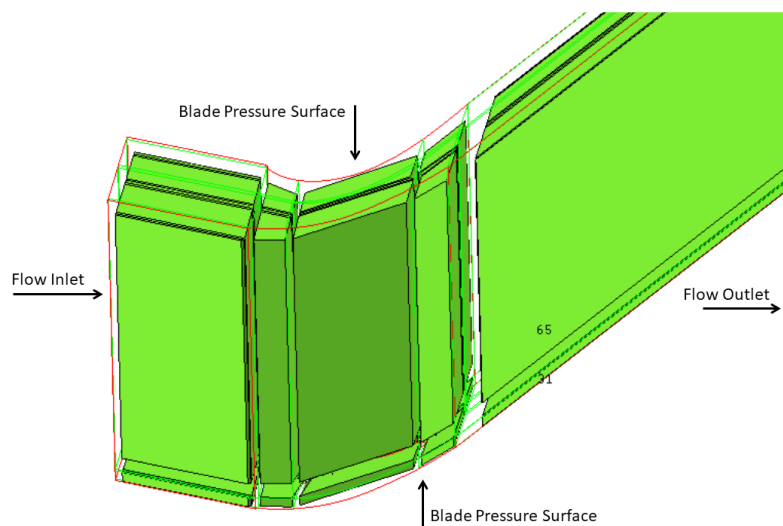


**Figure 3.4:** Mesh blocks adapted to the shape of the flow domain.

The local refinement of the mesh is determined by the number and distribution (linear, polynomial, exponential, etc...) of nodes that are set on the edges of each sub-block. Fixing a number of nodes along the edges of a changing geometry entails a variation of mesh resolution that, if locally decreased beyond a certain level, might affect the accuracy of the calculation results. For this reason, the nodes number of each edge has been parameterized: basically, when the movement of the fence reduces or enlarges an edge, the number of nodes in this edge is, respectively, decreased or increased. This way, the mesh density has been kept fairly constant in every region of the flow passage, for the whole range of parameters variability.

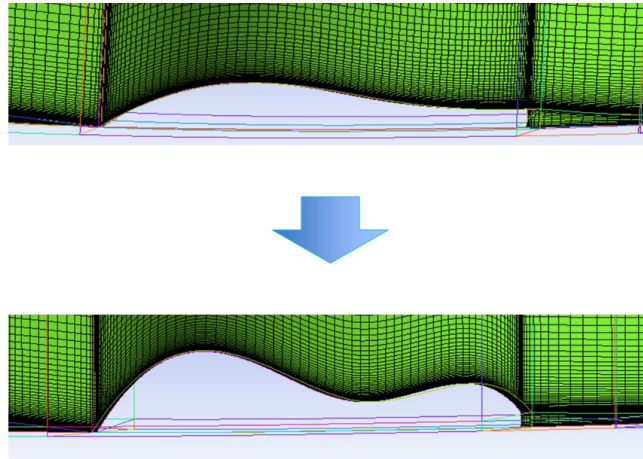


**Figure 3.5:** Example of automatic mesh adaptation to the fence geometry modification.

### 3.4. CFD MODEL

The CFD simulations are run in Ansys CFX 17.1 [67]. The numerical model used consists in the incompressible steady state RANS and the turbulence closure is achieved with the two equation  $k - \omega$  Shear Stress Transport model (SST [72]). The velocity profile boundary condition is required for the inlet, possibly obtained by means of experiments. In this way, the inlet vorticity, which is the origin of the secondary flow, can be correctly modelled. A static pressure is, instead, needed at the outlet. Periodicity has been imposed on the sides, and, in order to simulate only half of the blade span, symmetry has been set at the mid-span plane. A high resolution numerical scheme of the UDS-type has been used, blending between first and second order as a compromise between stability and numerical viscosity: a first order scheme is used where the variables change sharply, while second order is used where gradients are lower. The calculation of the time scale is performed automatically by Ansys CFX on the base of the boundary conditions, flow conditions, physics, and domain geometry. Details on the calculation method can be found in the Ansys Guide [67]. A simulation is considered converged when the RMS values of the residuals reach  $10^{-6}$ . Otherwise, the calculation stops after 130 iterations, as it has been observed that the convergence is usually achieved within 100 steps.

Each simulation outputs both the values of the objective function and the RMS residual of the pressure. This way, it can be recognized whether the simulation converged or not, so that, in the case, the design point can be discarded.

### 3.5. OPTIMIZATION THROUGH RESPONSE SURFACE

An Optimal Space Filling-type DOE has been used, but according to the prior knowledge on the geometry the DOE can be chosen differently; for example, if an experimental optimization already provided a well-performing configuration, a CCD DOE could be preferred to explore the performance variation around that design point.

Once the DOE is complete, i.e. all simulations have been run, the response surface is generated with one of the available algorithms. The algorithm chosen for this optimization framework is the Non-Parametric Regression, which is particularly appropriate for highly non-linear problems. Fig. 3.6 shows an example of response surface correlating a total pressure loss coefficient (presented in Sec. 4.1.1) with the position parameters of the control point of the camber line,  $x_3$  and  $x_5$ . The available visualization tool can be exploited to gain an understanding of the objective function sensitivity with respect to the parameters.

The optimization is carried out on the derived surrogate model with a combination of gradient-based and gradient-free methodologies. A gradient-based methodology provides the highest accuracy in finding the optimum, but are intrinsically incapable to distinguish global from local optima. For this reason, a preliminary

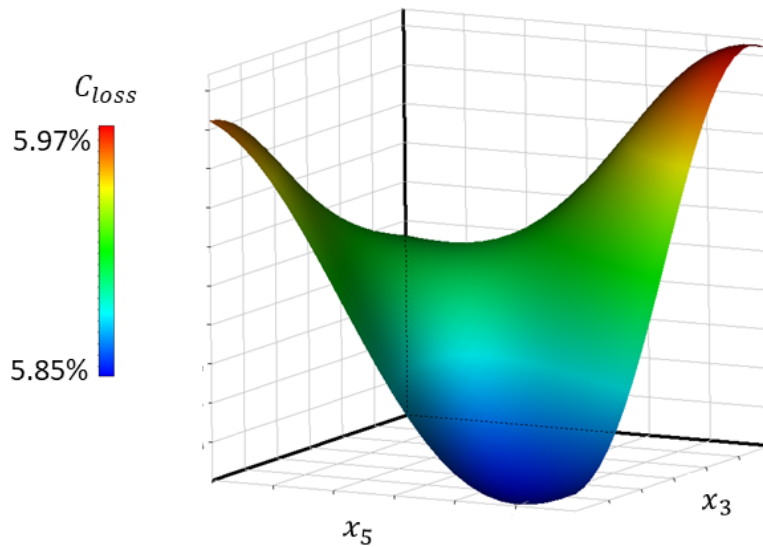


**Figure 3.6:** Example of response surface for total pressure loss coefficient as a function of the position of the camber line control point.

overview of the response surface is first acquired with the Screening (Sec. 2.5.2) method, allowing to start the optimization iterations from a point located close to the global optimum. Then, the global optimum is identified with the NLPQL method.

The optimum identified must be verified with a CFD simulation, as, according to the size of the DOE and the complexity of the problem, the surrogate model might have wrongly captured the trend. If the predicted value of the objective function differs from the value calculated beyond a certain tolerance (for instance  $\approx 0.5\%$  of relative error), the surface needs to be refined. In this case, the non-verified optimum point can be used as a refinement point and be added to the DOE; re-calculating the response surface and re-performing the optimization, another predicted optimum will be obtained. This process is repeated for few iterations, until the predicted objective function matches the simulation results within 1% of the simulation value. Once convergence is reached, the optimization is concluded.

# 4

## CASE STUDY

This chapter reports the results obtained with the application of the methodology illustrated in the previous section. Sec. 4.1 presents the turbine cascade where the fence has been applied, together with the starting shape of the fence. Sec. 4.3 presents the geometrical features of the optimal fence configuration obtained, Sec. 4.2 discusses the trend of the response surface created, and Sec. 4.4 reports a comparative analysis of the fluid-dynamic performance of the optimal configuration w.r.t. the baseline cascade.

### 4.1. TEST CASE PRESENTATION

In order to prove the effectiveness of the methodology, the endwall fence optimization has been performed on a prismatic linear stator of a steam turbine. This cascade is representative of a low-pressure steam turbine cascade for power generation applications. In the literature, there is only one other study about secondary flows in steam turbines (Li et al. [76]), and this work is the only shape optimization methodology ever performed on it. However, since the Reynolds number is lower than in gas turbines, the secondary flow is not a main source of losses as in high pressure gas turbine vanes.

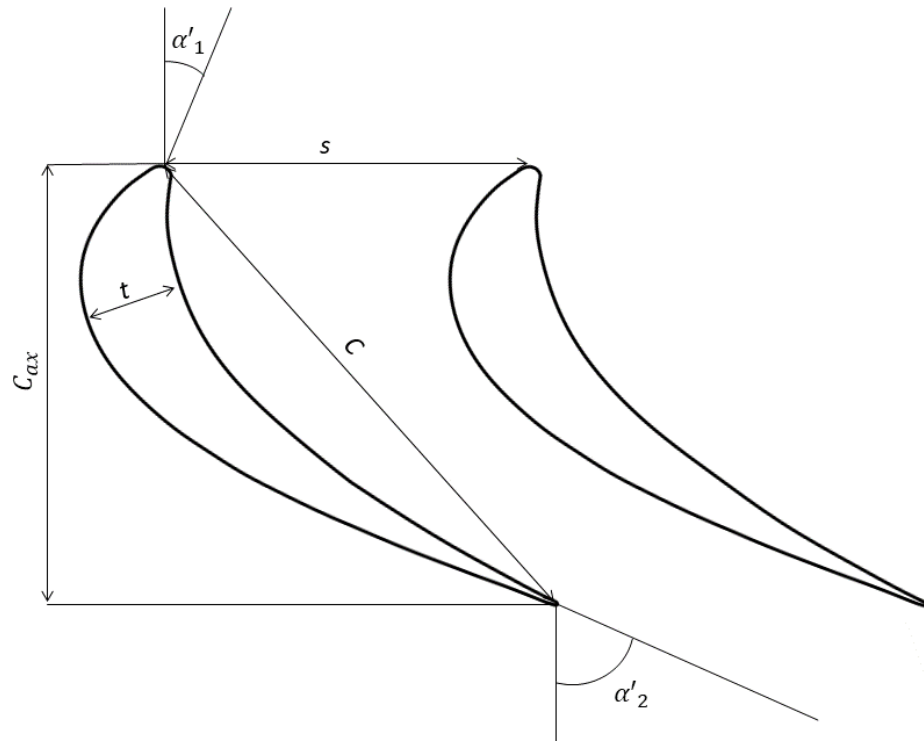
This cascade is available at the low-speed single stage test facility of the Osaka Institute of Technology (OIT) laboratories. The experimental rig consists of a wind tunnel running with air at ambient conditions, where the dynamic similarity is maintained by running at the same Reynolds number as in the original steam turbine. As a consequence of this, the blade loading is reduced with respect to the original steam turbine, reducing the strength of the secondary flow effects. Also high aspect ratio and low thickness-chord ratio contribute to making the secondary losses in this cascade a minor loss source with respect to the profile losses. Therefore, this turbine cascade stresses the necessity of a trade-off between added viscous losses and reduced secondary losses, making it a perfect test bench where to prove the general validity of this method.

All relevant geometrical features are reported in Tab. 4.1 and shown in Fig. 4.1.

Inlet blade angle, $\alpha'_1$	21.4°
Outlet blade angle, $\alpha'_2$	-68.2°
Thickness-chord ratio, $t/C$	0.171
Solidity, $s/C$	0.637
Aspect ratio, $AR$	2.6
Reynolds number <sup>1</sup> , $Re$	$7 \cdot 10^4$

**Table 4.1:** Main geometrical characteristics of the cascade employed for the methodology verification.

The baseline fence shape, shown in Fig. 4.1 (b) in the blade passage, differs from the fence concepts studied in previous investigations (see Sec. 2.3.5). The height distribution features a local increase at 25% of the camber line, aimed at intercepting the horseshoe vortex trajectory. The leading edge protrudes as a ramp from the



(a)



(b)

**Figure 4.1:** Representations of the turbine cascade geometry: (a) 2D sketch, (b) CAD view of the blade passage with the baseline shape of the endwall fence.

endwall, in order to avoid the creation of a stagnation region and, consequently, of an additional horseshoe vortex. Similarly to many other endwall fence configurations previously investigated, it is located in the middle of the passage and its camber line is the same as the blade. The geometrical features are reported in Tab. 4.2 and shown in Fig. 4.2. In Tab. 4.2,  $C_{bf}$  indicates the chord length of the baseline fence. The baseline fence has been provided by the research group of the Osaka Institute of Technology, who carried out an experimental investigation with the same turbine geometry.

Geometrical Features	Control Parameters	Values
Pitchwise position	$x_1$	51% $s$
Streamwise position	$x_2$	20% $C_{ax}$
Chord length, $C_{bf}$	$x_4$ and $x_6$	85% $C_{ax}$
Camber	$x_3$ and $x_5$	13% $C_{bf}$
Camber position	$x_3$ and $x_5$	37% $C_{bf}$
Thickness	$x_7, x_8$ and $x_9$	3% $C_{bf}$
1 <sup>st</sup> height	$x_{10}$	47% $\delta_{inlet}$
2 <sup>nd</sup> height	$x_{11}$	32% $\delta_{inlet}$
3 <sup>rd</sup> height	$x_{12}$	20% $\delta_{inlet}$
4 <sup>th</sup> height	$x_{13}$	20% $\delta_{inlet}$

**Table 4.2:** Geometrical features of the baseline fence. Parameter names ( $x_i$ ) are referred to the parameterization illustrated in Sec. 3.2.

Experiments pointed out that the baseline fence shape reduces the efficiency of the cascade because the additional profile losses introduced by the fence surface counterbalance the reduced secondary kinetic energy.

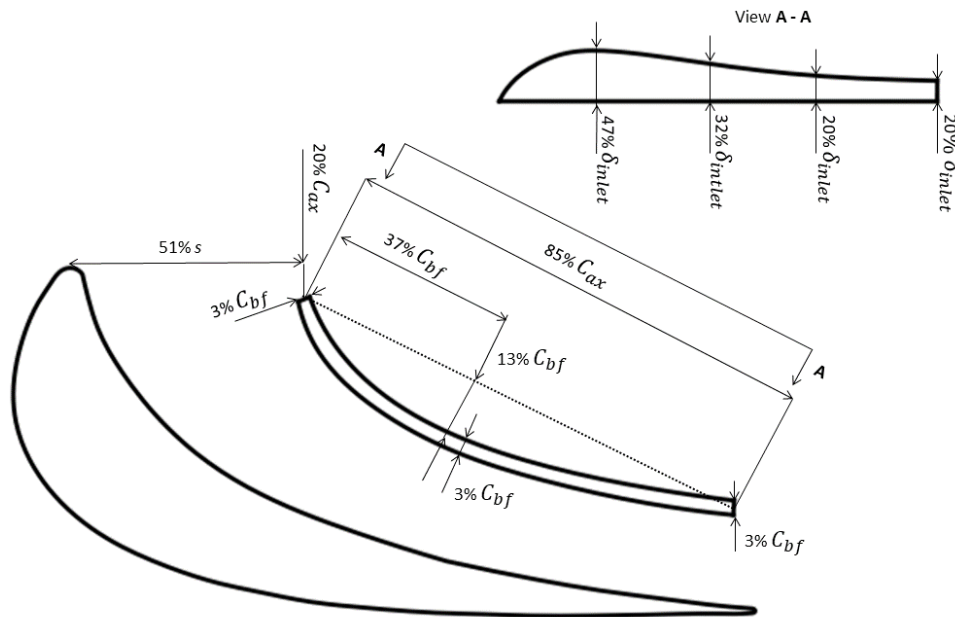


**Figure 4.2:** Schematic of the baseline fence shape with values of geometrical parameters.

The boundary conditions of the CFD simulations are set so as to reproduce the exact flow conditions present in the wind tunnel cascade where the validation has been performed, namely the test-rig at the Osaka Institute of Technology. A two-dimensional spanwise velocity distribution has been measured at a distance of one blade chord upstream of the cascade and is used as the inlet boundary condition. The inlet plane is positioned at the same distance from the blades. At the outlet is defined an average static pressure equal to the atmospheric pressure.

### 4.1.1. MESH INDEPENDENCE ANALYSIS

An analysis of the independence of the simulation results from the mesh refinement has been performed on the mesh of the flow passage with the baseline fence. The parameter used to assess the convergence of the solution is the total pressure loss coefficient  $C_{loss}$ , Eq. 4.1, the same used as objective function of the optimization. This is defined as:

$$C_{loss} = \frac{\overline{P}_{T,in} - \overline{P}_{T,out}}{\overline{P}_{T,in} - \overline{P}_{S,out}} \quad (4.1)$$

In Eq. 4.1 pressures in inlet and outlet plane are massflow-averaged (indicated with the overbar like  $\bar{x}$ ), according to Cumpsty and Horlock[65].

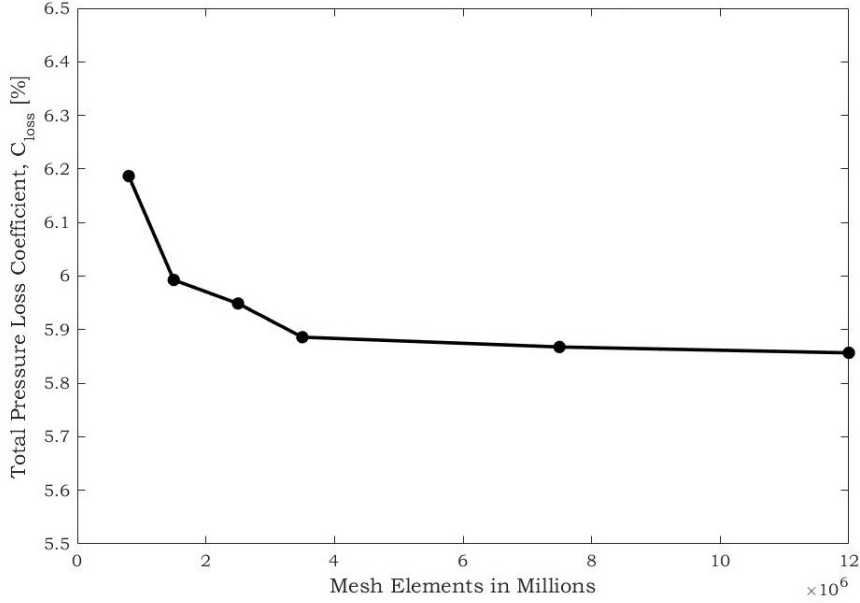


Figure 4.3: Mesh convergence analysis results.

The analysis has been carried out by keeping fixed the thickness of the first mesh element adjacent to the surfaces, in order to maintain the condition of  $y^+ \approx 1$  for every mesh size. The results of the analysis are shown in the plot in Fig. 4.3; for meshes made up by more than 3.5 millions of elements, the  $C_{loss}$  trend assumes an asymptotic behavior and the decrease from 3.5 to 12 million elements is within 0.5%. As a consequence, the mesh employed for the optimization had 3.5 million elements.

## 4.2. RESULTING RESPONSE SURFACE

The response surface produced for this case has been obtained with an OSF DOE of 100 design points. Each design point required more or less 240 minutes in CPU time, while the total optimization took around 400 hours in CPU time. On a cluster server using 16 CPUs the optimization took around 25 hours of calculations to return an optimal configuration.

The response surface is a multivariate function of 13 dimensions. As a consequence, in a 3D space it is possible to visualize the sensitivity of  $C_{loss}$  only w.r.t. two parameters at a time, keeping the others fixed. The analysis of the sensitivity of the different parameters w.r.t. the  $C_{loss}$ , indicates that the most relevant parameters are the pitchwise and streamwise position of the fence leading edge. Indeed, Fig. 4.4 shows the response surface of  $C_{loss}$  as a function of  $x_1$  and  $x_2$ , while the other variables have the values of Tab. 4.2, i.e. of the baseline fence. The trend shows a well-marked region of loss minimization; this region corresponds to the positions in which the fence leading edge intercepts the passage vortex core. In Fig. 4.5, on the left is shown the color plot of the response surface while on the right is reported the sketch of the turbine geometry. In the latter, the dashed line represents the pattern of the passage vortex. The optimal region, circled with a dashed line in the figure on the left, is highlighted with a grey ellipse in the cascade sketch, showing that the optimal position for the fence is located in the neighborhood of the vortex core. Moreover, the optimal position is also bounded in the

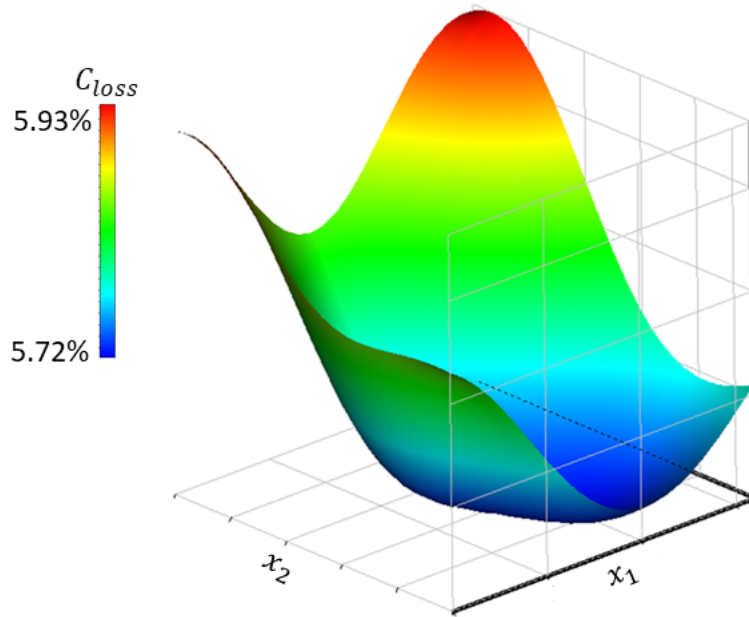


**Figure 4.4:**  $C_{loss}$  response surface for the fence leading edge position in pitchwise  $x_1$  and streamwise  $x_2$  direction against the .

streamwise direction: if the fence is located too close to the inlet or too much toward the trailing edge, the loss coefficient grows. In fact, when the fence is moved too close to the inlet the passage vortex is still weak, and profile losses are added without reductions in secondary losses. On the other way around, when the fence is moved too far downstream, it can not damp the passage vortex development.

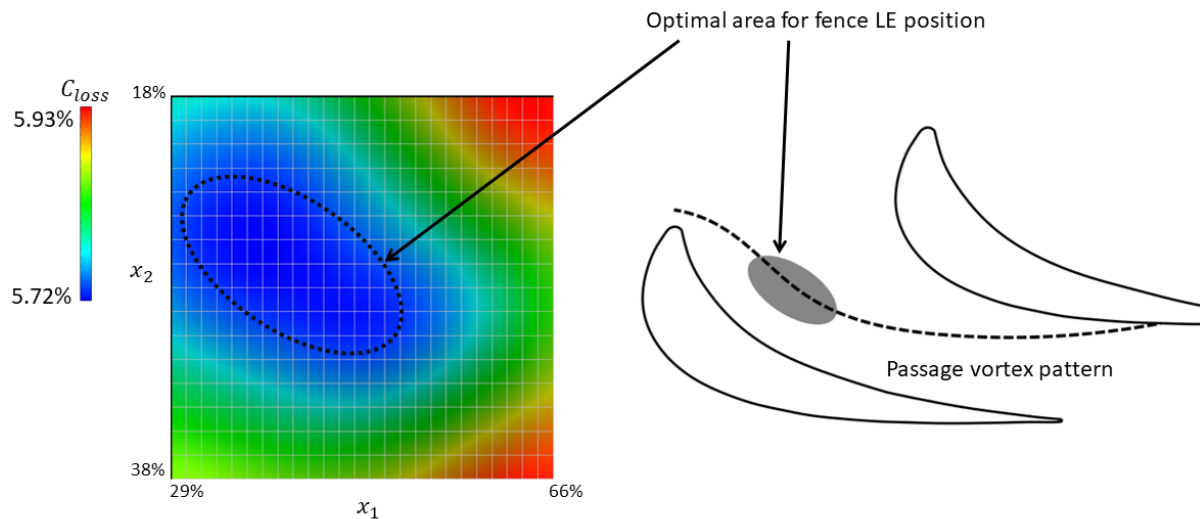


**Figure 4.5:** Identification in the cascade endwall of the optimal region for the fence position in the response surface.

The trend shown in Fig. 4.4 is not sensitive to the modification of the other fence parameters, proving that the fence position is decoupled from its shape. As a consequence, placing the fence leading edge in a position where the core of the passage vortex is intercepted, can be a design rule-of-thumb for endwall fences. Conversely, the other parameters are strongly coupled to each other, not allowing a clear visualization of their influence on the  $C_{loss}$ , as for the position.

### 4.3. OPTIMAL FENCE SHAPE

The optimal shape reduced the  $C_{loss}$  by 1.96% with respect to the baseline cascade without a fence. The geometrical characteristics of this fence are reported in Tab. 4.3 and represented in the illustration in Fig. 4.6. Here, the parameter  $C_{of}$  is the chord length of the optimal fence.

Geometrical Features	Control Parameters	Values
Pitchwise position	$x_1$	35% $s$
Streamwise position	$x_2$	33% $C_{ax}$
Chord length, $C_{of}$	$x_4$ and $x_6$	69% $C_{ax}$
Camber	$x_3$ and $x_5$	9% $C_{of}$
Camber position	$x_3$ and $x_5$	39% $C_{of}$
LE thickness	$x_7$	0.7% $C_{of}$
Half-chord thickness	$x_8$	3.6% $C_{of}$
TE thickness	$x_9$	2.7% $C_{of}$
1 <sup>st</sup> height	$x_{10}$	60% $\delta_{inlet}$
2 <sup>nd</sup> height	$x_{11}$	21% $\delta_{inlet}$
3 <sup>rd</sup> height	$x_{12}$	19% $\delta_{inlet}$
4 <sup>th</sup> height	$x_{13}$	0% $\delta_{inlet}$

**Table 4.3:** Geometrical features of the optimal fence. Parameter names ( $x_i$ ) are referred to the parameterization illustrated in Sec. 3.2.

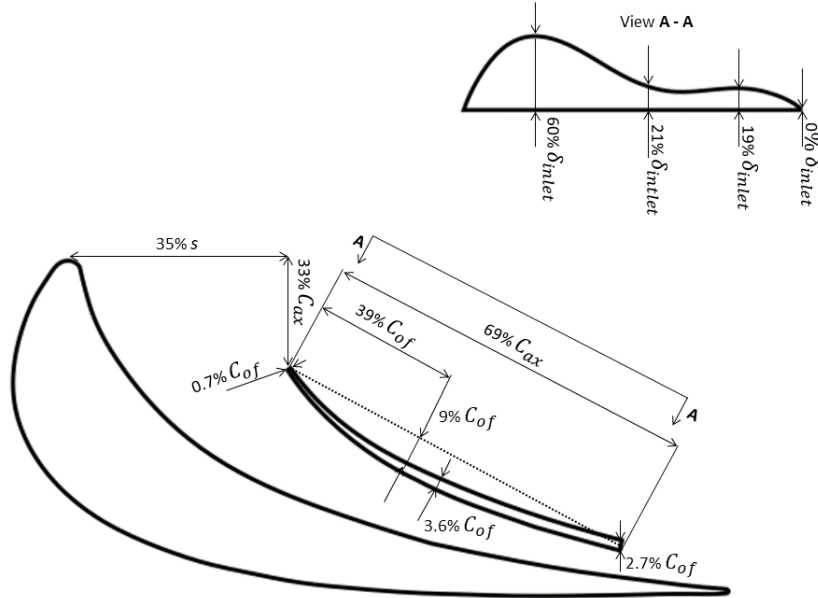


**Figure 4.6:** Schematic of the optimal fence with all the relevant dimensions.

Fig. 4.7 shows that the position of the optimal fence is shifted with respect to the mid-passage camber line. Instead, the fence configurations tested, or optimized, in previous studies were all positioned in the passage centre, as also the baseline fence described in Sec. 4.1. The leading edge of the optimal fence, is positioned in the region of optimal  $C_{loss}$  of the response surface discussed in Sec. 4.2, so in a position where the trajectory of the passage vortex is intercepted. Also, the fences available in the literature have the same camber line of the blade, while this fence is tilted toward the blade pressure surface. In Fig. 4.8 the baseline and optimal fence are compared. The height distribution of the latter resembles the baseline fence; both have the local height increase at 25% of the chord and a lower and flat portion toward the trailing edge, but the maximum height

of the optimal fence is 28% higher than the baseline. Specifically, the maximum height in the optimal fence is 60% of the  $\delta_{inlet}$ , which is also much higher than the 1/3 of  $\delta_{inlet}$  identified as optimum in different previous studies (Sec. 2.3.5). In addition, the fence height becomes zero at the trailing edge, joining the endwall and eliminating the squared shape causing a large wake in the cascade with the baseline fence. In general, the fence dimensions have been overall reduced, except for the maximum height: the optimal fence is 16% shorter, 80% thinner at the leading edge and 25% at the trailing edge. The resulting sharp leading edge, recalls the solution adopted by Chung and Simon in [57] and [58] to reduce the entity of the vortex forming at the fence leading edge.

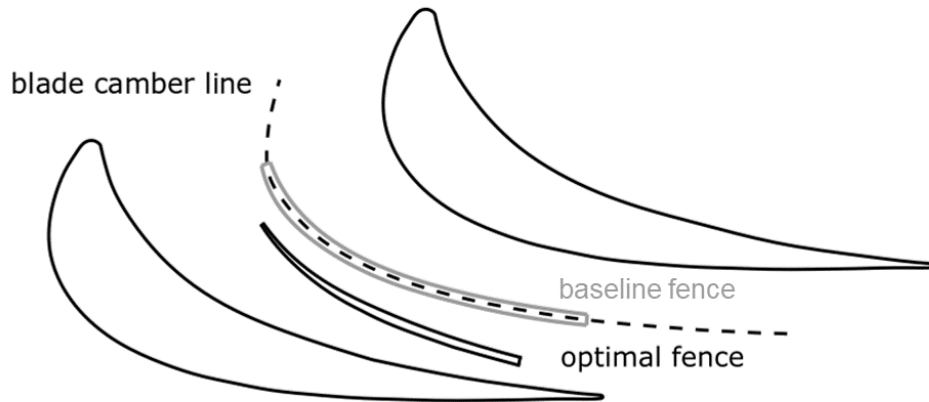


Figure 4.7: Optimal fence position and shape compared to the blade camber line passing for the middle of the passage.

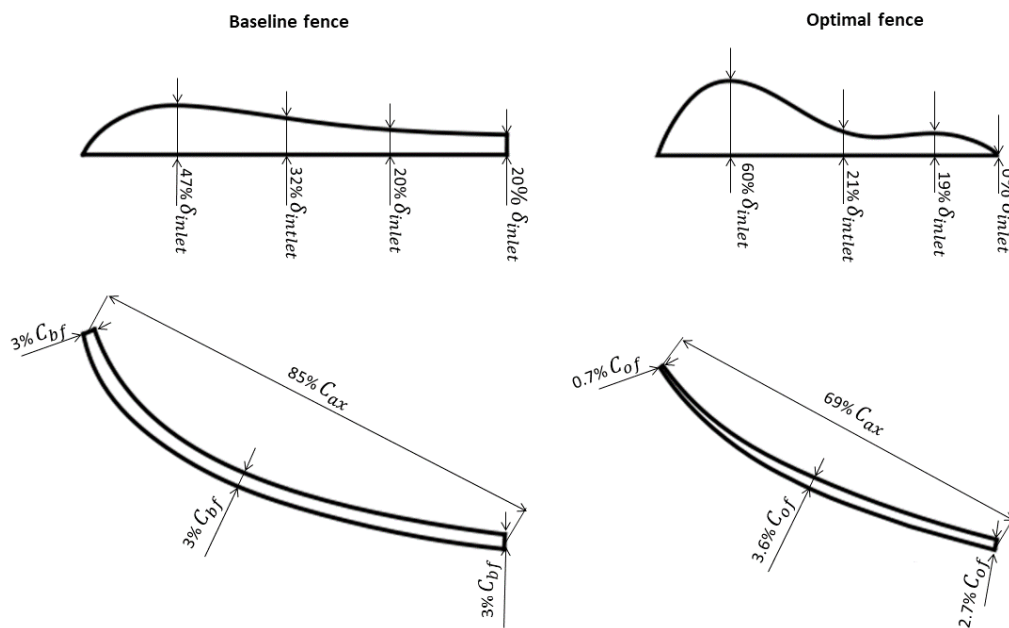


Figure 4.8: Comparison between optimal and baseline fence.

#### 4.4. PHYSICAL MECHANISM OF LOSS REDUCTION

In this section, we analyze the physical mechanism associated with the reduction of loss due to the secondary flow comparing the cascade with the optimal fence with the baseline cascade without the fence. The two quan-

tities used for the configurations comparison are the total pressure losses and the secondary kinetic energy. In order to quantify the amount of secondary kinetic energy, a mathematical definition of the secondary flow is needed. The secondary flow is defined as the component of velocity that is orthogonal to the  $\mathbf{V}_{bulk}$ , namely the vector having as components the mass flow averages of the velocity components over the plane considered,  $\bar{V}_x$ ,  $\bar{V}_y$  and  $\bar{V}_z$ . The definitions of  $\mathbf{V}_{bulk}$  and the secondary velocity  $\mathbf{V}_{sec}$  are reported respectively in Eq. 4.2 and Eq. 4.3:

$$\mathbf{V}_{bulk} = \begin{pmatrix} \bar{V}_x \\ \bar{V}_y \\ \bar{V}_z \end{pmatrix} \quad (4.2)$$

$$\mathbf{V}_{sec} = \mathbf{V} - (\mathbf{V} \cdot \hat{\mathbf{n}})\hat{\mathbf{n}} = \mathbf{V} - \left( \frac{\mathbf{V} \cdot \mathbf{V}_{bulk}}{|\mathbf{V}_{bulk}|^2} \right) \mathbf{V}_{bulk} \quad (4.3)$$

Once the secondary velocity is quantified in every point of the flow domain, a secondary kinetic energy coefficient  $C_{SKE}$  can be defined to give a meaningful global value to the phenomenon and estimate its entity in every plane. This can be calculated as:

$$C_{SKE} = \frac{\frac{1}{2} \rho \overline{V_{sec}^2}}{\bar{P}_{T,in} - \bar{P}_{S,in}} \quad (4.4)$$

Fig. 4.9 illustrates the flow domain with 8 sections indicated with dotted lines that have been used to study the streamwise evolution of  $C_{loss}$  and  $C_{SKE}$ . The axial position of these sections with respect to the blade trailing edge are reported normalized to the blade pitch  $s$  in Tab. 4.4:

Plane name	Axial position [% of $s$ ]
TE Plane	0
Plane 1	0.37%
Plane 2	0.74%
Plane 3	1.11%
Plane 4	1.48%
Plane 5	2.96%
Plane 6	4.44%
Plane 7	5.92%

**Table 4.4:** Axial distance from the blade trailing edge of the section planes indicated in Fig. 4.9. Distance normalized to  $s$ .

The information extracted for each of these sections are:

- a spanwise distribution
- a color plot with the planar distributions
- a mass flow average of the quantity over the section

The plots of spanwise distributions of  $C_{loss}$  and  $C_{SKE}$  are particularly convenient to analyze the causes of losses, and are a common tool in secondary flow research. The planar distributions allow quantifying the local peak values and recognize the secondary flow features. The mass flow averaged values are used to show the overall evolutions of  $C_{loss}$  and  $C_{SKE}$ .

For the color plots, both  $C_{loss}$  and  $C_{SKE}$  are expressed as flow properties defined in any point of the domain, modifying the definition of Eq. 4.1 as:

$$C_{loss} = \frac{\bar{P}_{T,in} - P_{T,out}}{\bar{P}_{T,in} - \bar{P}_{S,out}} \quad (4.5)$$

where the  $P_{T,out}$  is not averaged, contrary to Eq. 4.1. Eq. 4.4 is changed in:

$$C_{SKE} = \frac{\frac{1}{2} \rho \overline{V_{sec}^2}}{\bar{P}_{T,in} - \bar{P}_{S,in}} \quad (4.6)$$

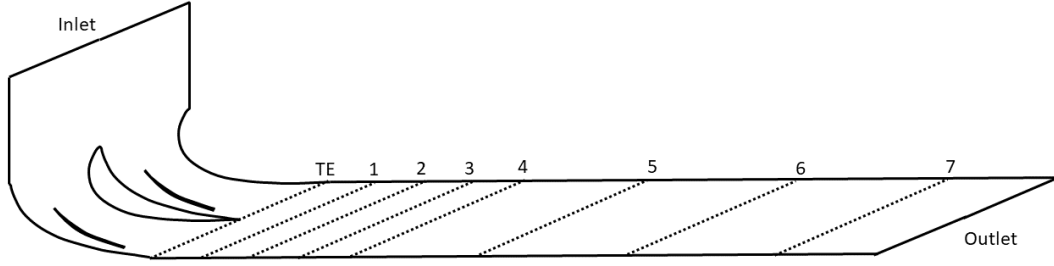


**Figure 4.9:** Planes used to study the evolution of  $C_{loss}$  and  $C_{SKE}$  spanwise distributions.

where also the values of  $V_{sec}^2$  are not averaged. The  $C_{loss}$  and  $C_{SKE}$  defined in Eq. 4.5 and Eq. 4.6 are mass flow averaged along the pitchwise direction to obtain the spanwise distribution plots. Precisely, the average has been calculated over pitchwise “stripes” having a height of 0.37% of the blade span. The dimensions of the stripes have been chosen to be consistent with the experiments.

Two parameters have been defined and plotted to indicate the local improvements/worsenings in  $C_{loss}$  and  $C_{SKE}$ , which are obtained with the optimal configuration. A  $\Delta C_{loss}$  is defined as:

$$\Delta C_{loss} = C_{loss,baseline} - C_{loss,optimal} \quad (4.7)$$

and a  $\Delta C_{SKE}$  defined as:

$$\Delta C_{SKE} = C_{SKE,baseline} - C_{SKE,optimal} \quad (4.8)$$

Where the  $\Delta C_{loss}$  and the  $\Delta C_{SKE}$  are positive,  $C_{loss}$  and  $C_{SKE}$  values have been reduced in the optimal configuration, while negative values indicate their increase.

#### 4.4.1. ANALYSIS OF $C_{loss}$

Sec. 2.2.3 describes the relationship between the trend in a spanwise loss distribution plot and the flow characteristics: essentially, the dimension of the  $C_{loss}$  peak depends on the size of the boundary layer  $\delta_{inlet}$  and the intensity of the crossflow. In Fig. 4.10, the peak in  $C_{loss}$  at 5-12% of span indicates the spanwise position of the passage vortex and of the separation line detached from the blade suction surface. The presence of a single peak suggests that the losses of the passage vortex are included in the peak of the separated flow, pointing out that the passage vortex is a region of a minor loss source as a consequence of the low blade loading. Fig. 4.10 shows how the loss profile develops with increasing distance from the blade trailing edge, for the baseline cascade and for the cascade with the optimal fence. Three features can be observed in this development:

1. Growth of boundary layer losses: this effect is due to the friction with the endwall and is worsened by the endwall crossflow.
2. Enlargement of loss peak: the loss peak enlarges both in terms of  $H$  (spanwise extension) and height. This means that energy is dissipated in that region even downstream of the cascade, under the effect of the flow mixing.
3. Spanwise penetration of the loss core: enlarging, the passage vortex pushes the wake of the separated flow away from the endwall.

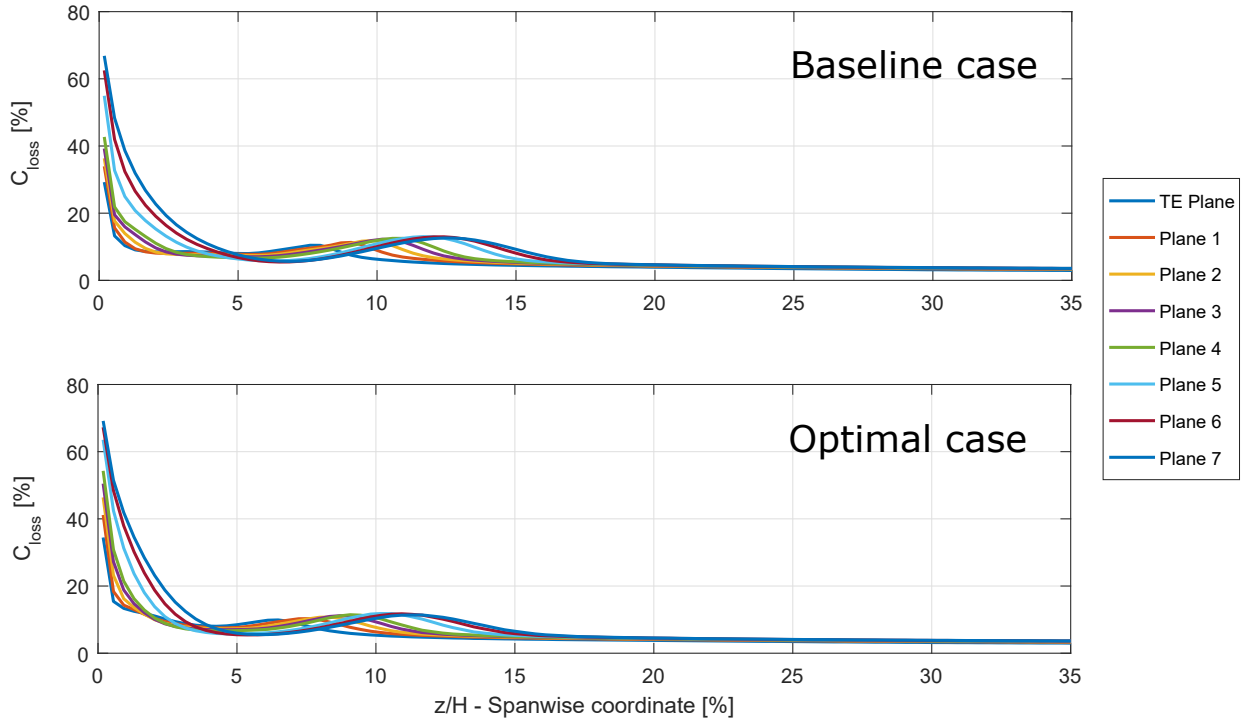


**Figure 4.10:** Comparison between evolution of  $C_{loss}$  spanwise distributions for baseline case and optimal case.

The loss distributions yield similar trends for the two configurations. Fig. 4.11 shows the comparison between the loss curves of the two configurations extracted at the same planes, i.e. TE Plane, Plane 4 and Plane 7. At the TE Plane the configuration with the optimal fence presents higher losses close to the endwall, with respect to the baseline geometry without fence. The loss peak of the optimal fence case is 5% higher than the baseline, respectively  $C_{loss} = 9.9\%$  w.r.t.  $C_{loss} = 10.4\%$ , but the latter is located 1.1% of the span length  $H$  closer to the midspan. Proceeding streamwise, in Plane 4, the endwall losses of the baseline configuration are the same as for the optimal case. Instead, the loss peak in the baseline grows more than in the optimal, both in height,  $C_{loss}$  is 9% higher, and in wideness, 20% larger. Also, the spanwise distance of the peaks increases to 1.5%  $H$ . In Plane 7, the endwall losses of the baseline case exceed those of the optimal geometry. Furthermore, the loss peak in the baseline case is 11% wider, 10.8% higher and located 1.11%  $H$  closer to the midspan w.r.t. the peak in the optimal configuration.

Fig. 4.12, 4.13 and 4.14 show the distributions of  $C_{loss}$  for baseline case and optimal fence case on the TE plane, Plane 4 and Plane 7. Five flow characteristics can be identified in each of these figures:

- blade wake: a stripe of low energy flow, going from the bottom to the top of the plot.
- wake of the separated flow: a loss peak in the wake, between  $z/H = 10-15\%$ .
- endwall boundary layer: a stripe of losses along the bottom of each plot.
- corner vortex: local enlargement of endwall boundary layer losses.
- passage vortex: diffused region of  $C_{loss}$  levels higher than 0, between the endwall and the separated flow.

Fig. 4.12 illustrates the TE Plane for both the baseline and the optimal, both showing the wakes of the separation bubbles between 5% and 10% of  $H$ . The separation bubble in the baseline is larger than in the optimal, suggesting that the passage vortex in the optimal case is weaker than in the baseline. However, the  $C_{loss}$  peak values are equal in the two configurations. Also, the low energy flow is still confined to the wake region and the passage vortex losses are hardly visible. The presence of the fence wake in the optimal case, on the bottom-left of the figure, provides a reason for the greater endwall losses in the optimal case, visible from the spanwise

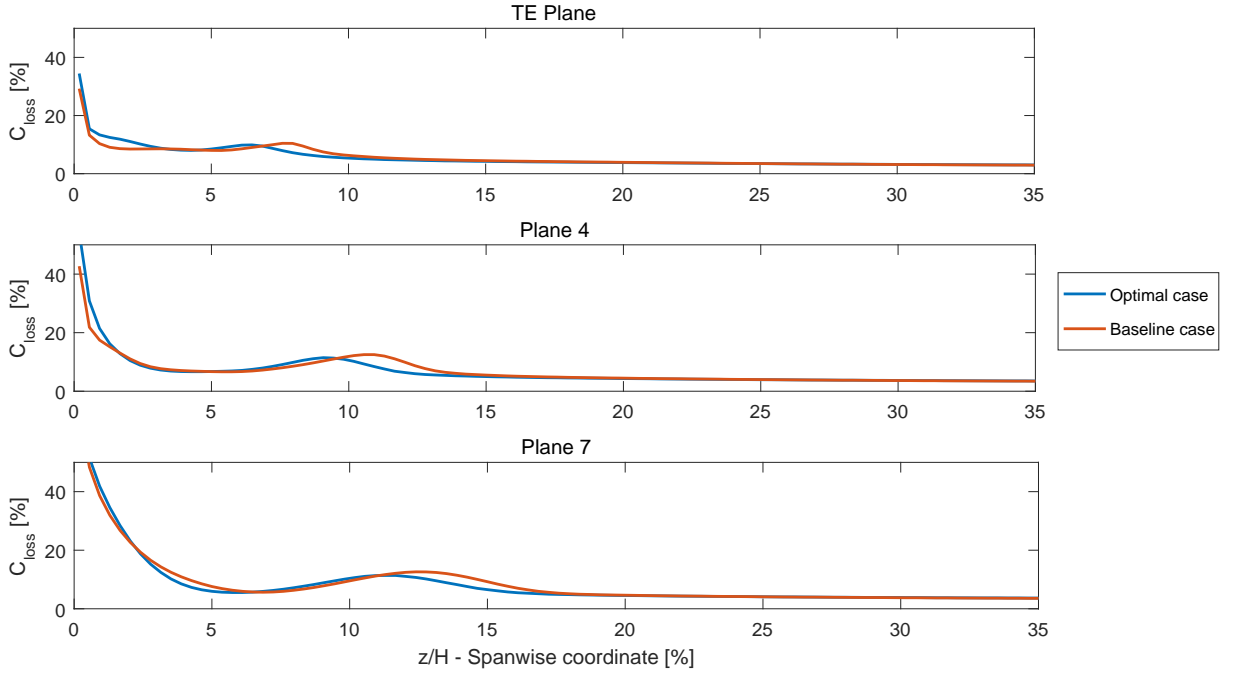


**Figure 4.11:** Comparison between  $C_{loss}$  spanwise distributions for baseline case and optimal fence case at the TE plane, Plane 4 and Plane 7.

distribution in Fig. 4.11. Fig. 4.12 (c) shows the difference in spanwise location of the separation bubbles in the two configurations. The fence wake is also visible as a region of negative  $\Delta C_{loss}$ , while the reduced strength of the corner vortex is highlighted by the positive region at the endwall.

Fig. 4.13 shows the distributions in Plane 4, where the loss peaks of the separations are enlarged and the peak values are decreased, compared to the TE Plane. The enlargement of the loss peak region is more relevant in the baseline than in the optimal, and the losses carried by the passage vortex are higher in the baseline than in the optimal. Instead, the  $C_{loss}$  peak is 1.5% higher in the optimal configuration. This suggests that a more severe mixing occurred downstream of the baseline cascade. Also the loss region of the corner vortex is bigger in the baseline than in the optimal case, showing that the endwall cross flow is stronger in the latter.

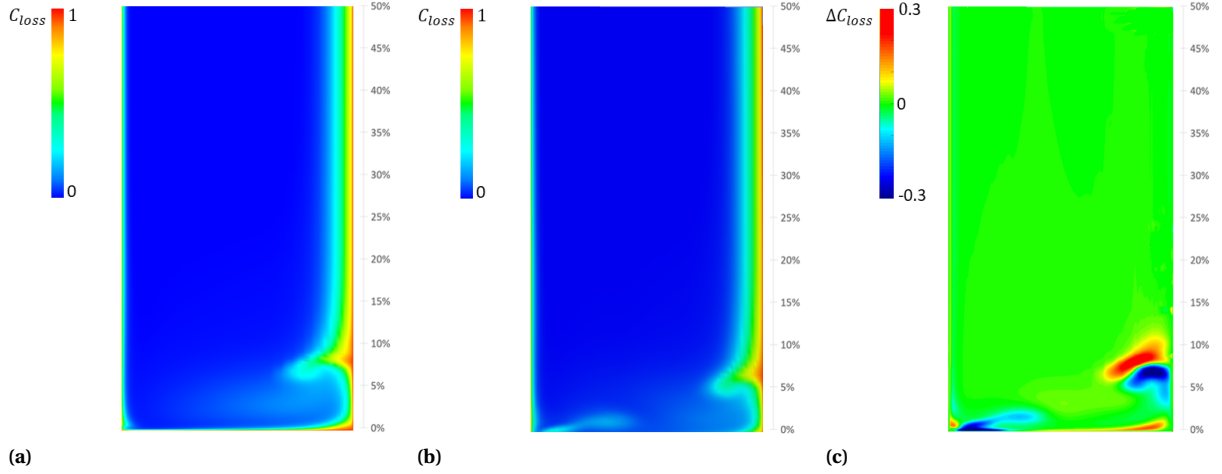
Fig. 4.13 shows that in Plane 7 both configurations feature diffused loss regions and distorted wakes. The endwall boundary layer of the baseline case is thicker than in the optimal. In Fig. 4.13 (c), a peak of  $\Delta C_{loss} = 0.08$  peak shows that the  $C_{loss}$  levels are still higher in the baseline configuration at a distance of 5.92  $s$  from the cascade.

Fig. 4.15 shows the evolution of the mass flow averaged  $C_{loss}$  in the two configurations, measured at the sections indicated in Fig. 4.9. The comparison shows that the value of  $C_{loss}$  at the TE Plane is the same for both the cascade geometries, but that in the optimal case the mixing losses are reduced downstream of the cascade.

#### 4.4.2. ANALYSIS OF $C_{SKE}$

The analysis of the  $C_{loss}$  development shows that the performance improvement found in the optimal case is due to the reduction of mixing losses. The analysis of the  $C_{SKE}$  development reveals how the decrease of secondary flow leads to the reduction of mixing losses.

Fig. 4.16 shows the development of the spanwise distributions of  $C_{SKE}$  for both the baseline and the optimal geometries. All of these curves show two peaks: the first peak corresponds to the endwall crossflow, while the second is due to the spanwise crossflow over the separated area of the blade surface. These are both parts of the passage vortex. The growing spanwise width of the peaks, the increase of their spanwise penetration and the decrease of the peak values, show that the SKE of the vortices diffuses and dissipates. In agreement with the analysis in Sec. 4.4.1, this energy is lost in the flow mixing, increasing the  $C_{loss}$  that grows, on the opposite of the  $C_{SKE}$ . The levels of  $C_{SKE}$  of the peaks in the baseline configuration shown in Fig. 4.16 are all larger than



**Figure 4.12:** Distributions on the TE Plane of: (a)  $C_{loss}$  for the baseline geometry, (b)  $C_{loss}$  for the optimal geometry, (c)  $\Delta C_{loss}$  between baseline and optimal case.

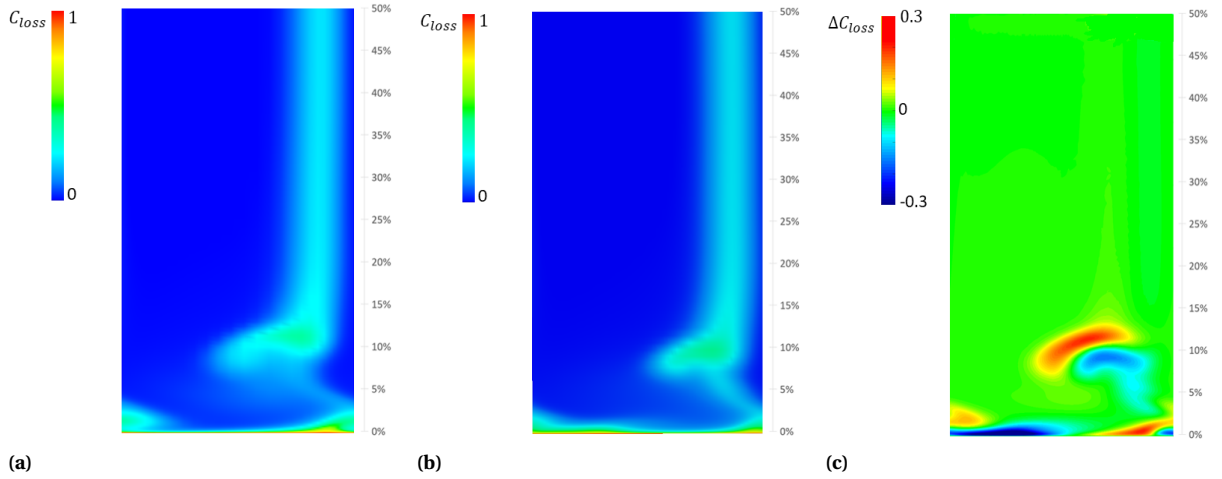


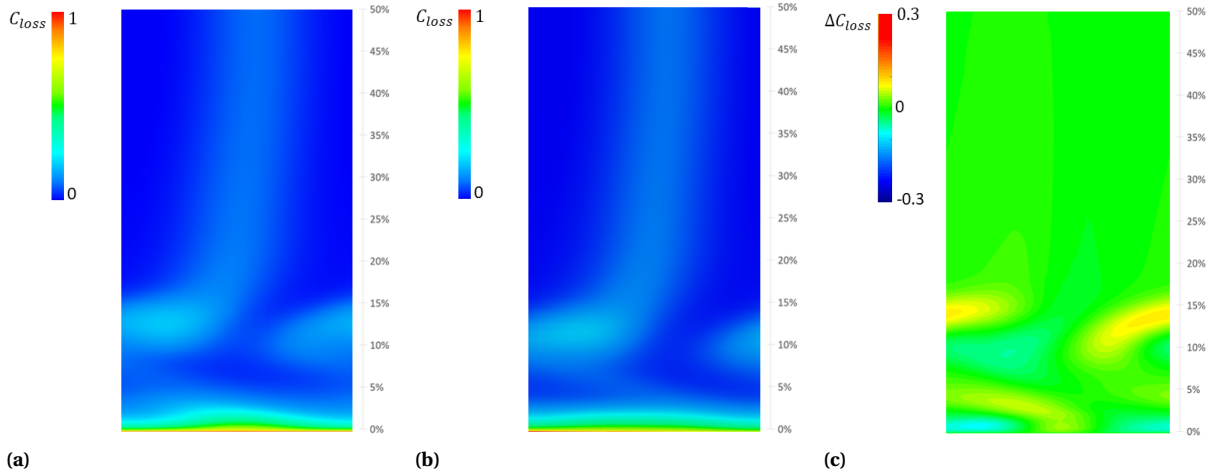
**Figure 4.13:** Distributions on Plane 4 of: (a)  $C_{loss}$  for the baseline geometry, (b)  $C_{loss}$  for the optimal geometry, (c)  $\Delta C_{loss}$  between baseline and optimal case.

in the optimal.

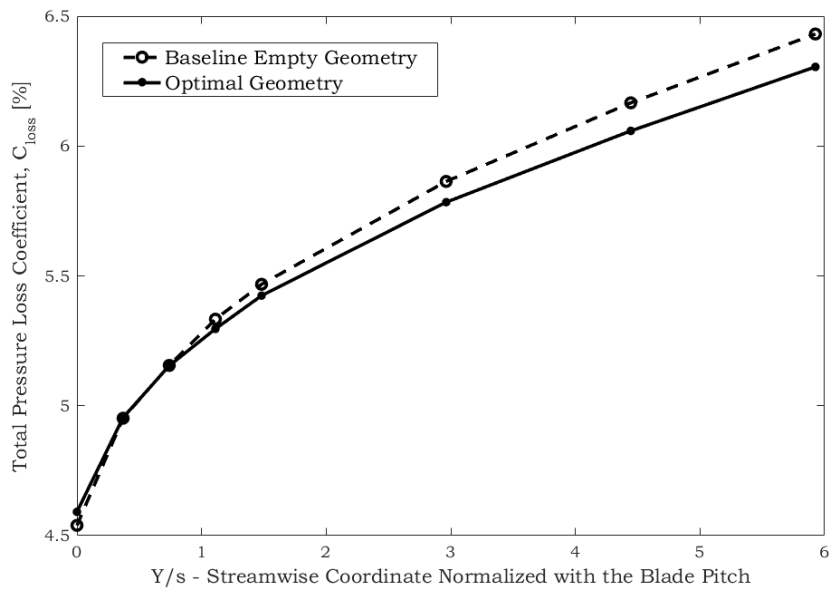
Fig. 4.17 compares the  $C_{SKE}$  spanwise distributions at the TE Plane, Plane 4 and Plane 7. In all of these three locations, the peak values found in the baseline case are always around twice as high as in the cascade with the optimal fence. At the TE Plane the secondary kinetic energy is confined to the region with spanwise coordinate  $z/H < 13\%$ , and the maximum  $C_{SKE}$  in the optimal case is 50% of the baseline. In Plane 4, two peaks are formed in both configurations, and both peaks have the same spanwise extension in the baseline and in the optimal geometry. The location of the second peak of the baseline  $C_{SKE}$  profile is 1.5%  $H$  closer to the midspan, while in Plane 7 this distance is reduced to 0.74%.

Fig. 4.18, 4.19 and 4.20 report the comparisons of  $C_{SKE}$  distributions for the two configurations in TE Plane, Plane 4 and Plane 7. A distribution of secondary velocity vectors has been added to provide a visual understanding of the vortical structures. Four flow features are visible in each of these figures:

- passage vortex: vortex of the dimensions of the blade pitch, confined within  $z/H < 10\text{-}15\%$ .
- endwall crossflow: the high- $C_{SKE}$  region at the endwall.
- spanwise crossflow: the high- $C_{SKE}$  region with secondary velocity directed toward the midspan.
- shed vortex: wake flow put into rotation by the passage vortex. Visible in Plane 4 and 7, for  $z/H > 10\%$ .



**Figure 4.14:** Distributions on Plane 7 of: (a)  $C_{loss}$  for the baseline geometry, (b)  $C_{loss}$  for the optimal geometry, (c)  $\Delta C_{loss}$  between baseline and optimal case.



**Figure 4.15:** Streamwise evolution of the  $C_{loss}$  for baseline and optimal case.

The corner vortex is only barely recognizable in the bottom corners of Fig. 4.19.

In both Fig. 4.18 (a) and (b), two wide passage vortices are present and strong secondary flow is located on the endwall and along the blade suction surfaces. In the baseline, the two crossflow regions are merged, indeed in Fig. 4.16 and Fig. 4.17 one only SKE maximum is visible; here, the  $C_{SKE}$  reaches the a value of 7.8%. In the optimized case the overall levels of  $C_{SKE}$  are concentrated in two separate smaller areas. In Plane 4, Fig. 4.19, the shed vortex is developed and the passage vortex is still clearly visible. The areas of the two crossflow regions have been strongly reduced, with peak values in the baseline case that are twice as large as in the optimal. In general, the  $C_{SKE}$  in the while region of the passage vortex is lower in the optimal than in the baseline. Proceeding to Plane 7, in Fig. 4.20, in both configurations the passage vortex is smaller, while the shed vortex remarkably enlarged, suggesting that part of the secondary kinetic energy is diffused to the low energy flow of the wake. The secondary kinetic energy is mostly dissipated or diffused, leaving the flow swirling with low secondary velocity. The local peaks of  $C_{SKE}$  are still visible as pitchwise stripes, one at the endwall and one around 10% of the blade span for the baseline. At the endwall, a crossflow is indeed still present. In the optimal geometry, these local  $C_{SKE}$  peaks are hardly visible.

In Fig. 4.21, the streamwise evolution of the secondary kinetic energy coefficient  $C_{SKE}$  is plotted for both

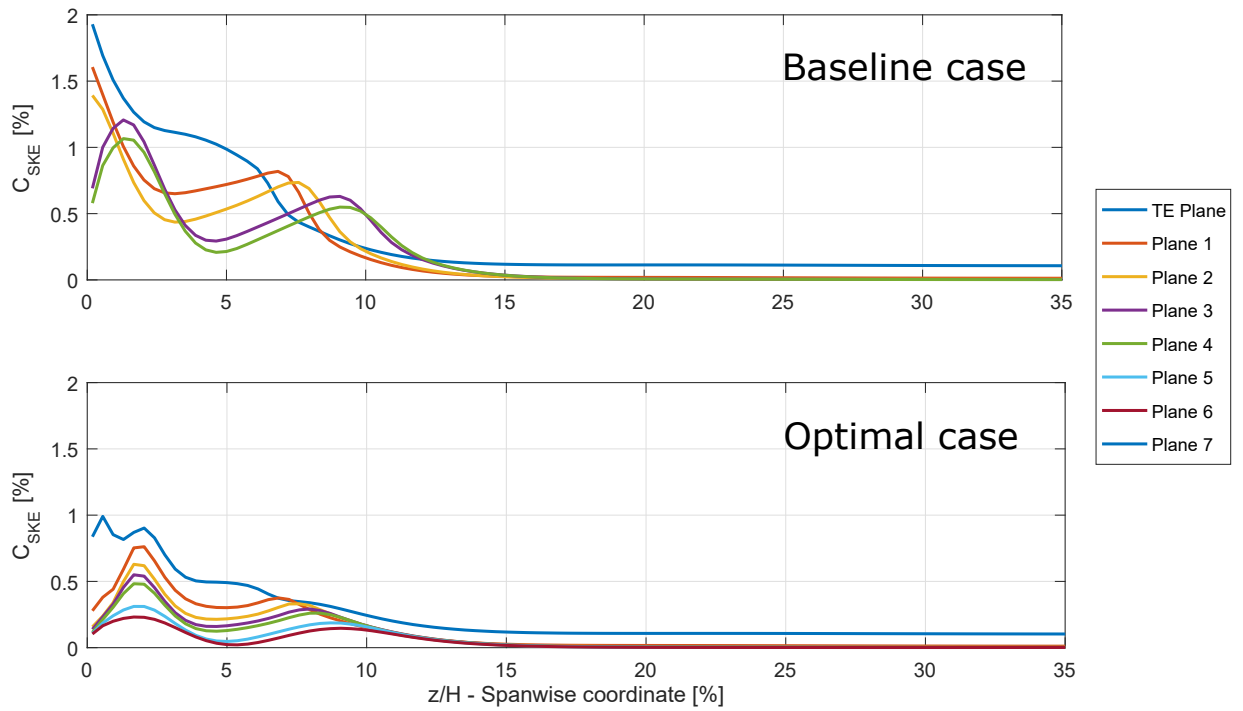


**Figure 4.16:** Comparison between evolution of  $C_{SKE}$  spanwise distributions for baseline case and optimal fence case.

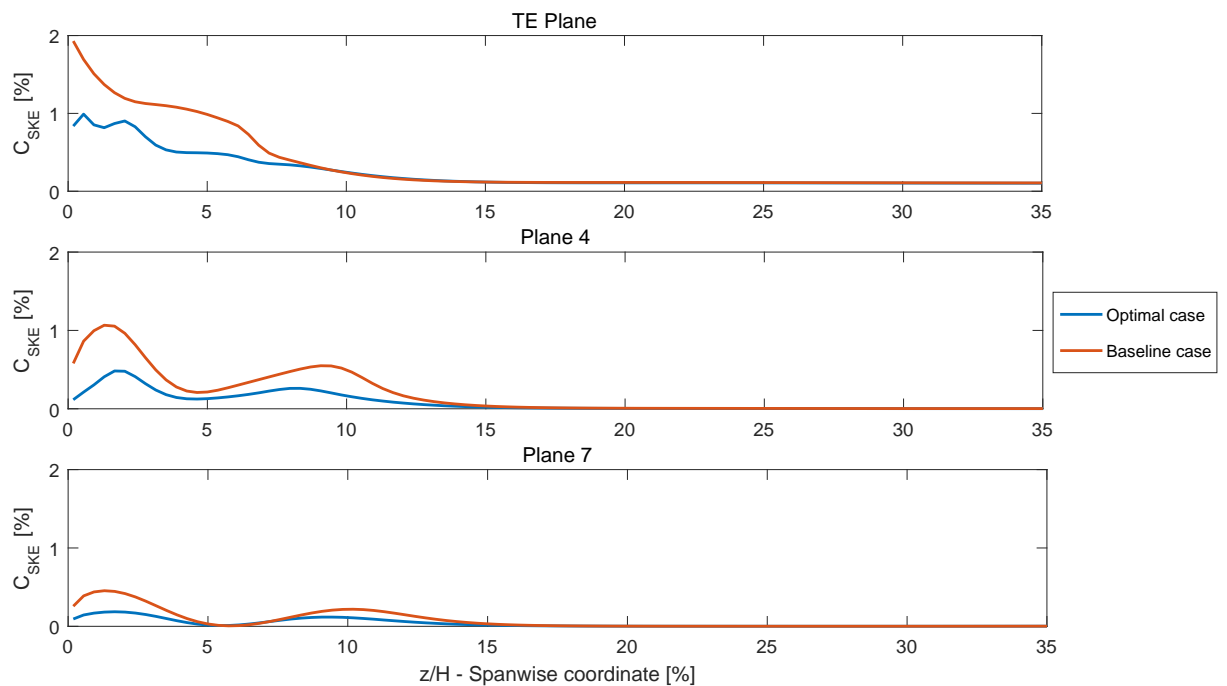


**Figure 4.17:** Comparison between  $C_{SKE}$  spanwise distributions for baseline case and optimal fence case on the TE plane, plane 4 and plane 7.

cases. The plot shows that the value of  $C_{SKE}$  in the two cases is the same upstream the fence. Immediately downstream, the vorticity starts to build up. The  $C_{SKE}$  grows up to a maximum value that is 34% higher in the

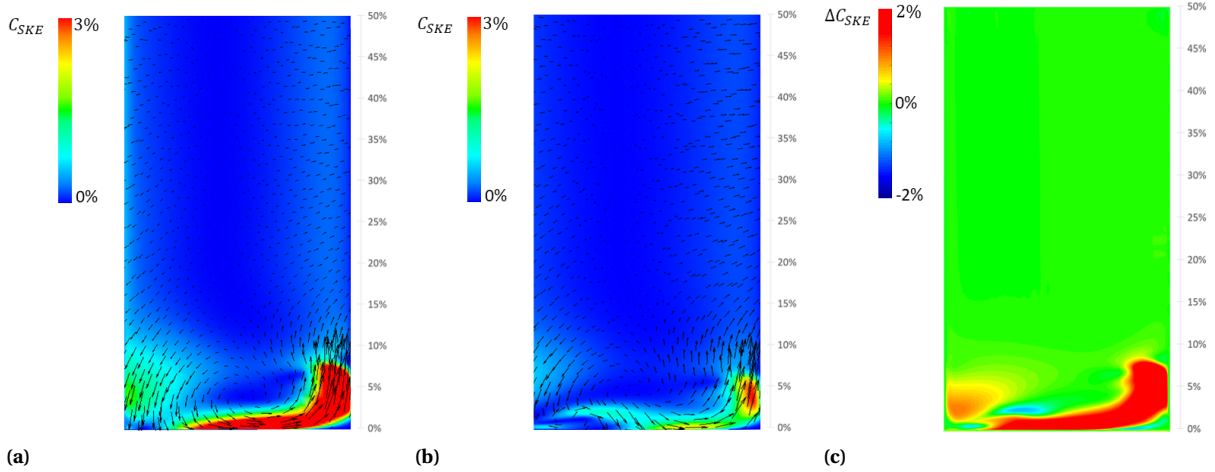


**Figure 4.18:** Distributions on the TE Plane of: (a)  $C_{ske}$  for the baseline geometry, (b)  $C_{ske}$  for the optimal geometry, (c)  $\Delta C_{ske}$  between baseline and optimal case.

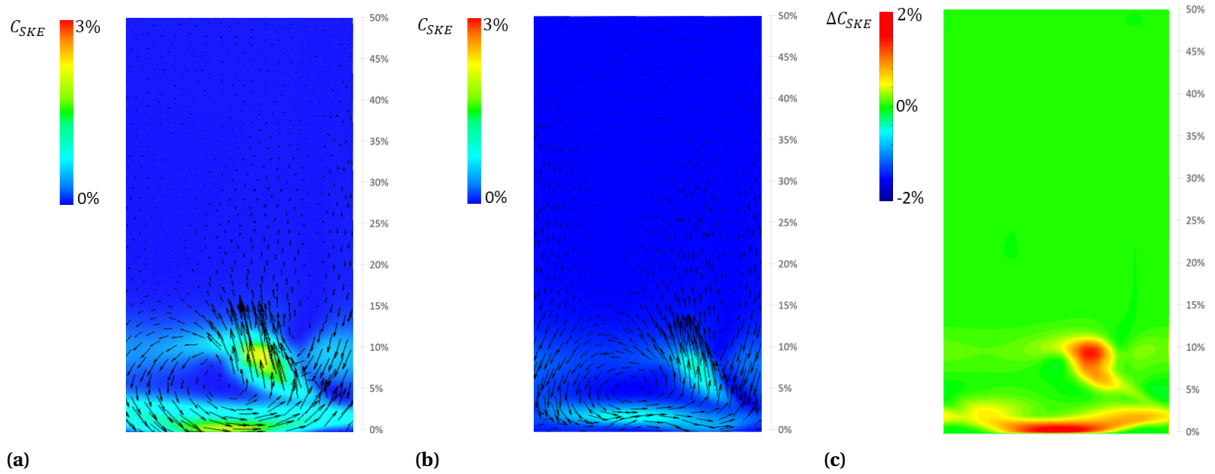


**Figure 4.19:** Distributions on Plane 4 of: (a)  $C_{ske}$  for the baseline geometry, (b)  $C_{ske}$  for the optimal geometry, (c)  $\Delta C_{ske}$  between baseline and optimal case.

baseline configuration than in the cascade with the optimal fence shape. The addition of the optimal fence prevents the intensification of a strong vorticity throughout the passage, as the fence is positioned where SKE reaches its peak value. The dumped growth of the vortex results in overall lower levels of SKE downstream the fence, reaching a reduction of the 48% of SKE at the outlet.

#### 4.4.3. DISCUSSION ON THE IMPROVEMENT MECHANISM

The reduction of 48% in SKE and of 1.96% in total pressure losses, are achieved by splitting the vorticity and reducing the crossflow. This is consistent with other studies in literature, as those of Clark et al. in [4] and of Prümper [51]. A weaker and smaller vortex crosses the blade passage and reaches the suction surface, due to the partition of the vorticity of the fence. Fig. 4.22 compares the development of the passage vortex in the baseline and in the optimal configurations. In the baseline configuration the vortex forms at the blade leading edge and grows while crossing the passage. In the optimal, as the fence intercepts the vortex trajectory (Sec. 4.2), it divides the vortex into two smaller vortices. The two passage vortices re-merge downstream in one passage vortex, which has the sum of the secondary kinetic energies of the two vortices. As explained in Sec. 2.2.5.4, the sum of the kinetic energy of these two smaller passage vortices is smaller than the kinetic energy of the single whole passage vortex, with equal inlet vorticity. This is the reason of the reduction of 48% in SKE.

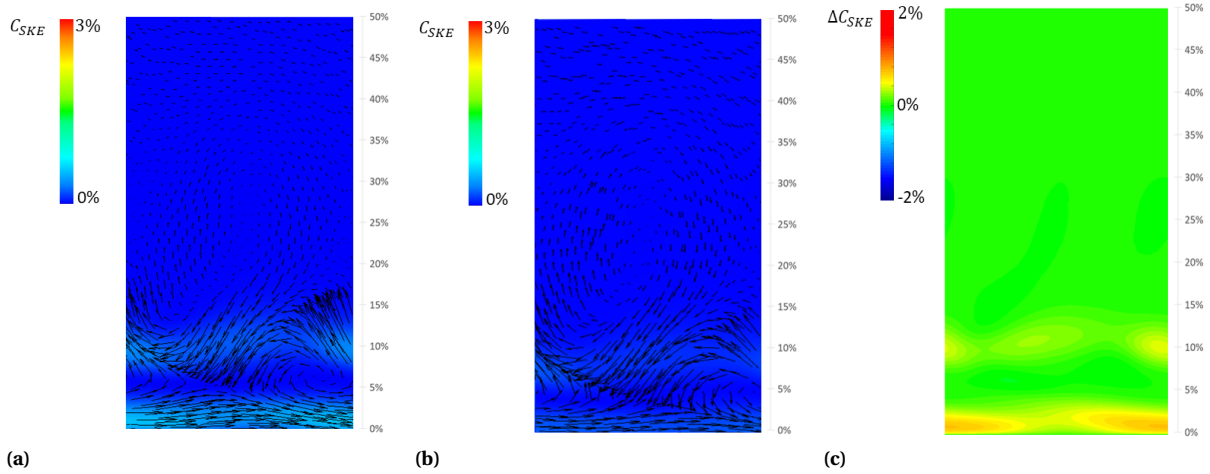


**Figure 4.20:** Distributions on Plane 7 of: (a)  $C_{ske}$  for the baseline geometry, (b)  $C_{ske}$  for the optimal geometry, (c)  $\Delta C_{ske}$  between baseline and optimal case.

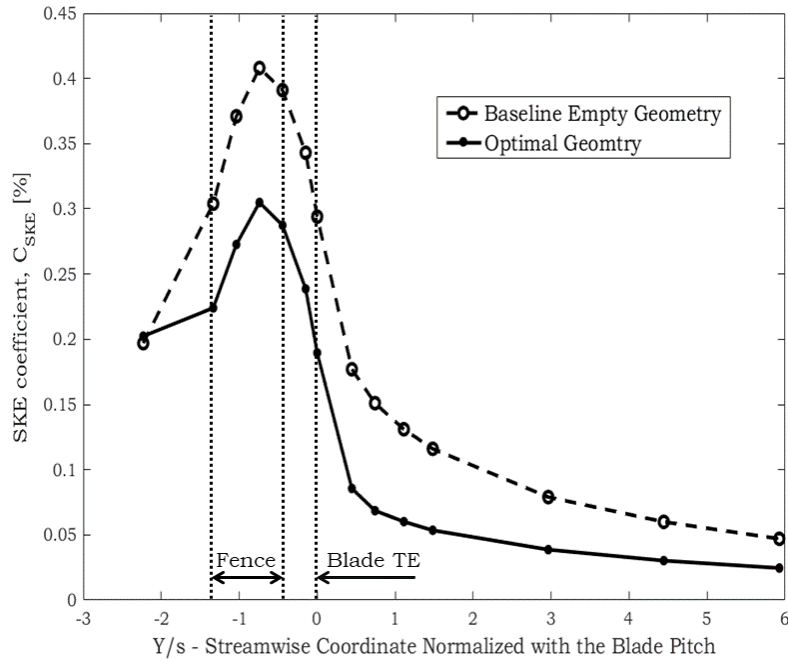


**Figure 4.21:** Streamwise Evolution of the Secondary Kinetic Energy Coefficient for Baseline and Optimal Case.

Fig. 4.23 illustrates the wall shear distribution over the blade suction surface, showing the region where the spanwise crossflow increases the shear on the blade suction side. In the optimal configuration the high-shear region is reduced of 22.4% with respect to the baseline, because of the weakening of the crossflow. This is in agreement with the results shown in Fig. 4.18, 4.19 and 4.20, where the peak of  $C_{SKE}$  of the optimal case is at lower  $z/H$  than in the baseline. Nevertheless, the overall profile losses produced in the cascade are exactly the same in both cases, as the reduction in shear stress on the blade surface is counterbalanced by the the fence profile losses. Coherently, in Fig. 4.15 the  $C_{loss}$  value of the two configurations is the same TE Plane.

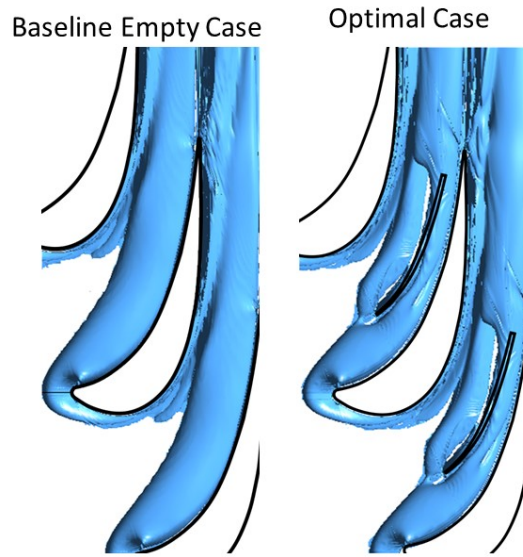


Figure 4.22: Comparison between vortex development in baseline and optimal cases.

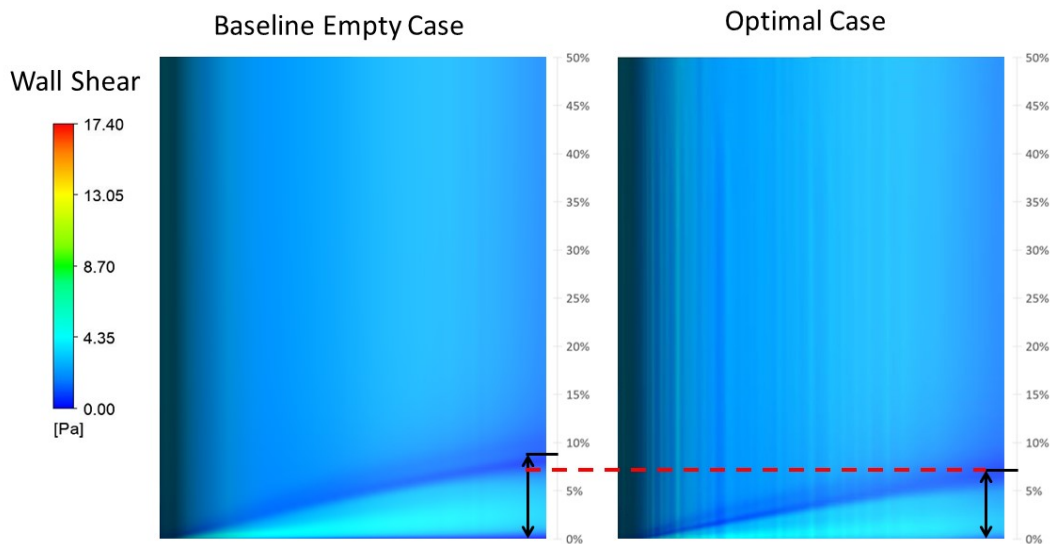


Figure 4.23: Comparison of wall shear distribution on the blade suction side for baseline and optimal configurations.



# 5

## EXPERIMENTAL VALIDATION

As already addressed in Sec. 2.4, the secondary flows in turbomachinery, and in particular the related total pressure losses, have always been problematic to predict with the CFD. The turbulence models implemented in the RANS are based on many assumptions, for instance, that the model constants are obtained via experiments for a high Reynolds number flows (Wilcox in [75]). In addition, human mistakes in the CFD settings must be considered as a possible reason of mistake. Therefore, the uncertainty on the simulation accuracy requires the accomplishment of an experimental validation to prove that the optimization worked. Specifically, it is necessary to verify that the improvement was actually achieved by comparing the experimental results of the baseline configuration with those of the optimal.

The experiments are carried out on a linear cascade wind tunnel, and consist in the measurement of static and total pressure fields downstream of the cascade. These data are elaborated to obtain the distributions of  $C_{loss}$  on the measurement plane, which are compared with the distributions from the CFD. The measurement plane is located at a fixed distance of 74%  $s$  downstream the blade trailing edge, namely in correspondence of Plane 2 in the CFD analysis, Fig. 5.1. Fig. 4.10 shows that both the baseline and the optimal cases have  $C_{loss} =$

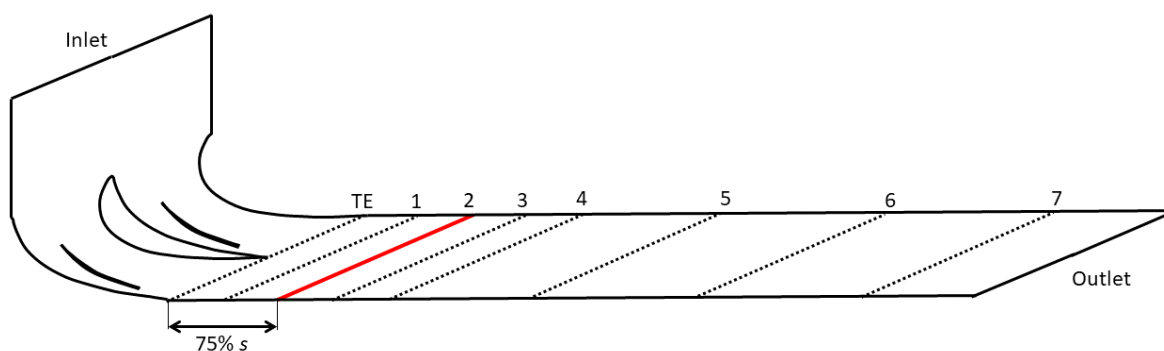


**Figure 5.1:** Position of the measurement plane in the CFD domain.

5.15% in Plane 2. In fact, the flow mixing that generates the losses occurs further away from the TE Plane, and the improvement of the optimal configuration is visible only from Plane 3 on. The measuring distance in the experimental setup is not adjustable, so it is not possible to do the measurements at a larger distance from the cascade. For this reason, the validation do not aim at finding an improvement in  $C_{loss}$ , but rather to find  $C_{loss}$  trends similar to those of the CFD simulations. Obtaining similar  $C_{loss}$  distributions, also the similarity of the flow field and of the  $C_{loss}$  evolution can be deduced.

This chapter presents the description of experimental setup and measuring procedure in Sec. 5.1, the assessment of experimental error in Sec. 5.1, and is concluded with the discussion of validation experiments in Sec. 5.3.

## 5.1. WIND TUNNEL EXPERIMENTS

The experiments are carried out in a wind tunnel linear cascade and total pressure and velocity measurements are taken upstream and downstream of the blade cascade. This section describes the test rig and the experimental procedure.

### 5.1.1. EXPERIMENTAL SETUP

The experiments are conducted in the wind tunnel linear cascade shown in Fig. 5.2. The setup features a rotatable support where the linear blade cascade is mounted; this feature allows the adjustability of the inlet flow angles. For the present work, the inlet blade angle is  $21.4^\circ$  degrees, in agreement with the fsimulatins in the optimizations. Upstream the cascade support, there is a small hole for the inlet Pitot tube, which is positioned at the exact middle of the channel and is aligned with the main flow direction.

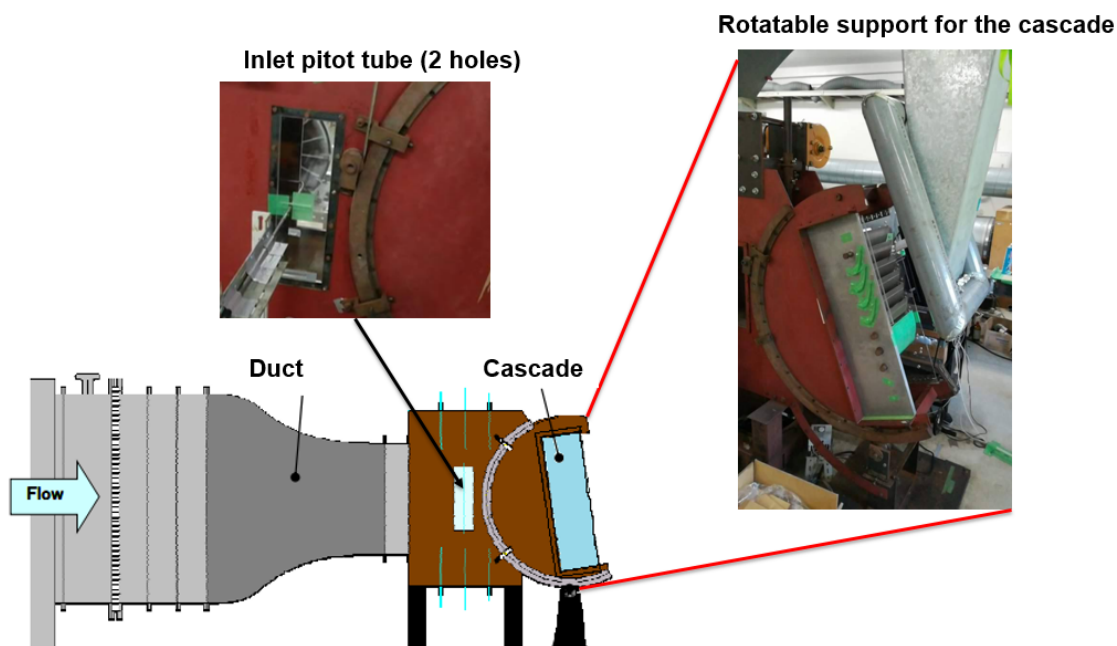


Figure 5.2: Drawing of the wind tunnel with zooms on the inlet Pitot tube and the rotatable cascade.

Downstream of the cascade the wind tunnel is opened. The opening allows to position the measurement apparatus and to rotate the inlet blade angle of the linear cascade. The air coming out of the cascade flows into a duct positioned about 4.4%  $s$  from the cascade and is driven outside the building. The wind tunnel works with a fan positioned at the inlet that is controlled by means of an inverter. The measurements of the outlet flow conditions are gathered by means of the apparatus shown in Fig. 5.3.

The measurement apparatus consists of a 5-holes Pitot tube that can be automatically positioned with a precision of 2 thousandths of a millimetre. A 5-holes Pitot tube is a particular probe allowing, not only to measure static pressure, total pressure and velocity, but also to know the flow direction. In fact, due to the presence of 5 holes positioned as shown in Fig. 5.4, it acquires 5 different total pressures that allow calculating the angles  $\alpha_p$  and  $\delta_p$ , presented in the same figure, knowing that:

$$P_2 - P_3 = f(\delta_p)$$

$$P_4 - P_5 = f(\alpha_p)$$

The tube total diameter is 2.8 mm, and each side hole has the center at a distance of 0.9 mm from the central one. Therefore, the measurement relies on the assumption that the flow feature variations are negligible in the area of the tube circle.

Fig. 5.5 illustrates the automatic positioning system. The apparatus is connected to a PC, where a program developed in LabView coordinates the movements and the measurements. The program sends the commands

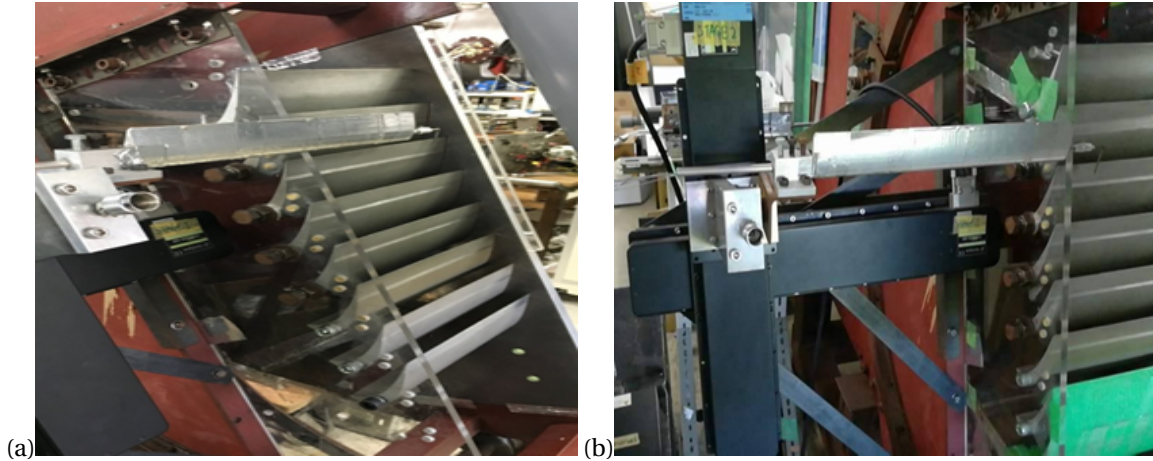


**Figure 5.3:** 5-holes Pitot tube positioned downstream of the cascade (a) and the automatic positioning system (b).

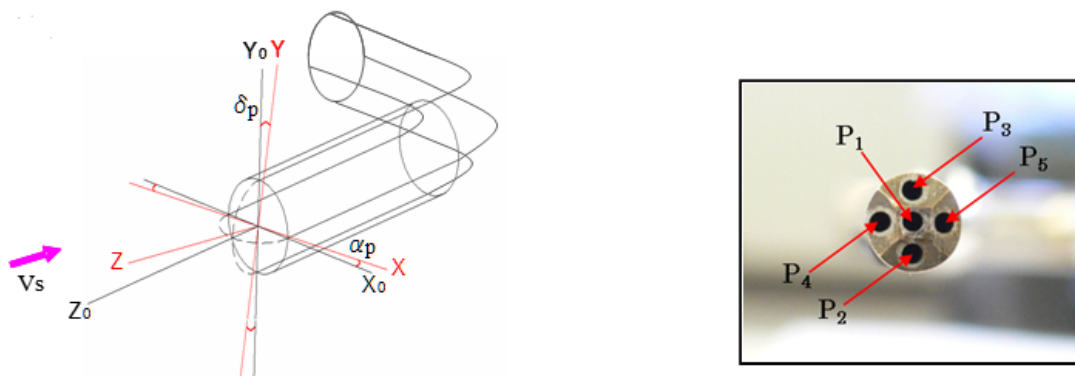


**Figure 5.4:** 5-holes Pitot tube orientation angles and holes positioning.

of motion to the controller, the positioning system moves the Pitot tube, and the PC transmits the input to the DSA for a new collection of measurements. This way, the measurement plane (Plane 2) is completely mapped, row after row, with a grid of points whose resolution can be set up at the beginning of the experiment. The DSA (Digital Sensor Array), in Fig. 5.6 is the device responsible for the data acquisition, connected both to the inlet Pitot tube and to the outlet 5-holes probe. The specific model used is a Scanivalve DSA3217. Static and total pressures are also recorded upstream of the cascade, with the fixed Pitot tube located in the center of the wind tunnel. Doing so, the pressure difference between the inlet and each point in the measurement plane is recorded, to calculate the  $C_{loss}$  for every location. The  $C_{loss}$ , by definition, accounts for the difference between inlet and outlet pressure, being independent on any oscillations of inlet conditions during the experiment. For each point of the measurement plane, 50 samples are gathered and averaged during the data post-processing. Fig. 5.7 shows the airfoil-shaped fairing that covers the tube; this solution has been adopted in order to limit the oscillations caused by the von Kármán wake to the cylindrical shape of the tube. The fairing section has the shape of a NACA 63<sub>4</sub> – 021 airfoil, which is a symmetrical airfoil so as not to generate any force. The fairing is also free to rotate around the tube, so that the fairing automatically turns to null its angle of attack with respect to the flow.

### 5.1.2. DATA ACQUISITION PROCEDURE

The acquisition procedure consists of three steps, which are coordinated in LabVIEW: the calibration, the inlet velocity adjustment and the launch of automatic experiment. The calibration is carried out with the wind tunnel turned off, and is considered accomplished when the probe measures a total pressure within the interval  $\pm 0.4\%$  of the relative inlet total pressure  $P_{T,in}$ . The adjustment of the inlet velocity is done by measuring the difference between total ( $P_T$ ) and static ( $P_S$ ) pressure at the inlet, i.e. the dynamic pressure  $P_D$ . The velocity is

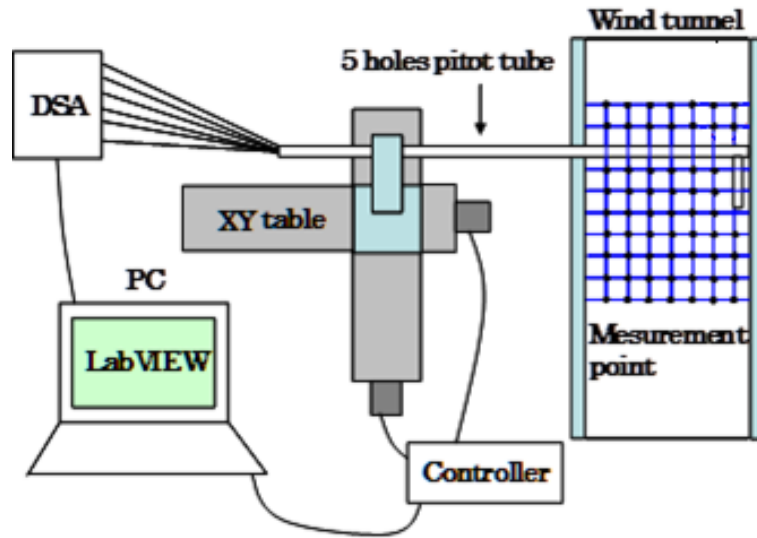


Figure 5.5: Schematic of the automatic positioning system.

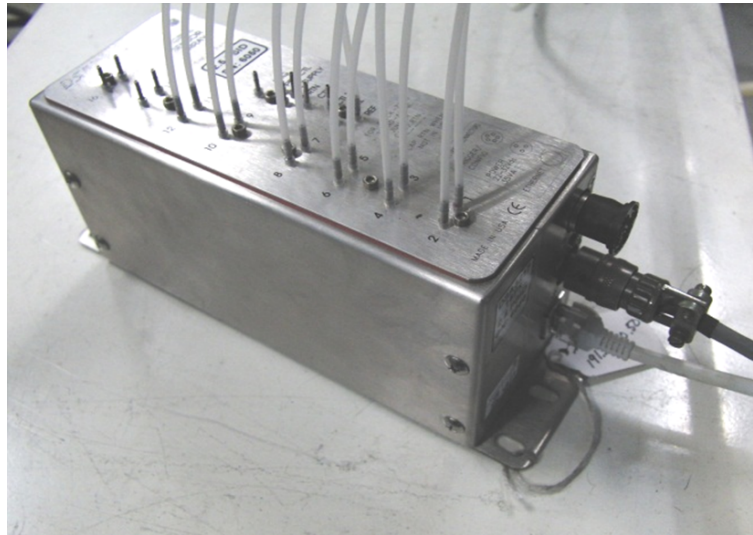
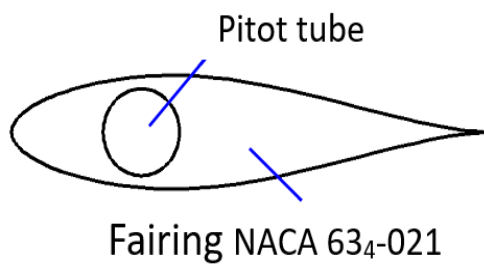


Figure 5.6: Picture of the DSA.



(a)



(b)

Figure 5.7: NACA 63<sub>4</sub> – 021 shape of the 5-holes Pitot tube fairing (a) and fairing picture (b).

derived according to the Bernoulli law:

$$\frac{1}{2} \rho V_{in}^2 = P_D = P_T - P_S$$

The velocity calculated with this procedure, is accepted within an error of  $\pm 0.5\%$  the inlet velocity  $V_{in}$ . The actual experiment is then automatically performed.

The data from the 5-holes Pitot tube are processed so to extract static and total pressures,  $P_T$  and  $P_S$ , velocity  $V$  and the angles  $\alpha_p$  and  $\delta_p$ , all as functions of the 5 pressures measured. The spacings between measurement points in the experiments presented in this work are: 7.4% of the blade pitch  $s$  in the pitchwise direction and 0.74% the blade span  $H$  in spanwise direction. In spanwise direction the pressure gradients are larger, in fact  $0.74\% H < 7.4\% s$ . Finally, a grid of total pressure loss coefficients is obtained; this is used to generate color plots of loss planar distribution and to obtain the loss spanwise distribution by pitchwise averaging the  $C_{loss}$ .

## 5.2. EXPERIMENTAL ERROR ASSESSMENT

A confidential interval for these measurements is necessary to assess whether the discrepancy between CFD and experiments is accountable to random errors of measurement. In particular, the uncertainty on the pitchwise averaged loss coefficient, so to see the error on the spanwise distribution and easily compare it with the discrepancy between experiments and simulations. Therefore, each experiment has been repeated 10 times, in order to eliminate the non-systematic errors.

The possible causes of non-systematic (random) errors identified, are:

- **calibration error:** as mentioned, values in the interval between  $\pm 0.4\%$  of the relative inlet total pressure  $P_{T,in}$  are accepted as a successful calibration.
- **weather conditions instabilities:** there is an influence of the weather conditions, in particular of strength and direction of the wind. It is remarkable to note that the building hosting the facility is situated next to a river, exposing both the inlet and the outlet of the wind tunnel to strong winds.
- **instrument error of measurement:** the DSA has a certain intrinsic uncertainty on its measurement. According to the information document, the declared accuracy is of  $\pm 0.2\% P_{T,in}$ .
- **error in inlet velocity:** when setting up the experiment, as explained in Sec. 5.1.2, the inlet velocity  $V_{in}$  is accepted within error  $\pm 0.5\%$ .
- **vibrations of 5-holes Pitot tube:** the arm sustaining the 5-holes Pitot tube undergoes vibrations during the experiment. Despite the airfoil-shaped fairing covering it, the last part of the probe is inevitably cylindrical, and this part is at the extremity of the stick, where oscillations are more easily generated (because of the larger moment of the force). These are considered as the largest source of uncertainties, as also the error bar distribution suggests. In fact, the largest probe's vibrations occur while measuring the region closer to the endwall, where the tube is subject to the 3D oscillations caused by the vortices, leading to larger uncertainties right in the area of higher interest.
- **flow unsteadiness:** a certain degree of unsteadiness can be expected to take place in a flow with such a low Reynolds number, causing discrepancies among measurements taken in the same location but in different experiments.

To take into account all the sources of uncertainties, has been defined an interval within which each measurement *probably* lays. Using the widespread *standard deviation* as interval centered in the average value, the probability that the "real" value is inside the interval is 68.2%. The standard deviation is defined as:

$$\sigma = \sqrt{\frac{\sum_{i=1}^N (x_i - \bar{x})^2}{N}} \quad (5.1)$$

where  $\sigma$  is the standard deviation,  $N$  is the number of experiments,  $x_i$  is the  $i$ -th experimental value and  $\bar{x}$  is the average of all the experimental values. The 10 experiments carried out per configuration returned 10 different distributions of  $C_{loss}$ . As the data are collected at the same location, the consistency of position allows to average among the  $C_{loss}$  of all these experiments. The standard deviation is calculated through Eq. 5.1 and the confidence interval is defined by the adding and subtracting  $\sigma$  from the average.

The same procedure to estimate the confidence interval is used for the loss distributions on the plane and along the spanwise direction. The difference is that for the planar distributions the averages and the standard

deviations are calculated for each grid point on the measurement plane. For the spanwise distributions, the averages and the standard deviations are calculated with the pitchwise averaged that correspond to the same spanwise location. However, these are not visible in the plots reported.

### 5.3. VALIDATION RESULTS

The results of the validation are presented below, showing first the validation of baseline and optimal configurations independently and later the validation of the deviation between the two configurations.

#### 5.3.1. INDEPENDENT VALIDATIONS OF BOTH CONFIGURATIONS

Fig. 5.9 shows the comparison between the spanwise  $C_{loss}$  distributions from the CFD simulations and from the wind tunnel experiments. The measurements have been limited to the endwall region, for  $z/H < 20\%$ , where the secondary flow is located. The experimental data are the averages of the 10 experiments, and the error bar representing the confidence interval is calculated as explained in Sec. 5.2. The CFD results do not fall within the interval of confidence found, which is actually rather small, except at the endwall. The CFD results are upward shifted from the experimental data, indicating that the turbulence model over-estimated the losses. The opposite happens at the endwall. Nevertheless, the overall trend seems to be fairly captured. In particular, the correct modelling of the spanwise position of the  $C_{loss}$  peak, suggests that the of secondary flow has been correctly calculated. The larger uncertainties of measurement are located in correspondence of the peaks of secondary kinetic energy, as can be seen comparing Fig. 5.9 with Fig. 4.16. This suggests that the error is mainly due to the vibrations of the Pitot tube that are caused by the vortex.

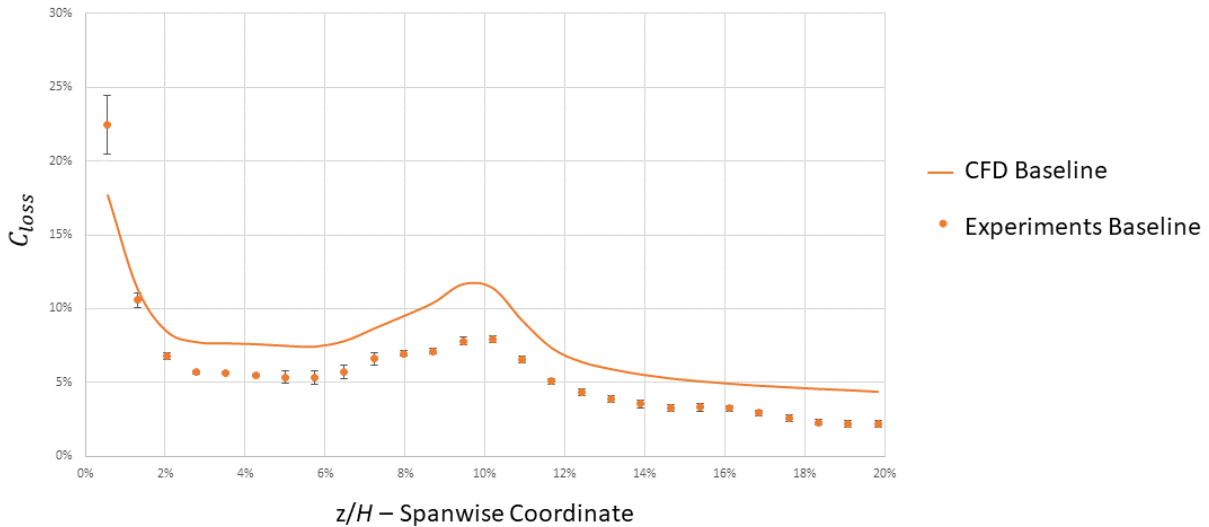
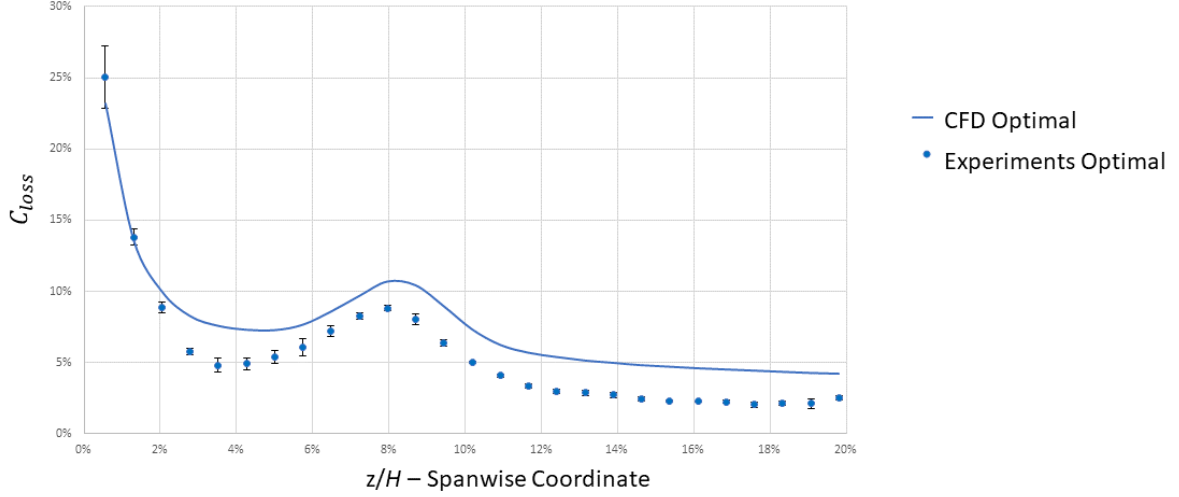


**Figure 5.8:** Comparison of  $C_{loss}$  spanwise trends between CFD results and wind tunnel experiments for the baseline configuration.

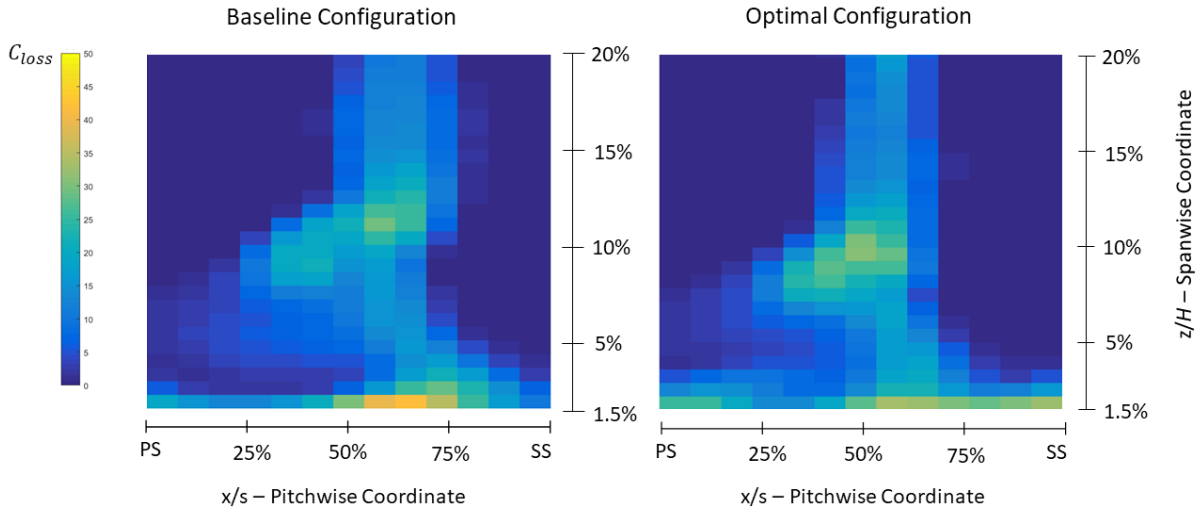
Similar considerations also apply to Fig. 5.9, for the validation of the CFD simulations of the optimal configuration. The CFD results show an over-estimation of losses, but the trend is well captured. Also for these experiments the interval of confidence is slightly larger for  $z/H > 2\%$  to  $z/H < 5\%$ , where the secondary flow induces stronger vibrations on the probe.

Fig. 5.10 shows the  $C_{loss}$  distributions acquired with the experiments for the baseline and the optimal configurations. These data are the average among measurements took in the same points in the different experiments performed. The local error bars could not be plotted in these graphs because they would require a 3D visualization. In Fig. 5.10 the following features can be recognized: the loss peaks close to  $z/H = 10\%$ , the wakes, and the corner vortex peaks at the junction between endwall boundary layer and wake, in  $z/H = 1.5\%$  and  $x/s = 65\%$ .

However, the trend is hardly recognizable, because of the low resolution. Hence, in order to facilitate the



**Figure 5.9:** Comparison of  $C_{loss}$  spanwise trends between CFD results and wind tunnel experiments for the baseline configuration.



**Figure 5.10:** Planar  $C_{loss}$  distributions from wind tunnel experiments for the baseline and the optimal configurations.

comparison with the CFD, these data have been interpolated with cubic splines so to have a continuous map to plot. Fig. 5.11 shows the comparison of the baseline case. The simulation captured the trend and the position of each feature correctly, also in the pitchwise direction. The area of smooth loss diffusion for  $x/s < 65\%$  and  $z/H < 10\%$  indicates the loss region of the passage vortex. As its dimensions and location are well captured, the passage vortex is considered successfully modeled. Also the loss peak of the corner vortex is visible in the same position in both the figures. However, in the experiments the wake of the corner vortex is barely visible while a larger region of high losses is distributed along the endwall. Also, according to the experiments, in the main flow the  $C_{loss}$  is null everywhere, while losses are diffused all over the flow in the CFD simulations.

The same applies to the optimal configuration. In Fig. 5.12 the interpolated data are compared with the CFD results. Again, the shape and position of the peak are accurately captured. However, the peak in the CFD results exceeds the 52%, while the peak in the experiments only reaches  $C_{loss} = 33\%$ .

Therefore, the difference in local  $C_{loss}$  values is relevant in regions of low energy flow. To quantify the over-estimation in each point, a validation error has been defined as:

$$\epsilon = C_{loss,CFD} - C_{loss,exp} \quad (5.2)$$

The distribution of  $\epsilon$  for both the geometries is reported in Fig. 5.13. The over-estimation regards particularly the loss peaks and wakes above it ( $z/H > 10\%$ ), while the CFD loss prediction is closer to the experiments

for lower  $z/H$ . Indeed, in the upper region, the losses predicted are more than twice larger than the actual experimental values. The same also applies to the wake of the corner vortices, visible in correspondence of the endwall. Regions of negative  $\epsilon$  surround the wakes and extend to the endwall boundary layer. This seems to indicate that the loss diffusion toward the mainstream flow is in general under-estimated.

The positions of passage vortices and separation lines have been correctly predicted. This suggests that the secondary flow has been successfully modeled, as the spanwise penetration of the vortex, with a same inlet vorticity, only depends on vortex size. However, the loss over-estimation reaches the 64% of the experimental values in peak zones (33% against 52%). This large over-estimation of losses can imply an over-estimation of the loss reduction as well, up to nullify the validation. For this reason, the next section presents the validation of the loss reduction.

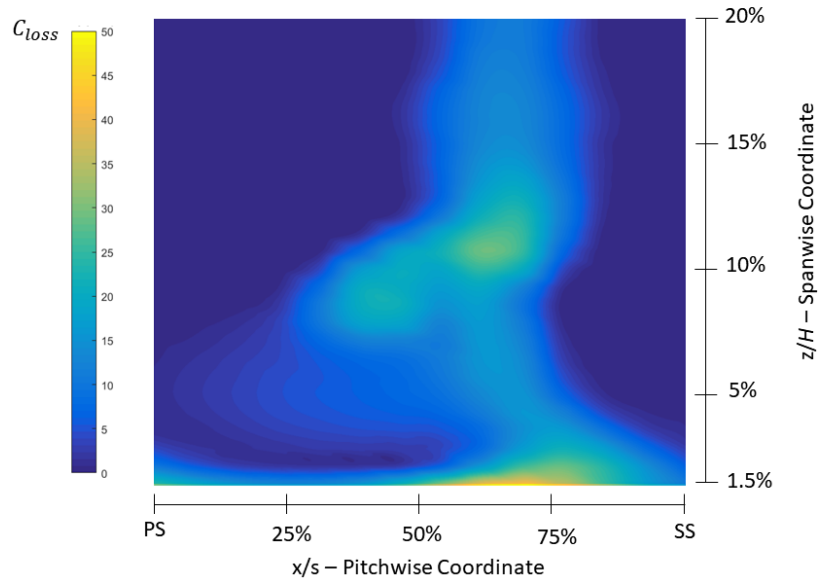
### 5.3.2. VALIDATION OF THE OPTIMIZATION

In Ch. 4, the conclusion of the comparative analysis between the optimal and the baseline cases is that the reduced secondary flow strength implies lower mixing losses downstream the cascade. In Sec. 5.3.1, the correct prediction of the loss trends in the measurement plane, both two-dimensional and three-dimensional, have been assessed for both the configurations. This proves that there is a similarity between the flow fields in experiments and simulations. However, the loss over-estimation could result in an over-estimation of the loss reduction; to validate the improvement, the validation of the difference between baseline and optimal configuration is performed.

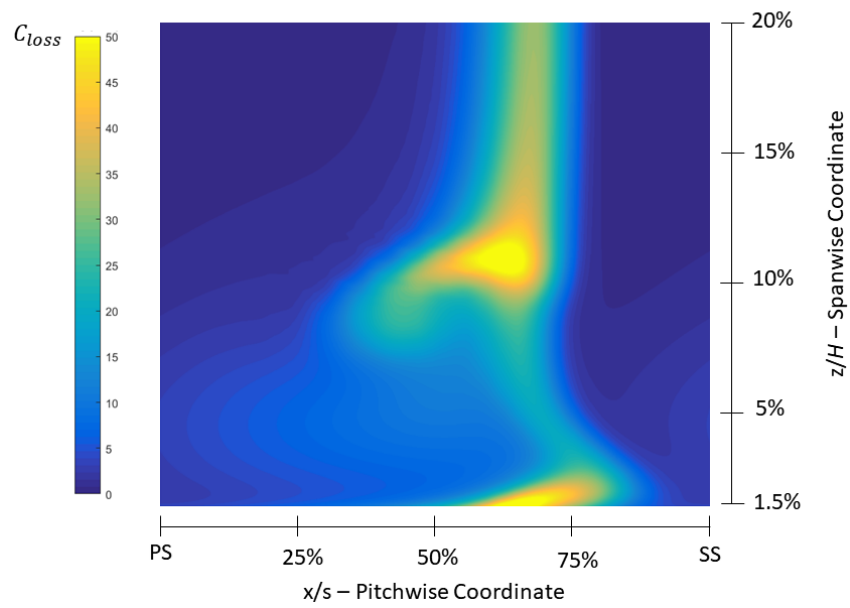
In Fig. 5.14 (a) and (b) show the comparisons between the baseline and optimal configuration of the spanwise  $C_{loss}$  distributions for the CFD and for the experimental results. The loss peak for the baseline configuration in the CFD reaches the 11.7%, surpassing the peak value of the optimal, 10.7%. Conversely, in the experiments the baseline peak is at 7.9%, lower than the 8.8% reached in the optimal case.

Spanwise distributions of  $\Delta C_{loss}$ , Eq. 4.7, have been calculated both with the CFD and the experimental data, and are plotted in Fig. 5.14 (c). The  $\Delta C_{loss}$  of the CFD has lower values than in the experiments for  $z/H < 1\%$ . This comparison suggests that also the profile losses added by the endwall fence have been over-estimated in the simulations. A region of local improvement has not been predicted between  $z/H > 2.5\%$  and  $z/H < 5\%$ , i.e. in the position of the passage vortex. For  $5\% < z/H < 9\%$  the  $\Delta C_{loss}$  of the experimental results reaches values 200% more negative than in the CFD, and remains below the simulation results up to  $z/H < 11.5\%$ . This negative region is due to the reduced spanwise penetration of the passage vortex, and corresponds to the peak region of the optimal configuration. Where the  $\Delta C_{loss}$  of the experiments is beneath the CFD results, the local worsening due to the fence is under-estimated. Also, the peak in  $\Delta C_{loss}$  at  $z/H = 10.5\%$  is higher for the CFD, meaning that the improvement at this spanwise location has been over-estimated. For  $z/H > 11.5\%$ , the simulations under-estimated the improvements, as larger diffusion of low momentum flow has been modeled in the wake region. In spite of the presence of local differences in Fig. 5.14 (c), both curves have similar trends.

Integrating the two curves of Fig. 5.14 (c) along the  $z$  direction, both integrals result positive, meaning that there is a net loss reduction both in CFD and experiments. Even if this analysis is limited to the region closer to the endwall ( $z/H < 20\%$ ), beyond  $z/H > 20\%$  there is no influence of secondary flows, so there is an actual overall loss reduction. Comparing these two integrals, turns out that the CFD over-estimated the improvement of the 24.4% w.r.t. the experiments. As discussed in Ch. 4 and shown in Fig. 4.15, the  $C_{loss}$  improvement at this stage is overall negligible, and according to the CFD the  $\Delta C_{loss}$  grows downstream. However, if in Plane 2 the experiments confirm a loss reduction, and the reduction in secondary flow strength has been proved by the  $C_{loss}$  trends, mixing losses generated in the optimal configuration must be less than in the baseline. This results in a more relevant improvement further downstream of the cascade. The improvement at an axial distance of 5.92%  $s$  from the cascade (Plane 7 in the CFD domain) is expected to be smaller than the predicted 1.96%. In fact, it is proved that the CFD model over-estimated the  $\Delta C_{loss}$ . The low Reynolds number of the flow is hypothesized as the cause of the difference between CFD and experimental results, given that the constants in the SST turbulence model are suitable for high Reynolds number flows. However, the validation of the methodology can be considered successful, as an actual improvement has been obtained.



(a)



(b)

**Figure 5.11:** Comparison of planar  $C_{loss}$  distributions for the baseline configuration of: (a) experimental data after interpolation, (b) CFD results.

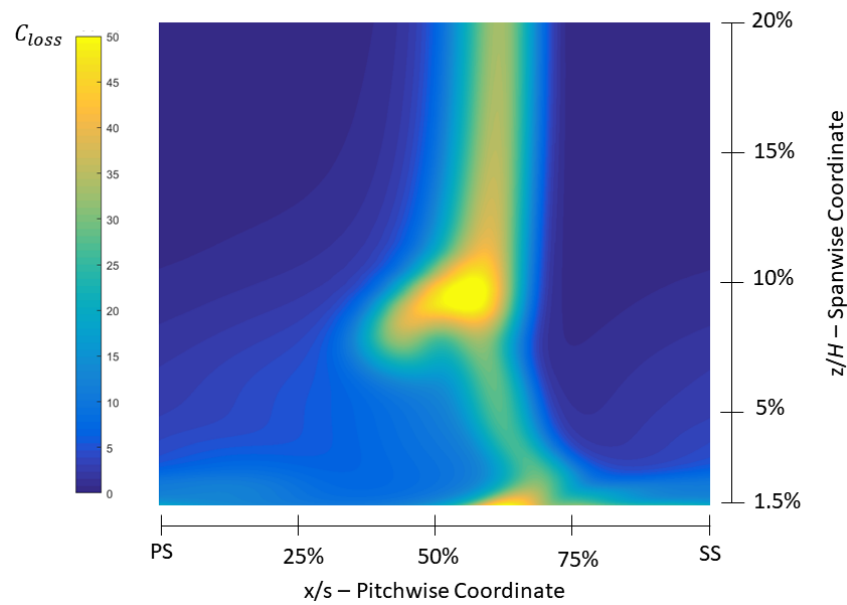
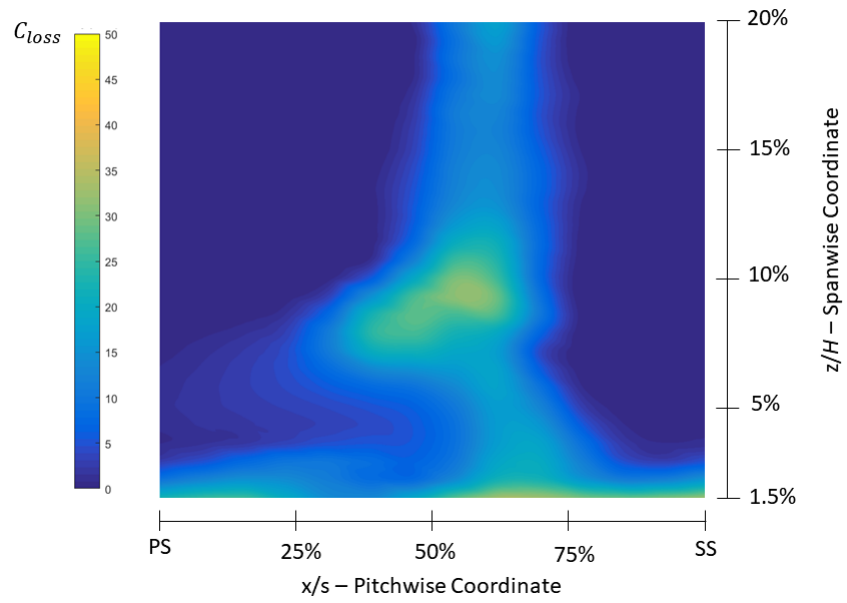


**Figure 5.12:** Comparison of planar  $C_{loss}$  distributions for the optimal configuration of: (a) experimental data after interpolation, (b) CFD results.

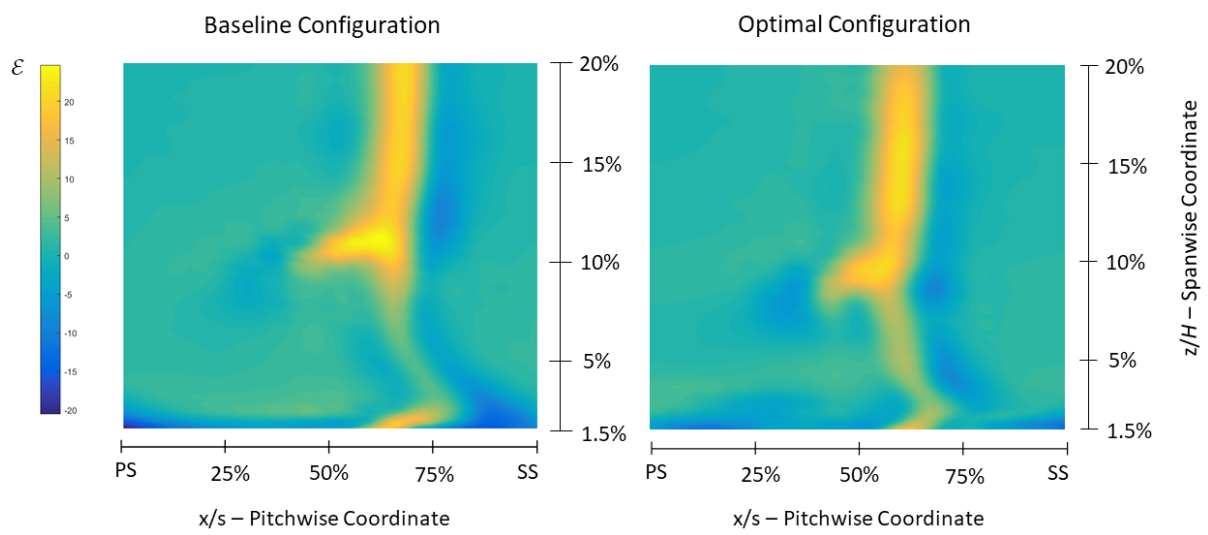
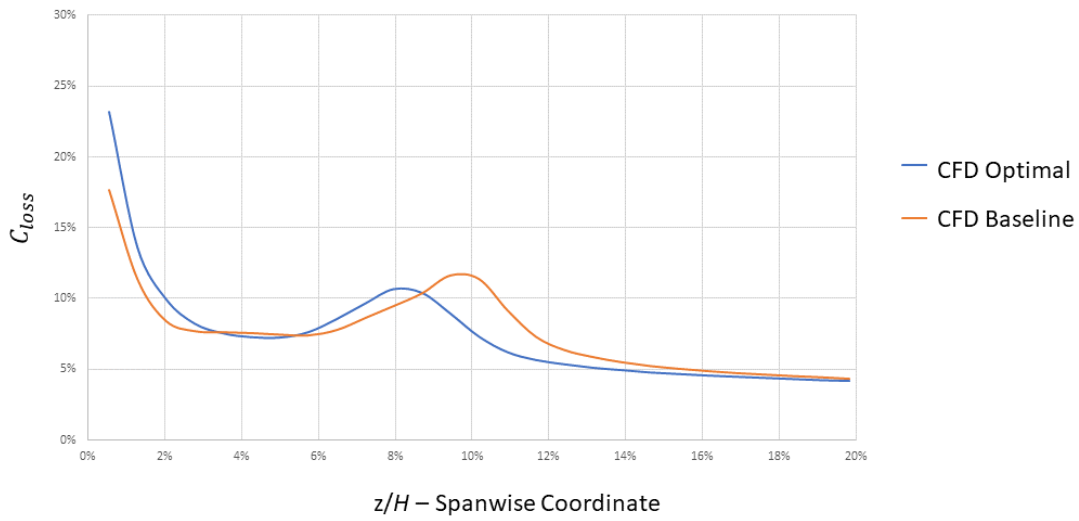
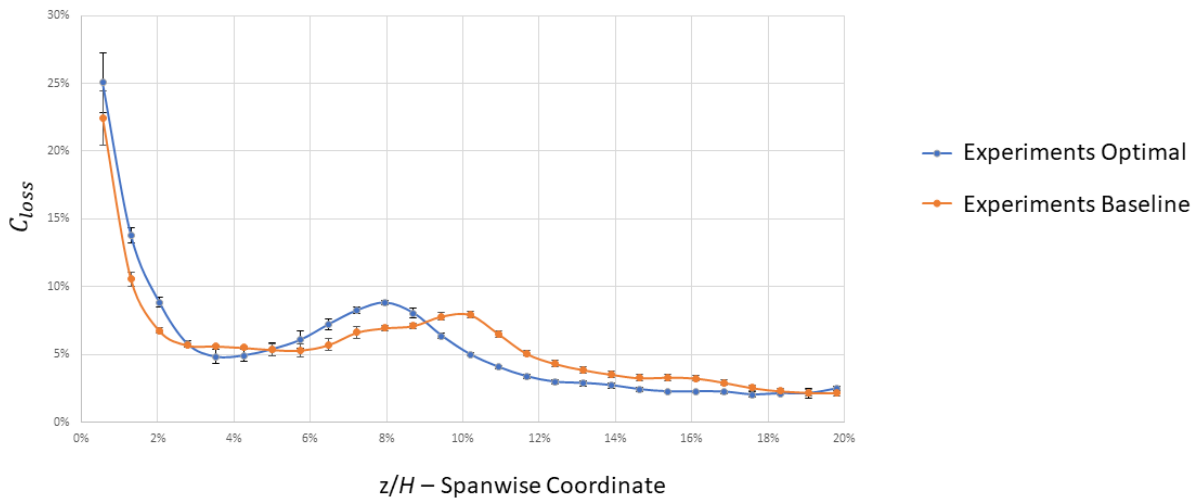


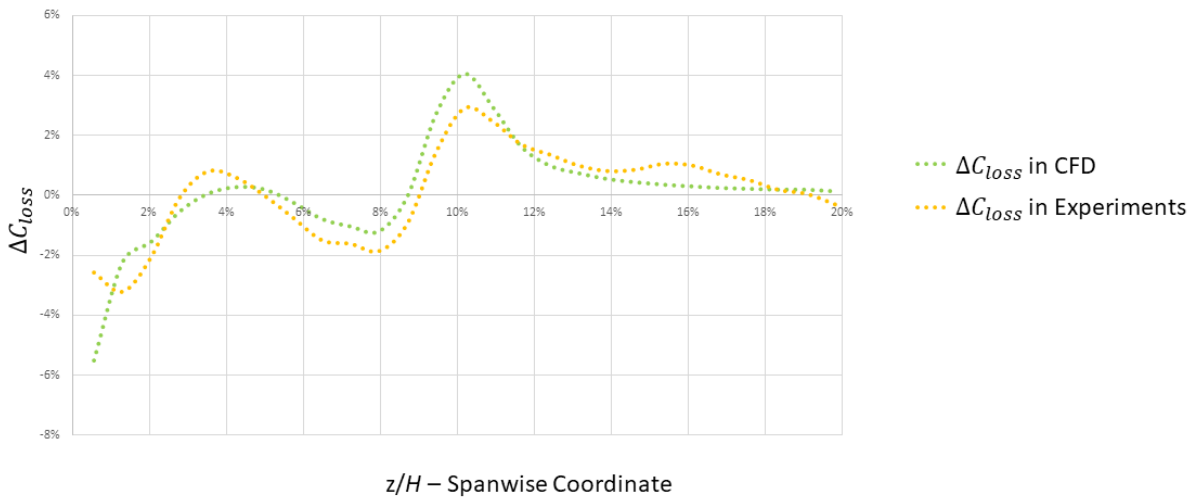
**Figure 5.13:** Planar distribution of the loss validation error  $\epsilon$  for the optimal configuration.



(a)



(b)



(c)

**Figure 5.14:** Comparisons of spanwise distributions at the measurement plane of: (a)  $C_{loss}$  of baseline and optimal configurations extracted from the CFD, (b)  $C_{loss}$  of baseline and optimal configurations obtained through experiments, (c)  $\Delta C_{loss}$  between the two configurations in according to CFD and experiments.

# 6

## CONCLUSIONS AND RECOMMENDATIONS

The present chapter rounds up the accomplishments of the thesis and outlines the key outcomes in Sec. 6.1. Sec. 6.2 concludes providing recommendations for future works.

### 6.1. CONCLUSIONS

The objective of this work is the development and testing of an automatic design tool for the reduction of secondary losses in stator turbine cascades. For this purpose, a response surface optimization framework based on CFD simulations has been created in Ansys Workbench for the design of endwall fences. The optimization framework has been tested with a low Reynolds steam turbine cascade and the results have been validated through wind tunnel experiments. The key outcomes of the work can be summarized:

- **What is the performance gain attainable with an optimal fence shape in terms of reduction in total pressure losses?**

Numerical calculations show a reduction of 1.96% of total pressure losses obtained with the optimal endwall fence. The loss reduction takes place downstream of the cascade, where mixing losses have been decreased thanks to the reduced secondary flow strength. The 48% reduction in secondary kinetic energy is achieved as the fence leading edge intercepts the passage vortex, splitting the vorticity and mitigating the crossflow.

- **What is a suitable optimization methodology for fence design?**

The CFD-based shape optimization successfully returned a fence configuration that led to a validated improvement in the steam turbine cascade used as a test case. The whole design process required around 400 hours CPU time of calculation, while the experimental campaign usually carried out for the design of an endwall fence can take weeks. The surrogate model shape optimization proved to be an efficient and effective design procedure.

- **What is the accuracy of CFD models in predicting secondary flow-induced losses?**

Calculations over-estimated the performance improvement by 24%. The loss reduction has been experimentally verified, and the measured loss distributions across the span are consistent with that from calculations, corroborating the results of the comparison.

### 6.2. RECOMMENDATIONS FOR FUTURE WORKS

Though an automatic design tool has been developed and demonstrated to be effective, there is still room for improvement in creating an all-around means for design optimization. For what regards the optimization tool, a full parameterization should be implemented for the turbine blade geometries, both for adapting the tool to whichever cascade geometry and for attempting an optimization of blades and fence together. Then, the optimization procedure could be improved by adding non-linear constraints. A structural analysis should

be incorporated into the tool to ensure that the fence can withstand the aerodynamic loading without deformation. Also, given that the second major effect of the secondary flow is the detriment of the blade cooling, a heat transfer analysis could ensure that the creation of hot spots on the blade surfaces is avoided.

A much larger energy loss reduction is expected in a cascade featuring a stronger secondary flow. As discussed also in Sec. 2.2.5, the secondary flow entity is affected by a series of cascade characteristics, in particular blade loading, Reynolds number, and blade aspect ratio; blade rows with large blade loading, large Reynolds number, and low aspect ratio suffer from large secondary losses. The test case considered in this work, is a low loading, low Reynolds number and high aspect ratio cascade in which the secondary losses represented a minor loss generation factor. As a consequence, a 48% reduction in SKE entailed only a 1.96% reduction in total pressure losses. Higher Reynolds number flows would also allow a more accurate prediction of the loss generation with the CFD, as the constants used in the turbulence models are derived for high Reynolds number flows.

# BIBLIOGRAPHY

- [1] Denton, J., 1993. Loss Mechanisms in Turbomachinery. *The 1993 IGTI Scholar Lecture*.
- [2] T. Tamagawa, K. Fujii, M. Ohto and Y. Kawata, November 2011. Optimization of Secondary Flow Loss Reduction of High Loaded Gas Turbine Cascade. International Gas Turbine Congress 2011, Osaka, Japan.
- [3] Coull, J.D., 2016. Endwall Loss in Turbine Cascade. ASME. Turbo Expo: Power for Land, Sea, and Air, *Volume 2B: Turbomachinery* ():V02BT38A039.
- [4] Clark, C., Pullan, G., Curtis, E., Goenaga F., 2016. Secondary Flow Control in Low Aspect Ratio Vanes Using Splitters. ASME. Turbo Expo: Power for Land, Sea, and Air, *Volume 2B: Turbomachinery*, ():V02BT38A023.
- [5] IPCC, 2014, *Climate Change 2014: Mitigation of Climate Change. Contribution of Working Group III to the Fifth Assessment Report of the Intergovernmental Panel on Climate Change* [O. Edenhofer, R. Pichs-Madruga, Y. Sokona, E. Farahani, S. Kadner, K. Seyboth, A. Adler, I. Baum, S. Brunner, P. Eickemeier, B. Kriemann, J. Savolainen, S. Schlömer, C. von Stechow, T. Zwickel and J.C. Minx]. Cambridge, United Kingdom and New York, NY, USA: Cambridge University Press.
- [6] Sharma, O.P., Butler, T.L., 1987. Predictions of Endwall Losses and Secondary Flows in Axial Flow Turbine Cascades. *J. Turbomach*, 109(2), pp.229-236.
- [7] Greitzer, E.M., Tan, C.S., Graf, M.B., 2004. *Internal Flow Concepts and Applications*. New York, USA: Cambridge University Press.
- [8] Squire, H.B., Winter, K.G., 1951. The Secondary Flow in Cascade of Aerofoils in Non-Uniform Stream. *Royal Aircraft Establishment*, Report No: AERO 2317.
- [9] Lakshminarayana, B., Horlock, J.H., 1973. Generalized expression for Secondary Vorticity Using Intrinsic Co-ordinates. *J. Fluid Mech.*, 59(1), pp. 97-115.
- [10] Dixon, S.L., Hall, C.A., 2014. *Fluid Mechanics and Thermodynamics of Turbomachinery*. 7th ed. Oxford, UK: Elsevier Inc.
- [11] Hawthorne, W.R., 1955. Rotational Flow Through Cascades. *J. Mech. & Appl. Math.*, 8(3), pp. 266–292.
- [12] Herzig, H. Z., Hansen, A. G., and Costello, G. R., 1954. Visualization Study of Secondary Flow Through Cascades. *NACA TN 1163*.
- [13] Armstrong, Ncd., 1955. The Secondary Flow in a Cascade of Turbine Blades. *ARC R&M 2979*.
- [14] Klein, A., 1966. Untersuchungen über den Einfluss der Zuström-grenzschicht auf die Sekundärströmung in den Beschaukelungen von Axialturbinen. *Forsch. Ing.*, Bd 32, Vol. 6. (English translation: Investigation of the Entry Boundary Layer on the Secondary Flows in the Blading of Axial Turbines. BHRAT 1004).
- [15] Eckerle, W.A., Langston, L.S., 1986. Horseshoe Vortex Formation Around a Cylinder. ASME. Turbo Expo: Power for Land, Sea, and Air, *Volume 1: Turbomachinery* ():V001T01A109. doi:10.1115/86-GT-246.
- [16] Osnaghi, C., 2012. *Teoria delle Turbomacchine*. 2nd ed. Milano, IT: Esculapio.
- [17] Bölcs, A., 1969. Flow Investigations in a Water Channel at Subsonic and Supersonic Veocities. *Escher Wyss News*, 42(1).
- [18] Langston, L.S., Nice, M.L., and Hooper, R.M., 1977. Three-Dimensional Flow Within a Turbine Blade Passage. *ASME J. Eng. Power*, 99(1), pp. 21-28.
- [19] Takeishi, K., Matsuura, M., Aoki, S., Sato, T., 1989. An Experimental Study of Heat Transfer and Film Cooling on Low Aspect Ratio Turbine Nozzles. *ASME. Turbo Expo: Power for Land, Sea, and Air, Volume 4: Heat Transfer; Electric Power; Industrial and Cogeneration* ():V004T08A021. doi:10.1115/89-GT-187.

- [20] Sieverding, C.H., Van den Bosch, P., 1983. The Use of Coloured Smoke to Visualize Secondary Flows in a Turbine-Blade Cascade. *J. Fluid Mech.*, 134, pp. 85-89.
- [21] Sieverding, C.H., 1985. Recent Progress in the Understanding of Basic Aspects of Secondary Flows in Turbine Blade Passages. *J. Eng. Gas Turbines Power*, 107(2), pp.248-257.
- [22] Langstom, L.S., 2001. Secondary Flows in Axial Turbines - A Review. *Annals New York Academy of Sciences*, 934, pp. 11-26.
- [23] Goldstein, R.J., Spores, R.A., 1988. Turbulent Transport on the Endwall in the Region Between Adjacent Turbine Blades. *ASME Jour. of Heat Transfer*, 110, pp. 862-869.
- [24] Wang, H.P., Olson, S.J., Goldstein, R.J. and Eckert, E.R.G., 1997. Flow Visualization in a Linear Turbine Cascade of High Performance Turbine Blades.
- [25] Belik, L., 1975. Secondary Losses in Turbine Blade Cascade With Low Aspect Ratio and Large Deflection. *Proc. 6th Conf. on Steam Turbines of Large-Power Output*, Plzen, Czechoslovakia.
- [26] Sjolander, S.A., *The Endwall Boundary Layer in an Annular Cascade of Turbine Nozzle Guide Vanes*, Carleton U., Canada TR ME/A 75-4.
- [27] Marchal, P., Sieverding, C. H., 1977. Secondary Flows Within Turbomachinery Bladings. *Secondary Flows in Turbomachines*, AGARD 214.
- [28] Moore, J., 1983. Flow Trajectories, Mixing and Entropy Fluxes in a Turbine Cascade. *Viscous Effects in Turbomachines*, AGARD CP 351.
- [29] Gotthardt, H., 1983. *Theoretische und experimentelle Untersuchungen an ebenen Turbinengittern mit Pfeilung und V-Stellung*, dissertation, TU Braunschweig, Germany.
- [30] Wolf, H., 1961. Die Randverluste in geraden Schaufelgitter. *Wiss. Z. Tech.*, Hochschule Dresden, 10(2).
- [31] Gregory-Smith, D.G., Graves, C.P., 1983. Secondary Flows and Losses in a Turbine Cascade. *Viscous Effects in Turbomachines*, AGARD CP 351.
- [32] Perdicchizzi, A., Savini, M., Dossena V., 1996. Secondary Flow Investigations in Turbine Cascades. *Turbomachinery Fluid Dynamics and Heat Transfer*, New York, USA: CRC Press, pp. 125-156.
- [33] Yamamoto A., Nouse H., 1988. Effects of Incidence on Three-Dimensional Flows in a Linear Turbine Cascade. *ASME J. Turbomach.*, 110, pp. 486-496.
- [34] Perdicchizzi, A., 1990. Mach Number Effects on Secondary Flow Development Downstream of a Turbine Cascade, *J. Turbomach*, 112(4), pp. 643-651.
- [35] Perdicchizzi, A., Dossena, V., 1993. Incidence Angle and Pitch-Chord Effects on Secondary Flows Downstream of a Turbine Cascade. *J. Turbomach.*, 115(3), pp. 383-391.
- [36] Hodson, H.P., Dominy, R.G., 1987. The off-design performance of a low-pressure turbine cascade. *ASME J. Turbomach.*, 109, pp. 201-209.
- [37] Perdicchizzi, A., Ubaldi, M., Zunino, P., 1992. Reynolds Stress Distribution Downstream of a Turbine Cascade. *Journal of Experimental Thermal and Fluid Science*, 5, pp. 338-350.
- [38] Spataro, R., Santner, C., Lengani, D., and Gottlich, E., 2012. On the Flow Evolution Through a LP Turbine With Wide-Chord Vanes in an S-Shaped Channel. *ASME TurboExpo*, GT2012-681.
- [39] D'Ippolito, G., Dossena, V., Mora, A., 2011. The Influence of Blade Lean on Straight and Annular Turbine Cascade Flow Field. *J. Turbomach.*, 133(1), 011013.
- [40] Harrison, S., 1992. The Influence of Blade Lean on Turbine Losses. *J. Turbomach.*, 114, pp. 184-190.
- [41] Tan, C., Zhang, H., Chen, H., Yamamoto, A., 2010. Blade Bowing Effect on Aerodynamic Performance of a Highly Loaded Turbine Cascade. *J. Prop. and Power*, 26(3), pp. 604-608.

- [42] Deich, M.E., Zaryanskin, A.E., Fillipov, G.A., and Zatsepin, M., 1960. Method of Increasing the Efficiency of Turbine Stages with Short Blades. *Teploenergetika*, 2, pp. 240-254.
- [43] Kopper, F.C., Milano, R., 1981. Experimental Investigation of Endwall Profiling in a Turbine Vane Cascade. *AIAA Journal*, 19, pp. 1033-1040.
- [44] Dossena, V., Perdichizzi, A., Savini, M., 1998. The Influence of Endwall Contouring on the Performance of a Turbine Nozzle Guide Vane. *ASME J. Turbomach.*, 121, pp. 200-208.
- [45] Zess, G.A., Thole, K.A., 2001. Computational Design and Experimental Evaluation of Using a Leading Edge Fillet on a Gas Turbine Vane. ASME Paper 2001-GT-0404, June 2001.
- [46] Sauer, H.H., Müller, R.R., Vogeler, K.K., 2000. Reduction of Secondary Flow Losses in Turbine Cascades by Leading Edge Modifications at the Endwall. *ASME. J. Turbomach.*, 123(2): pp. 207-213. doi:10.1115/1.1354142.
- [47] Müller, R.R., Sauer, H.H., Vogeler, K.K., Hoeger, M.M., 2002. Influencing the Secondary Losses in Compressor Cascades by a Leading Edge Bulb Modification at the Endwall. *ASME. Turbo Expo: Power for Land, Sea, and Air, Volume 5: Turbo Expo 2002, Parts A and B* (): pp. 783-791. doi:10.1115/GT2002-30442.
- [48] Luo, J., Feng, L., McBean, I., 2015. Turbine Blade Row Optimization Through Endwall Contouring by an Adjoint Method, *Journal of Propulsion and Power*, 31(2), pp. 505-518. <https://doi.org/10.2514/1.B35152>.
- [49] Shahpar, S., Caloni, S., de Prieëlle, 2017. Automatic Design Optimization of Profiled Endwalls Including Real Geometrical Effects to Minimize Turbine Secondary Flows. *ASME J. Turbomach.*, 139, 071010.
- [50] Denton, J., 2010.
- [51] Prümper, H., 1975. Verbesserung des Wirkungsgrades axialer Turbinenstufen durch Reduzierung der Sekundärverluste. Dissertation, RWTH Aachen, F. R. Germany, pp.30.
- [52] Prümper, H., 1972. Application of Boundary Layer Fences in Turbomachinery. *AGARD ograph No. 164 on Boundary Layer Effects in Tubomachinery*, pp.311-332.
- [53] Kawai, T., Adachi, T., 1987. Effects of Blade Boundary Layer Fences on Secondary Flow and Losses in a Turbine Cascade. *Proc. 1987 Tokyo Int, Gas Turbine Congr.*, 2, pp. 115.
- [54] Kawai, T., Shinoki, S., Adachi, T., 1989. Secondary Flow Control and Loss Reduction in a Turbine Cascade Using Endwall Fences. *JSME international journal. Ser. 2, Fluids engineering, heat transfer, power, combustion, thermophysical properties*, 32(3), pp.375-387.
- [55] Kawai, T., Adachi, T., Shinoki, S., 1990. Improvement in Turbine Blade Aerodynamic Force in the Tip Region. *JSME international journal. Ser. 2, Fluids engineering, heat transfer, power, combustion, thermophysical properties*, 33(3), pp.517-524.
- [56] Kawai, T., 1994. Effect of Combined Boundary Layer Fences on Turbine Secondary Flow and Losses. *JSME International Journal*, 37(2), pp. 377-384.
- [57] Chung, J. T., Simon, T. W., Buddhavarapu, J., 1991. Three-Dimensional Flow Near the Blade/Endwall Junction of a Gas Turbine: Application of a Boundary Layer Fence. ASME. Turbo Expo: Power for Land, Sea, and Air, *Volume 4: Heat Transfer; Electric Power; Industrial and Cogeneration* ():V004T09A008.
- [58] Chung, J. T., Simon, T. W., 1993. Effectiveness of the Gas Turbine Endwall Fences in Secondary Flow Control at Elevated Freestream turbulence Levels. ASME. Turbo Expo: Power for Land, Sea, and Air, *Volume 1: Aircraft Engine; Marine; Turbomachinery; Microturbines and Small Turbomachinery*, ():V001T03A019.
- [59] Aunapu, N. V., Volino, R. J., Flack, K. A., Stoddard, R. M., Secondary Flow Measurements in a Turbine Passage With Endwall Flow Modification. *J. Turbomach*, 122(4), pp.651-658.
- [60] Moon, Y.J., Koh, S.R., 2001. Counter-rotating streamwise Vortex Formation in the Turbine Cascade with Endwall Fence. *Computer and Fluids*, 30(4), pp.473-490.

- [61] Camci, C., Rizzo, D. H., 2002. Secondary Flow and Forced Convection Heat Transfer near Endwall Boundary Layer Fences in a 90° Turning Duct. *International Journal of Heat and Mass Transfer* 45(4), pp.831-843.
- [62] Kumar, K.N., Govardhan, M., 2011. Secondary Flow Loss Reduction in a Turbine Cascade with a Linearly Varied Height streamwise Endwall Fence. *International Journal of Rotating Machinery*, 2011, 352819.
- [63] Kumar, K.N., Govardhan, M., 2014. On Topology of Flow in a Turbine Cascade, *ASME Journal of Fluid Engineering*, 136, 081201.
- [64] Hartland, J.C., Gregory-Smith, P.G., Harvey, N.W. and Rose, M.G., 2000. Nonaxisymmetric Turbine End Wall Design: Part II - Experimental Validation. *ASME J. Turbomach.*, 122, pp. 286-293.
- [65] Cumpsty, N.A., Horlock, J.H., 2006. Averaging Nonuniform Flow for a Purpose. *J. Turbomach*, 128(1), pp.120-129.
- [66] Myers, R.H., Montgomery, D.C., Anderson-Cook, C. M., 2016. *RESPONSE SURFACE METHODOLOGY: Process and Product Optimization Using Designed Experiments*, 4th ed., Hoboken, New Jersey: Wiley.
- [67] *Ansys Helper*, Ansys Inc., Release 17.1
- [68] Delvecchio, R.J., 1997. *Understanding Design of Experiments: A Primer for Technologists*. Cincinnati, CA, USA: Hanser Publications.
- [69] Beyer, W., Liebscher, M., Beer, M., Graf, W., 2006. Neural Network Based Response Surface Methods - a Comparative Study. LS-DYNA Anwenderforum, Ulm, pp. K-II-29 to K-II-38.
- [70] Diwekar, U.M., Kalagnanam, J.R., 1997. Efficient sampling technique for optimization under uncertainty. *AIChE Journal.*, 43(2), pp. 44-47.
- [71] Schittkowski, K., 2009. NLPQLP: A Fortran Implementation of a Sequential Quadratic Programming Algorithm with Distributed and Non-Monotone Line Search. Report, Department of Computer Science, University of Bayreuth.
- [72] Menter, F.R., 1994, Two-Equation Eddy-Viscosity Turbulence Models for Engineering Applications. *AIAA Journal*, 32 (8): 1598–1605.
- [73] Persico, G., Gaetani, P., Dossena, V., D'Ippolito, G., Osnaghi, C., 2009. On the definition of the secondary flow in three-dimensional cascades. *Proceedings of the Institution of Mechanical Engineers, Part A: Journal of Power and Energy*, Vol. 223(6), pp. 667-676.
- [74] Prasad, A., 2005. Calculation of the Mixed-Out State in Turbomachine Flows. *J. Turbomach*, 127(3), pp.564-572.
- [75] Wilcox, D., C., 2006. *Turbulence Modeling for CFD*, 3rd ed. La Cañada, California, USA: DCW Industries.
- [76] Y. Li, Y. Xue and L. Cao, 2012. Numerical Study of the Secondary Flow in Steam Turbine Static Cascade under Varying Conditions. Asia-Pacific Power and Energy Engineering Conference, Shanghai, pp. 1-4. doi: 10.1109/APPEEC.2012.6307016